RICE UNIVERSITY

An Assessment of Gadonanotubes as Magnetic Nanolabels for Improved Stem Cell Detection and Retention in Cardiomyoplasty

by

Lesa A. Tran

A THESIS SUBMITTED
IN PARTIAL FULFILLMENT OF THE
REQUIREMENTS FOR THE DEGREE

Doctor of Philosophy

APPROVED, THESIS COMMITTEE

Lon J. Wilson, Chair
Professor of Chemistry

Seiichi P. T. Matsuda
E. Dell Butcher Professor of Chemistry and
Professor of Biochemistry & Cell Biology,
Department Chair

Jeffrey G. Jacot
Assistant Professor of Bioengineering

Emerson C. Perin
Medical Director, Stem Cell Center, Texas Heart Institute

Maria da Graça Cabreira
Research Scientist, Stem Cell Center, Texas Heart Institute

HOUSTON, TEXAS
December 2012

ABSTRACT

An Assessment of Gadonanotubes as Magnetic Nanolabels for Improved Stem Cell Detection and Retention in Cardiomyoplasty

by

Lesa A. Tran

In this work, gadolinium-based carbon nanocapsules are developed as a novel nanotechnology that addresses the shortcomings of current diagnostic and therapeutic methods of stem cell-based cardiomyoplasty. With cardiovascular disease (CVD) responsible for approximately 30% of deaths worldwide, the growing need for improved cardiomyoplasty has spurred efforts in nanomedicine to develop innovative techniques to enhance the therapeutic retention and diagnostic tracking of transplanted cells. Having previously been demonstrated as a high-performance T_1-weighted magnetic resonance imaging (MRI) contrast agent, Gadonanotubes (GNTs) are shown for the first time to intracellularly label pig bone marrow-derived mesenchymal stem cells (MSCs). Without the use of a transfection agent, micromolar concentrations of GNTs deliver up to 10^9 Gd^{3+} ions per cell, allowing for MSCs to be visualized in a 1.5 T clinical MRI scanner. The cellular response to the intracellular incorporation of GNTs is also assessed, revealing that GNTs do not compromise the viability, differentiation potential, or phenotype characteristics of the MSCs. However, it is also found that GNT-labeled MSCs exhibit a decreased response to select cell adhesion proteins and experience a non-apoptotic, non-proliferative cell cycle arrest, from which the cells recover 48 h after GNT internalization. In tandem with developing GNTs as a new stem cell diagnostic agent, this

current work also explores for the first time the therapeutic application of the magnetically-active GNTs as a magnetic facilitator to increase the retention of transplanted stem cells during cardiomyoplasty. *In vitro* flow chamber assays, *ex vivo* perfusion experiments, and *in vivo* porcine injection procedures all demonstrate the increased magnetic-assisted retention of GNT-labeled MSCs in the presence of an external magnetic field. These studies prove that GNTs are a powerful 'theranostic' agent that provides a novel platform to simultaneously monitor and improve the therapeutic nature of stem cells for the treatment of CVD. It is expected that this new nanotechnology will further catalyze the development of cellular cardiomyoplasty and other stem cell-based therapies for the prevention, detection, and treatment of human diseases.

Acknowledgments

First, I would like to thank my research advisor, Prof. Lon J. Wilson, for his guidance and encouragement during my time at Rice University. From the first day I stepped into the lab eight years ago, his helpful advice and confidence in my abilities have continually stimulated me to better myself in both the laboratory and classroom settings. I really could not have chosen a better mentor and program, even if someone at Northwestern had blatantly told me otherwise.

I would also like to express my deep appreciation to Dr. Emerson C. Perin and Dr. Maria da Graça Cabreira for serving as my stand-in advisors at the Texas Heart Institute. You have made my time there a wonderful learning experience, as I now walk away with more biological knowledge and surgical skills than I could have ever imagined learning as a chemistry student. Graça, you have become my research "Mom" – thank you for always being so optimistic and loving during times of stress and need. In addition to the individuals mentioned above, I want to thank Prof. Seiichi P. T. Matsuda and Prof. Jeffrey G. Jacot for taking the time out of their busy schedules to serve on my Ph.D. thesis committee and give constructive criticism on this work.

I will never forget the wonderful Wilsonites I have had the privilege of meeting over the years. Dr. Jeyarama Ananta, Matthew Cheney, Brandon Cisneros, and Dr. Michael Matson were like my brothers, always providing me with helpful advice and endless entertainment. It was a pleasure to have Ari Berlin as my undergraduate assistant and sidekick. I would also like to thank Scott Berger, Sue Friend, Ayrat Gizzatov, Adem Guven, Mayra Hernandez-Rivera, Justin Law, Dr. Yuri Mackeyev, Meghan Jebb, Sophia

Phounsavath, Tawana Robinson, and Richa Sethi for all their help and company during my time in the Wilson group. Among former group members, I would like to specifically acknowledge Dr. Balaji Sitharaman, who first taught me the basics of good science.

My second research family at the Texas Heart Institute and St. Luke's Episcopal Hospital was an amazing group of individuals to work with and know. I am particularly grateful for Fred Baimbridge, Dr. Christina Bove, Dr. Maximillian Buja, Dr. Amy Caivano, Andre Critsinelis, Tracye Dauphin, Dr. Amir Gahremanpour, Ramkumar Krishnamurthy, Dr. Raja Muthupillai, Dr. Ralph Nichols, Dr. Micheline Resende, Allan Prejusa, Dr. Luiz Sampaio, Deirdre Smith, Dr. Deborah Vela, Dr. Xiaohong Wang, Dr. James Willerson, Dr. Yi Zheng, and the Cardiovascular Research Laboratories. I would also like to thank the Baylor College of Medicine Genomic and RNA Profiling Core.

Outside of the lab, all my family and friends made sure I was sane and happy for the past five years. I will never be able to fully express my love and gratitude to my husband Eric, our dog Min-Mei, my brothers Larry and Lester, my sisters Judith and Rany, my wonderful nieces and nephew, and my best friend Meeta. Most importantly, I wish to thank my parents, Yen M. and Le Tran, for their continual love and support. Thank you for teaching me how to be a good, hardworking person and letting me be as ambitious as I wanted. To them I dedicate this thesis.

This work was supported by an NIH Challenge Grant (1RC1EB010791-01), an NSF Graduate Research Fellowship (DGE-0940902), the Robert A. Welch Foundation (C-0627), and the Nanoscale Science and Engineering Initiative of the NSF at Rice University (EEC-0647452).

Table of Contents

List of Figures

List of Tables

Nomenclature

1×PBS	Phosphate Buffered Saline
3D	Three-dimensional
αMEM	Alpha-modified Minimal Essential Medium
AMI	Acute Myocardial Infarction
BSA	Bovine Serum Albumin
CA	Contrast Agent
CDC	Cardiosphere-derived Cell
CHF	Chronic Heart Failure
CNT	Carbon Nanotube
Ct	Cycle Threshold
CVD	Cardiovascular Disease
DMEM	Dulbecco's Modified Eagle Medium
FBS	Fetal Bovine Serum
FDA	Food and Drug Administration
FITC	Fluorescein Isothiocyanate
GBCA	Gadolinium-based Contrast Agent
Gd-DTPA	Magnevist®; Gadopentetic Acid
GF	Gadofullerene
GNT	Gadonanotube
ICP-OES	Inductively-Coupled Plasma Optical Emission Spectrometry
ICP-MS	Inductively-Coupled Plasma Mass Spectrometry

LV	Left Ventricle
MR	Magnetic Resonance
MRI	Magnetic Resonance Imaging
MSC	Mesenchymal Stem Cell
MWNT	Multi-walled Carbon Nanotube
PI	Propidium Iodide
PLL	Poly-L-Lysine
RT	Room Temperature
RT-PCR	Real-time Polymerase Chain Reaction
RV	Right Ventricle
SPIO	Superparamagnetic Iron Oxide
SPM	Superparamagnetic Microsphere
SWNT	Single-walled Carbon Nanotube
TE	Echo Time
TEM	Transmission Electron Microscopy
TR	Repetition Time
USPIO	Ultrasmall Superparamagnetic Iron Oxide

Chapter 1

Introduction

Although stem cell therapy has proven to be an effective approach to treat cardiovascular disease (CVD), the challenges of improving the therapeutic retention and diagnostic visualization of transplanted stem cells remain unsolved. This work, for the first time, presents the superparamagnetic gadolinium-based carbon nanocapsules known as Gadonanotubes (GNTs) as a nanotechnological platform with simultaneous therapeutic and diagnostic, or theranostic, capabilities that help solve the limitations of current cardiovascular stem cell therapeutic methods.

With CVD as the leading cause of death worldwide, interest in cell transplantation therapy, or cardiomyoplasty, to treat damaged cardiac tissue has grown exponentially over the past decade. Of the various cell types used for cardiomyoplasty, adult bone marrow-derived mesenchymal stem cells (MSCs) are particularly attractive for clinical use because of their allogeneic nature, therapeutic potential, and ease of isolation and expansion. As such, numerous preclinical and clinical studies in recent years have

suggested the effective performance of transplanted MSCs in repairing damaged cardiovascular tissue. Irrespective of the cell type used, however, the low rates of cell homing, retention, and survival in the heart are fundamental challenges that must be overcome to enhance the therapeutic outcome of current cell transplantation approaches. Another inherent shortcoming of cardiomyoplasty is the difficulty in noninvasively tracking the movement of transplanted cells to elucidate their biodistribution and eventual incorporation into cardiac tissue. For these reasons, recent research efforts in nanotechnology and nanomedicine have focused on the development of innovative tools and methods to improve the therapeutic efficiency and diagnostic imaging of transplanted cells.[1–3] Having previously been demonstrated as a high-performance T_1-weighted magnetic resonance imaging (MRI) contrast agent with efficacies over 40 times higher than currently available clinical agents, the magnetically-active GNTs have the potential to address the limitations of stem cell therapy, as documented and discussed in this thesis. To fully illustrate the background and significance of this work, Chapter 2 reviews the biology of MSCs, the current status of stem cell therapy, and the recent developments of GNTs as a clinical MRI agent.

In this thesis, the primary objective is to evaluate the efficiency of GNTs as an intracellular MRI nanolabel. Chapter 3 details the *in vitro* optimization of GNT cell labeling, electron microscopy imaging of the intracellular GNT retention, and MRI visualization of GNT-labeled MSCs using a clinical 1.5 T MRI scanner. After the successful demonstration of T_1-weighted MR imaging of GNT-labeled MSCs, the short- and long-term cellular response to the intracellular incorporation of GNTs is assessed before advancing to *in vivo* experiments. In Chapter 4, the assays and transcriptome

analysis evaluating the effects of GNT incorporation on MSC viability, differentiation potential, adhesion behavior, phenotype characteristics, and growth kinetics are presented. Sections of Chapters 3 and 4 have been drawn from previously published work by L.A. Tran et al.[4] Along with developing GNTs as an intracellular MRI agent, the magnetically-active GNTs are presently being evaluated as a magnetic facilitator to improve the retention of GNT-labeled MSCs in cardiac tissue during cardiomyoplasty. Chapter 5 describes for the first time the *in vitro*, *ex vivo*, and *in vivo* experiments demonstrating the magnetically-driven therapeutic application and retention efficiency of GNT-labeled MSCs. Finally, Chapter 6 summarizes the conclusions of the described studies and elaborates on the future work envisioned beyond this present work to further confirm the potential of GNTs as a new, powerful stem cell theranostic agent for the treatment of CVD.

Chapter 2

Background and Literature Review

2.1. Mesenchymal Stem Cells

MSCs are nonhematopoietic multipotent progenitor cells found in all mammals that have the ability to differentiate into a variety of mesenchymal lineages, including adipocytes, chondrocytes, osteocytes, and cardiomyocytes. Although extremely rare in bone marrow (approximately 1:100,000), MSCs can readily be isolated and expanded *in vitro* by more than 1 million-fold while retaining their growth and multilineage potential.[5] Similar to fibroblastic cell lines, MSCs expand at a fast rate but maintain their contact inhibition upon reaching confluence in culture.

Phenotypically, MSCs express a number of cell surface markers, including CD29, CD90, CD105; however, none are specific to MSCs and the expression levels of these markers are heavily influenced by the tissue source, isolation methods, and *in vitro* conditions.[6] It is also established that MSCs do not express hematopoietic markers, such

as CD45, or the endothelial marker CD31.[7] MSCs also produce an array of growth factors and cytokines which can induce surrounding endogenous cells through a paracrine mechanism to differentiate while the MSCs undergo new tissue formation.

One striking characteristic that has been observed is that at appropriate levels, the presence of cultured MSCs does not stimulate immune responses within *in vivo* systems, due to their lack of major histocompatibility complexes and co-stimulatory molecules and their ability to secrete immunosuppressive cytokines.[8] Therefore, it may be possible to isolate MSCs from one donor, expand them *in vitro*, and administer them to an allogeneic host without the need for immunosuppression. Additionally, MSCs have the natural ability to home to sites of injury and inflammation, which suggest their active role in tissue repair.[9] This homing property is independent of the distance of the MSCs from the injury site, but diminishes with age and disease.

2.2. Stem Cell Cardiomyoplasty

Because of their ease of isolation and *in vitro* expansion, differentiation potential, paracrine effects, immunologic characteristics, and homing abilities, MSCs are ideal candidates for regenerative therapies to treat disorders of the bone, muscle, vasculature, organs, and skin.[10] In particular, recent studies have evaluated the use of MSCs for the treatment of cardiac injury after acute myocardial infarction (AMI) and chronic heart failure (CHF). A meta-analysis performed by Abdel-Latif et al. on 999 patient cases in 18 small clinical trials concluded that the use of adult bone marrow cells, such as MSCs, as therapeutic agents for cardiac repair post-AMI and CHF is safe and associated with

more anatomical and functional improvements than that of conventional therapies.[11] Similar cardiomyoplasty studies performed using MSCs in porcine models corroborated the benefits of stem cell transplantation, suggesting that implanted MSCs in damaged myocardium improved postinfarction hemodynamics and prevented wall thinning and stiffness.[12]

Despite the positive yet modest outcomes of MSC-based cardiomyoplasty, two major challenges still need to be addressed in the development of this therapy. One issue is the low and variable rates of cell retention and survival in the heart, which greatly limits the success of restoring cardiac tissue and function. Using immunohistochemistry and radiolabeling techniques, several studies based on human and animal models have reported that between 5-15% of the MSCs remain in the heart post-transplantation with the majority of the cells traveled to other organs in the body, regardless of the delivery method and dosage level used.[13–16] Several biochemical and physical approaches have been explored to improve the retention and survival of transplanted cells in the myocardium, including transgenic enhancement of protein secretion, *in vitro* conditioning for improved survival function, exploitation of endogenous mechanisms to enhance homing, biochemical targeting of tissue-specific cues,[17] and transplantation of cells integrated in biomaterials or as three-dimensional (3D) aggregates to enhance cell differentiation and function.[18,19] However, clinical translation of such methods may be difficult to scale up and only moderately improved rates have been observed.

Another major drawback in stem cell therapy is the difficulty to accurately and noninvasively track MSCs in real-time and determine the eventual biodistribution of the cells post-transplantation. While many imaging modalities and labeling agents have been

explored (MRI of magnetic particles, γ imaging of radiolabels, neutron activation of lanthanide-based compounds, and optical imaging of quantum dots and fluorescent reporter genes), these methods have moderate efficacies and the agents used must be in high concentrations to be detectable, which introduces the risk of becoming cytotoxic to the cells.[16,20,21] The visualization of individual cells and their tissues requires that each molecule of a particular agent induce a sufficient signal intensity to be detected at low concentrations, since biological constraints limit the amount of molecules that can be delivered into a single cell to the nanomolar (nM) range at a given time.[22]

To simultaneously resolve the issues of low retention rates and noninvasive cell tracking, the magnetic targeting and MRI of cells labeled with magnetic particles can be employed. However, no one to date has concurrently studied the magnetic-assisted retention and MRI visualization of magnetically-labeled cells for cardiomyoplasty. Cheng et al. have recently demonstrated that magnetic targeting enhances the engraftment and functional performance of superparamagnetic microsphere (SPM)-labeled cardiosphere-derived cells (CDCs) when intramyocardially transplanted into the infracted hearts of rats.[23,24] Using a superimposed magnet at the injection site, magnetic targeting enhanced the retention and eventual engraftment of iron-labeled CDCs in the recipient hearts by approximately 3-fold when compared to non-targeted cells over a 3-week period. However, these studies did not explore the MRI visualization of SPMs, which are larger versions (900 nm) of the FDA-approved superparamagnetic iron oxide (SPIO) nanoparticles (50-150 nm) used as T_2-weighted MRI contrast agents (CAs). Although proven moderately effective, T_2-weighted CAs generally darken acquired magnetic resonance (MR) images which may not be ideal for enhancing visual details (as opposed

to T_1-weighted CAs that brighten MR images). Nonetheless, SPIO nanoparticles have been shown to be internalized by MSCs, unlike the T_1-weighted Gd^{3+}-based MRI CA Magnevist®.[25] To optimize cellular uptake, most researchers employ the use of polycationic transfection agents such as protamine sulfate and poly-L-lysine (PLL). It has been demonstrated that the internalization of low dosages of SPIO nanoparticles does not affect cell viability or proliferation, but the use of a transfection agent may affect MSC differentiation.[26] Additionally, many polydisperse polycationic transfection agents are not FDA-approved for clinical use, as they are cytotoxic when used alone or at high (10 μg/mL) concentrations.[27,28]

2.3. Gadonanotubes

Carbon nanostructures are ideal platforms for medical therapeutic and diagnostic agent design.[29] The two main categories of these materials are carbon fullerenes (C_{60}, C_{70}, C_{80}, C_{2n}, etc.), which are spherical carbon molecules, and carbon nanotubes (CNTs), which are cylindrical rolls of graphene sheets. Because their surfaces can be chemically modified, carbon nanostructures may serve as molecular scaffolds for medically-relevant moieties such as drugs, peptides, antibodies, and other functional groups.[30] This surface functionalization may allow carbon nanostructures to become nontoxic, nonimmunogenic, and water-soluble.[31–33] In addition to being bioinert,[34] carbon nanostructures have also been shown to translocate across cellular membranes and accumulate within cells without significant cytotoxic effects.[4,35–37] Finally, the empty space within carbon nanostructures allows for the encapsulation of small molecules and

ions.[38–40] This loading ability is particularly useful in the design of MRI CAs, as these carbon nanomaterials can trap Gd^{3+} ions within the carbon cage and prevent the metal ions from dissociating under physiological conditions, thus producing gadonanostructures.[41]

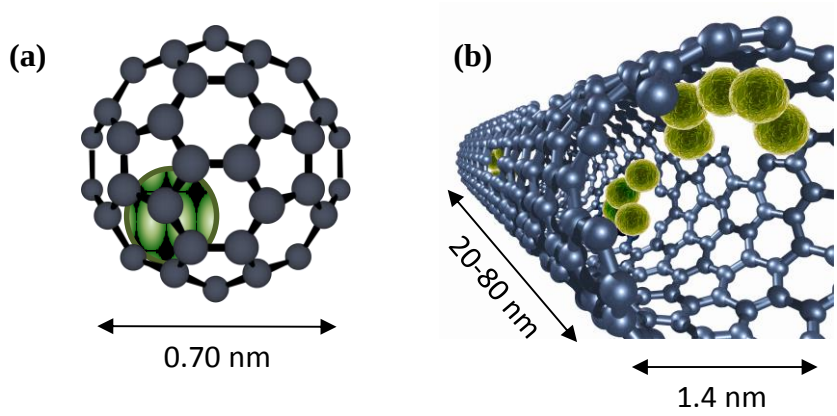

Figure 2.1 – Representative illustrations of two gadonanostructures: (a) a Gadofullerene and (b) a Gadonanotube.

Two gadonanostructures (Figure 2.1) that have recently been evaluated as T_1-weighted MRI CAs are the Gadofullerenes and GNTs. Gadofullerenes (GFs) are endohedral C_{60} fullerenes that encase a single Gd^{3+} ion inside the carbon framework, while GNTs are short (20-80 nm) segments of single-walled CNTs (SWNTs) that encapsulate small clusters of 5-10 Gd^{3+} ions.[29] Gadonanostructures have been reported to exhibit T_1 relaxivities of up to 40 times higher than those of MRI CAs in current clinical use. The GFs have r_1 values ranging from 20 to 100 mM^{-1} s^{-1} (37 °C, 1.5 T).[33] More impressively, the GNTs hold the highest recorded relaxivity to date at a clinically-relevant field, with a value of 170 mM^{-1} s^{-1} (37 °C, 1.5 T).[42]

Although both gadonanostructures exhibit higher T_1 relaxivities when compared to current MRI CAs, the GNTs are superior to the GFs from a synthetic standpoint. Because the production of GFs is both chemically challenging and time-consuming, obtaining large quantities of GFs is extremely difficult.[29] However, the synthesis of GNTs requires far less effort to produce gram quantities, which may be critical if the widespread clinical use of GNTs is ever to be realized. This ease of production is due to their ability to internally load Gd^{3+} ions through the many sidewall defects produced by the chemical cutting procedure used to produce GNTs.[42]

It has been demonstrated that GNTs can serve as effective cellular magnetic probes. Due to their short length, GNTs can readily internalize into mammalian cells without the assistance of a transfection agent. As suggested by Raffa et al., short CNTs (similar to GNTs) coated in surfactant can act as tiny 'nano-needles' that can insert and readily diffuse through cellular membranes.[43] As such, recent studies have shown that GNTs can internalize into a variety of cell types, performing as an effective T_1-weighted CA in breast cancer cells[37] and T_2-weighted CA in macrophages.[44] This phenomenon, in addition to their inherent magnetic properties, biocompatibility, and relaxivity performance, has prompted a more extensive investigation of GNTs as a new cellular labeling platform to improve MRI contrast at lower dosages.

Chapter 3

Gadonanotubes as MRI Nanolabels for Stem Cell Detection

3.1. Introduction

The demand for advanced cell tracking technologies is increasing in the field of stem cell therapy. While currently relying on the immunohistochemistry of extracted tissue samples to visualize cells within a living system, investigators desire a noninvasive and more accurate means of imaging transplanted stem cells *in vivo* to better examine their regenerative abilities, monitor their retention rate in the target tissue, and determine the biodistribution of cells post-transplantation.

Recent efforts have been made to develop nanoparticle-based stem cell labeling techniques using MRI.[20,35,45,46] Among the various medical diagnostic imaging modalities available, MRI is ideal for tracking stem cells *in vivo* as it allows for serial imaging acquisitions that provide high spatial resolution in a noninvasive and non-ionizing manner. In 2007, approximately 43% of the 27.5 million clinical MRI procedures

performed in the U.S. use CAs to alter MR signals.[47] In general, paramagnetic T_1-weighted CAs, which enhance MR signals to produce bright positive contrast, are preferred over superparamagnetic T_2-weighted CAs, which decrease MR signals to produce dark negative contrast. The hypointensity caused by T_2-weighted CAs may make it more difficult to distinguish them from the inherently low signals caused by other tissues or imaging artifacts.[48] Most available T_1-weighted CAs are based on the Gd^{3+} ion because of its high magnetic moment and symmetric electronic ground state.[49] However, these FDA-approved gadolinium-based CAs (GBCAs) are restricted to extracellular space and, in general, lack the ability to accumulate within cells to produce signal intensity enhancement for their detection on the cellular level.[50]

A primary focus in GBCA advancement is the development of new CAs that exhibit greater water-proton relaxation efficacy, or relaxivity, than that of current CAs to improve image contrast. Because biological constraints limit the number of CAs that can be delivered to the surface or interior of a single cell to the nanomolar (nM) range at a given time,[22] the visualization of individual cells and tissues requires that each unit of a particular CA produce a high enough signal intensity to be detected at nanomolar concentrations. In addition to its performance, an ideal CA must also be biologically inert and biocompatible at appropriate dosage levels for clinical use. To address these concerns, the high-performance GNTs were examined as an intracellular MRI agent that can effectively label cells at low loading concentrations. This chapter describes the *in vitro* cell labeling performance of GNTs in pig bone marrow-derived MSCs for T_1-weighted cellular MRI.

3.2. Materials & Methods

3.2.1. Synthesis of Gadonanotubes

GNTs were produced by following a previously established protocol.[42] Briefly, full-length SWNTs synthesized by the electric-arc discharge method were cut into ultra-short SWNTs (US-tubes, 20-80 nm in length) by fluorination followed by pyrolysis at 1000 °C under an inert Ar atmosphere.[51] After production, the US-tubes were sonicated with concentrated HCl for 60 min to remove metal catalyst impurities. The US-tubes were then reduced using Na^0/THF to produce predominantly individualized, or debundled, US-tubes.[52] Next, the US-tubes were refluxed in 6 N HNO_3 until boiling for 5 min and washed repeatedly with deionized water to pH 7.0. To load the US-tubes with Gd^{3+} ions, the debundled US-tubes were bath sonicated in an aqueous, acidic $GdCl_3$ solution (1 mg/mL, pH 3) for 60 min. The solution was left undisturbed overnight to allow for the gadolinium-loaded US-tubes (GNTs) to flocculate out of solution. Upon discarding the supernatant, the flocculated GNTs were collected by filtration, washed repeatedly with deionized water to remove excess external Gd^{3+} ions, and dried at 60 °C.

Biocompatible solutions of GNTs were made by suspending dry GNTs in 0.17% (w/v) Pluronic F-108 surfactant (BASF Corporation; Florham Park, NJ, USA) via probe sonication for 5 min, followed by centrifugation at 3200 rpm for 10 min to remove unsuspended GNTs. For all studies, the Gd^{3+}-ion concentration of GNT solutions was maintained at 76 μM, as confirmed by inductively-coupled plasma-optical emission spectrometry (ICP-OES). Prior to their addition to cell cultures, GNT solutions were sterilized under UV light while rocking for 3 h.

3.2.2. Cell Culture

MSCs were harvested and isolated from the bone marrow of male pigs as described elsewhere.[53] MSCs were expanded in two successive passages at 2×10^3 cells/cm^2. Cells in the second passage (P_2) were then frozen in cryovials, and at appropriate times, MSCs were thawed and expanded once (P_3) prior to labeling. Cell cultures were incubated at 37 °C (95% relative humidity in 5% CO_2). Unless otherwise specified, MSCs were grown and maintained in alpha minimal essential medium (αMEM) containing 10% fetal bovine serum (FBS) and 1% antibiotic supplement (200mM L-glutamine, 10,000 units/mL penicillin, and 10 mg/mL streptomycin). All labeling studies were performed with P_3 MSCs.

3.2.3. Label Concentration

To determine the optimal labeling concentration, MSCs were initially plated on 6-well tissue culture plates at 2×10^4 cells/well and were allowed to reach 70% confluence. The medium was removed, and the attached cells were co-cultured with GNTs in αMEM at various Gd^{3+} ion concentrations (15-42 μM). After 24 h, the cells were washed with phosphate buffered saline (1×PBS) and exposed to a mild ice-cold acid-strip buffer solution (50 mM glycine-HCl, 100 mM NaCl, and 2 mg/mL polyvinylpyrrolidone at pH 3.0) for 10 min at 4 °C. This has been previously shown to remove up to 95% of membrane-bound ligands without affecting cell viability.[54] The cells were washed again with 1×PBS and lifted upon exposure to trypsin-EDTA for 5 min. The cell suspension of GNT-labeled MSCs was then passed through a 70 μm nylon filter to eliminate large cell-

GNT aggregates and transferred to a 50 mL conical tube. To isolate "cleaned" cells (GNT-labeled MSCs without GNTs on their cellular membranes) from excess GNTs in solution, a density gradient centrifugation method was performed. Briefly, Histopaque® 1077 (25 °C, Sigma-Aldrich; St. Louis, MO, USA) was slowly added to the bottom of the tube at a 1:2 volume ratio (Histopaque:cells). The sample was then centrifuged at 400×g for 20 min. Upon successful separation, GNT-labeled MSCs were located at the interface of the αMEM and Histopaque phases. These cells were then isolated and washed twice with 1×PBS and centrifuged at 1500 rpm for 10 min. (Light microscopy images of the cells during the cleaning protocol are documented in Figure A1 in Appendix A) The cells were counted (Beckman Coulter MultiSizer 3) and prepared for ICP-OES analysis.

3.2.4. Incubation Time

MSCs were plated and grown as described above. The medium was removed, and the cells were co-cultured with GNTs (27 µM Gd^{3+}) in αMEM. The cells were then incubated and collected at various times (1, 2, 4, 8, 12, and 24 h). Upon collection, cells were processed as described above and prepared for ICP-OES analysis.

3.2.5. Cell Viability

MSCs were labeled with GNTs (27 µM Gd^{3+}) for 24 hours and collected as described above. Positive controls (unlabeled MSCs) and negative controls (unlabeled MSCs treated with 70% methanol for 30 min) were also cultured. A LIVE/DEAD® viability/cytotoxicity assay kit (Life Technologies; Grand Island, NY, USA) was used to

determine the viability of the GNT-labeled MSCs. The LIVE/DEAD reagents consist of calcein AM, which fluoresces green upon being cleaved from esterase activity in viable cells, and ethidium homodimer-1, which fluoresces red and can only enter cells with a compromised cellular membrane. To each well, the LIVE/DEAD reagents were added and the culture plates were incubated in the dark at RT for 30 min. Fluorescence-activated cell sorting (BD Excalibur Flow Cytometer) was used to measure fluorescence intensities.

3.2.6. Label Retention

MSCs were plated and grown as previously mentioned above. A pulse-chase protocol was then performed on the MSCs, which includes cell labeling in αMEM containing GNTs (27 μM Gd^{3+}) for 24 h (pulse) and replacing the incubating medium with fresh αMEM without GNTs (chase). Two experimental groups were examined: in Group A, the culture medium remained unchanged for the entire chase time; in Group B, the medium was changed every 24 h during the entire chase time (72 h). The cells and culture media were separately collected at 24, 48, and 72 h after initiating the chase and were prepared for ICP-OES analysis.

3.2.7. Electron Microscopy

MSCs were grown on 175 cm^2 cell culture flasks, incubated with GNTs (27 μM Gd^{3+}) in αMEM for 0.5, 2, 6, 12, or 24 h, and collected. Separate populations of GNT-labeled MSCs were replated in fresh αMEM without GNTs and were collected at 24, 48,

and 72 h. Unlabeled MSCs were also grown as a control group. Once collected, all cell populations (2×10^5 each sample) were separately prepared and centrifuged at 1500 rpm for 10 min to form cell pellets. The cell pellets were fixed in 4% glutaraldehyde for 2 days, washed with 1×PBS, post-fixed with 1% OsO_4 for 1 h, dehydrated through a series of graded alcohol washes, infiltrated with acetone and Epon 812 plastic resin, and embedded with 100% Epon 812 in a mold. Several 1 µm sections (thick sections) were cut and stained with 1% methylene blue and 1% basic fuchsin. Ultra-thin sections (80 nm) were cut from the sample block using an RMC MTXL ultra microtome and mounted on 100-mesh copper grids. The grids were stained with 2% alcoholic uranyl acetate and Reynold's lead citrate. The samples were examined with a JEOL 1250 TEM at 60 kV and equipped with an AMTV 540 digital imaging system at St. Luke's Episcopal Hospital (Houston, TX).

3.2.8. Magnetic Resonance Imaging

For pellet samples, unlabeled and GNT-labeled MSCs were separately prepared and centrifuged into cell pellets in Eppendorf tubes at 10×10^6 cells/tube with 1 mL αMEM. Another cell pellet of MSCs incubated in αMEM with Magnevist® (Gadopentetic acid; Gd-DTPA; 27 µM Gd^{3+}) for 24 h was also prepared. A 1.5 T MRI scanner (Achieva; Philips Health Care, The Netherlands) was used for the *in vitro* cellular MRI studies at room temperature (RT; 25 °C). A transmit-receive head coil was used for the acquisitions. An inversion recovery prepared turbo-spin sequence was used to measure the T_1 relaxation times of the samples (TR = 2500 ms; TE = 13 ms). The acquisition matrix resolution was 0.5 × 0.5 × 2.5 mm acquired over a field-of-view of 45

× 45 mm. Acquisitions were made at 8 different inversion times (TI) from 50-2200 ms and T_1 was calculated using the standard inversion recovery equation.

3.2.9. Elemental Analysis

ICP-OES analyses were performed by a PerkinElmer Optima 4300 DV Inductively-Coupled Plasma-Optical Emission Spectrometer. Five scans were performed for each sample. Gadolinium concentration was detected at 342.247 nm, while yttrium (371.029 nm) was used as the internal drift standard. To prepare samples for analysis, the collected cell samples were transferred to glass scintillation vials and heated with 500 µL 25% $HClO_3$ until boiling. Once the samples turned from yellow to colorless, an additional aliquot of $HClO_3$ was added and heated to evaporation. The samples were then diluted to 10 mL with 2% trace-metal HNO_3 and filtered through a 0.22 µm syringe filter.

3.2.10. Statistical Analysis

Unless otherwise noted, all experiments were conducted in triplicate. Results are presented as mean ± SEM. Statistical analysis between any two groups in the *in vitro* rolling assay was performed using a two-tailed paired Student's t test. Differences were considered statistically significant when $p < 0.05$.

3.3. Results & Discussion

3.3.1. Cell Labeling

Optimal conditions were determined for the magnetic labeling of MSCs with GNTs. Figure 3.1a shows cellular uptake as a function of GNT concentration. The most efficient labeling concentration was found to be at 27 μM Gd^{3+}, which delivered up to 0.98 pg or approximately 10^9 Gd^{3+} ions per cell, without affecting cell viability (98% based on calcein AM-positive cells, LIVE/DEAD assay; Figure A2 in the Appendix A). Complete labeling was achieved by 4 h and remained constant for up to 24 h of incubation, as shown in Figure 3.1b. Similar GNT labeling efficiencies were observed for other mammalian cell types, including breast cancer cells[37] and macrophages.[44] Although this labeling method is an effective way to intracellularly deliver large quantities of metal ions, its results are still considered conservative when compared to other nanoparticle-based labeling techniques. For example, a recent study recorded up to 20 pg of magnetite cationic liposomes, or approximately 10^{11} Fe atoms, were internalized per human MSC after 4 h.[55] Similarly, Gd^{3+}-ion encapsulated C_{60} fullerenes ($Gd@C_{60}$) internalized up to 133.6 pg, or 10^{11} Gd^{3+} ions, per mouse MSC within 2-8 h of incubation.[35] However, a direct comparison cannot be made between the present GNT-MSC system and other nanoparticle-based MSC labeling studies, since cellular uptake is highly dependent on the type of nanoparticle used, their preparation, and their administration to cell cultures.[56]

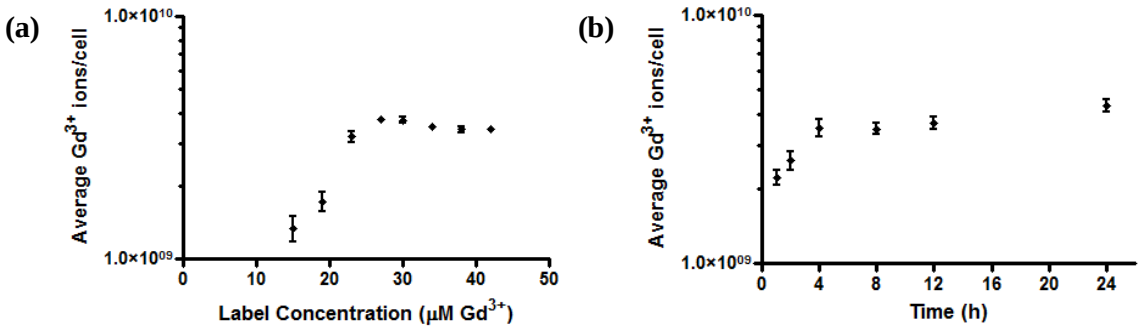

Figure 3.1 – MSC uptake of GNTs as a function of (a) GNT concentration and (b) incubation time. These graphs are plotted on a logarithmic scale. Note: error bars may be smaller than symbols.

Transmission electron microscopy (TEM) visually confirmed the progression of GNT cellular uptake, as depicted in Figure 3.2. As opposed to what is seen in unlabeled MSCs (Figure 3.2a), GNTs appear as irregular electron-dense aggregates within the cytoplasm of MSCs as early as 0.5 h of labeling time. There is no clear indication of GNTs transported into the nucleus. In the early stages of the GNT labeling process (Figure 3.2b-d), TEM images provide evidence of both vesiculated and nonvesiculated GNT aggregates. This observation suggests that GNTs can enter MSCs by either direct membrane penetration or by active endocytosis, both of which have been observed for the internalization of multi-walled CNTs (MWNTs) into human embryonic kidney epithelial cells.[57] However, the GNT aggregates found at 12 and 24 h (Figure 3.2e-f) seem to be too large to be enclosed by any vesicular membrane, which is typically 5 nm in thickness.[58]

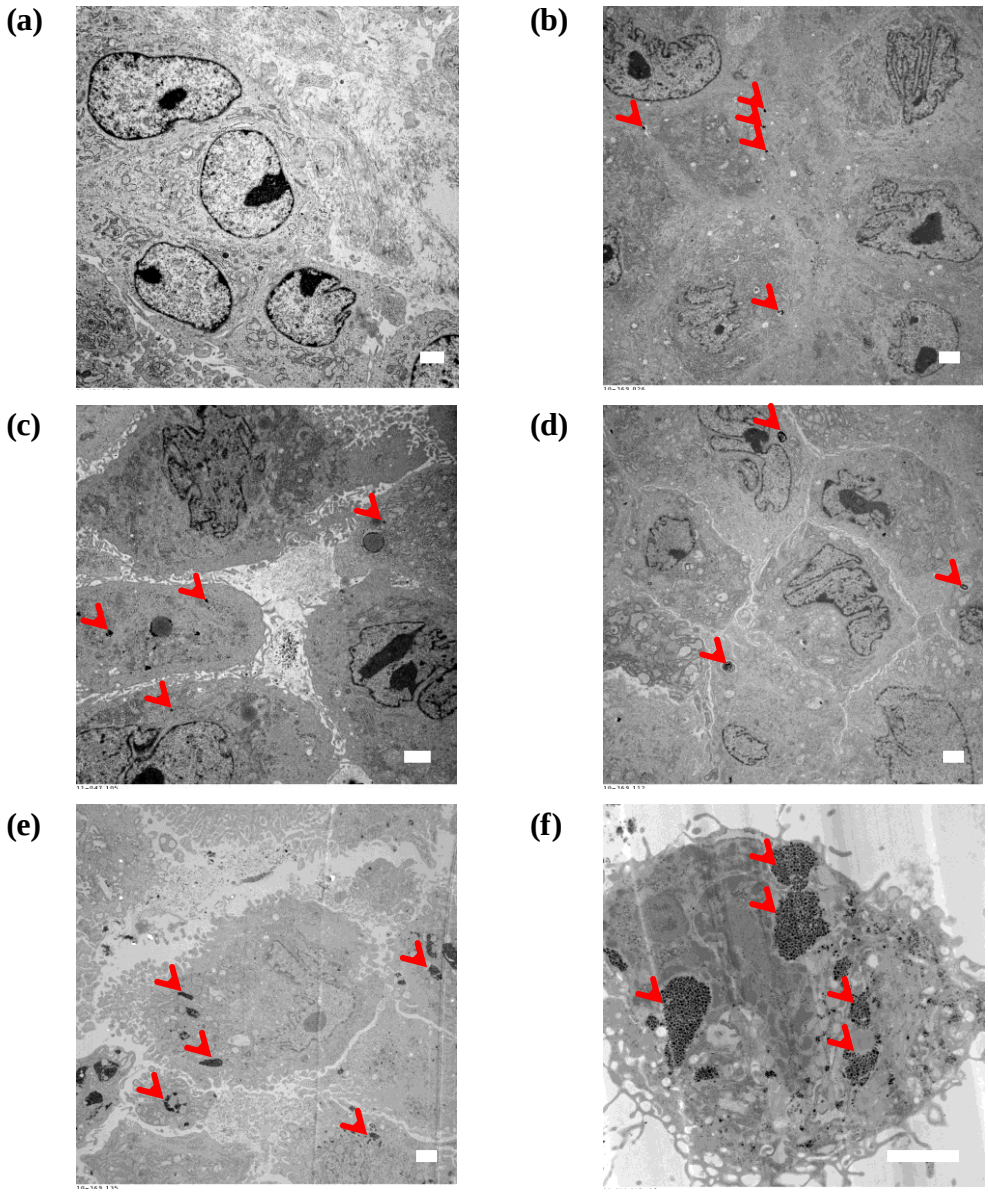

Figure 3.2 – TEM images of (a) unlabeled MSCs and MSCs labeled with GNTs for (b) 0.5 h, (c) 2 h, (d) 6 h, (e) 12 h, and (f) 24 h. Red arrows point to GNT aggregates. Scale bar = 2 µm.

In a separate study, GNT-labeled MSCs were replated in fresh αMEM and collected at 24, 48, and 72 h to examine the intracellular movement of the GNT aggregates after labeling. As seen in Figure 3.3a and b, large GNT aggregates are still

apparent 48 h after labeling. However, the aggregates have migrated towards the cellular membrane at 72 h (Figure 3.3c), suggesting that exocytosis of the GNTs may ultimately occur. Based on these results, GNTs are retained by the MSCs for up to 72 h after labeling. However, a more in-depth study detailing the uptake and eventual release of the GNTs from the cells and the intracellular mechanism of these processes is warranted.

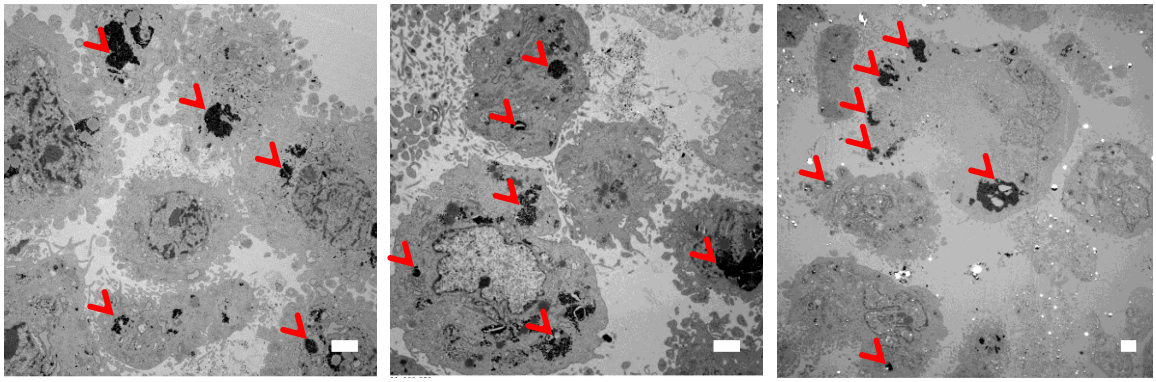

(a) **(b)** **(c)**

Figure 3.3 – TEM images of GNT-labeled MSCs after (a) 24 h, (b) 48 h, and (c) 72 h. Red arrows point to GNT aggregates. Scale bar = 2 µm.

3.3.2. Label Retention

In addition to understanding their mechanism of uptake, the eventual release of GNTs from cells must be considered. To determine whether the GNTs "leak" from the MSCs over time, a pulse-chase study was performed (Figure 3.4). The Gd^{3+}-ion content of the GNT-labeled cells and their culture medium were analyzed under two different experimental conditions. In one set (Group A, gray), no medium changes were performed during the entire chase period (72 h), while in a second set (Group B, black), the medium was replaced every 24 h during the chase period. As seen in Figure 3.4a and b, a decrease

in Gd^{3+}-ion content in the cell samples occurred at 24 h but remained unchanged in both groups for up to 72 h. Conversely, an increase in Gd^{3+}-ion content in the media samples was observed after chasing for 24 h. This initial loss of Gd^{3+}-ion content from the cell samples into the media is likely due to the removal of residual GNTs from the cellular membrane of the MSCs. However, the quantity of Gd^{3+} ions in the media of Group B decreased to an undetectable level by 72 h upon replenishing the media every 24 h, while the quantity found in the media of Group A remained unchanged.

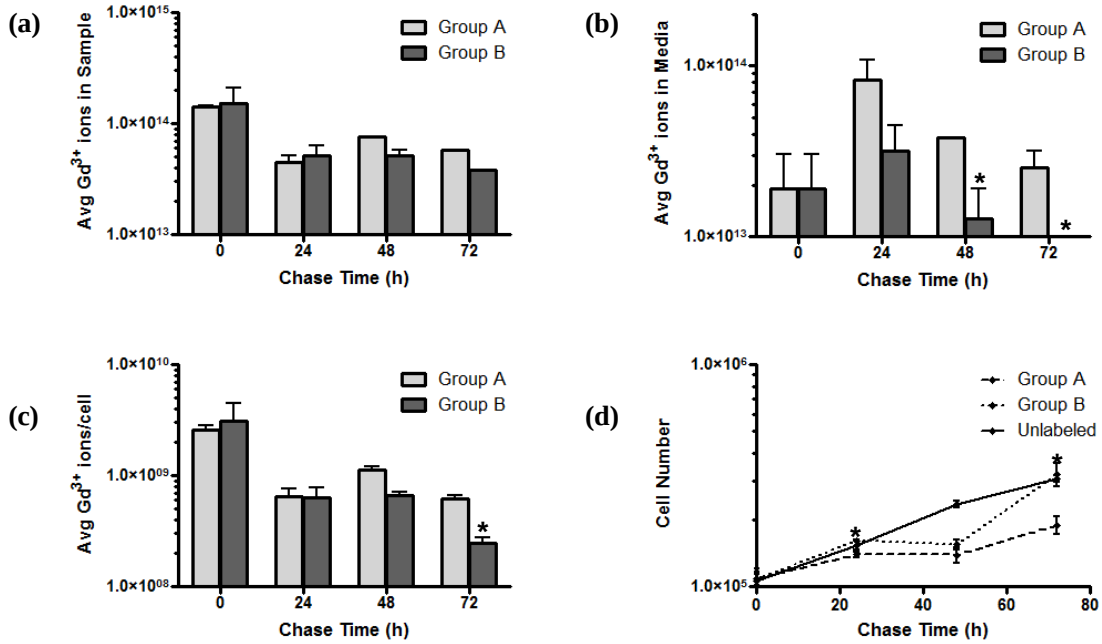

Figure 3.4 – GNT retention in MSCs as a function of chase time: (a) the total average number of Gd^{3+} ions found in the cell samples, (b) the total average number of Gd^{3+} ions in the media, (c) the total average number of Gd^{3+} ions per GNT-labeled cell, and (d) the cell count of each cell sample upon collection. All graphs are plotted on a logarithmic scale. Note: error bars may be smaller than the symbols; * indicates $p < 0.05$ for Group B when compared to Group A.

To better understand the dynamics of GNTs within the cell cultures and whether MSCs retain GNTs for up to 72 h after having been labeled, the average number of Gd^{3+} ions internalized per cell in each group was calculated (Figure 3.4c) based on the cell population of each group over time (Figure 3.4d). From these calculations, it is seen that the average number of Gd^{3+} ions per cell for Groups A and B remained constant between 24 and 48 h of chase time, as the cell populations remained static in an extended growth lag phase (when compared to the proliferation rate of unlabeled MSCs). This stunted cell growth phase suggests that the Gd^{3+} ion content detected in the media may be attributed to natural cell death and/or cell detachment 24-48 h after labeling. However, the quantification of dead cells in the media during the chase period proved to be difficult, since cell debris was mostly observed.

A significant decrease in Gd^{3+} ion content per cell was observed only for Group B after 72 h of chase time. This observed loss in Gd^{3+} ion content may be attributed to either (1) an active release of GNTs from the cells, which would lead to a respective increase of GNT content in the media samples, or (2) cell proliferation, which would divide each culture's total GNT content by a larger cell number and therefore lower the average number of Gd^{3+} ions on a per cell basis. GNT-labeled MSCs from both groups exhibited increased growth rates after 48 h, which implies that the cells eventually adjusted to the presence of the foreign GNT nanoparticles. Additionally, Group B proliferated faster than Group A, suggesting that changing the media, hence removing dead GNT-labeled cells and replenishing nutrients, results in a healthier environment that promoted cell growth. This accelerated proliferation rate corresponded to a decrease in Gd^{3+} ion content on a per cell basis at 72 h. The undetectable amount of Gd^{3+} ions in the

media at 72 h also suggests that no significant loss of intracellular Gd^{3+} ion content by the active cellular release of GNTs occurred. The Gd^{3+} ion content in each cell remained high even after 72 h, with approximately 10^8 Gd^{3+} ions per cell in both Groups A and B.

Although the above results suggest that the loss of Gd^{3+} ions into the media over time is more likely due to cell death and cell detachment rather than to the movement of GNTs across cellular membranes, the release of GNTs from the cells may still possibly occur. Because it is crucial to ensure the GNT-labeled cells lack membrane-bound GNTs, an extensive cell cleaning and separation protocol was used for these studies; however, the initial Gd^{3+}-ion loss from the cells after chasing for 24 h suggests that the cleaning method used is not completely effective in removing all excess GNTs from the cell exteriors. Additionally, the eventual release of GNTs from MSCs due to cell death and their eventual redistribution could impact their performance as *in vivo* magnetic labeling agents and therefore should be further studied.

3.3.3. Magnetic Resonance Imaging Detection

To simulate the number of MSCs in a single injection that will be delivered for the treatment of acute myocardial infarction,[15] MR images were taken of GNT-labeled MSCs, Gd-DTPA-labeled MSCs, and unlabeled MSCs (10×10^6 MSCs/pellet) at various inversion delay (Ti) times (Figure 3.5). Substantial MR signal contrast was generated between the labeled and the unlabeled cells. The T_1 of GNT-labeled MSCs was 494.9 ms (95%, 378-610 ms), the T_1 of Gd-DTPA-labeled MSCs was 1079 ms (CB: 95%, 698-1461 ms), and the T_1 of unlabeled MSCs was 875.9 ms (CB: 95%, 595-1157 ms).

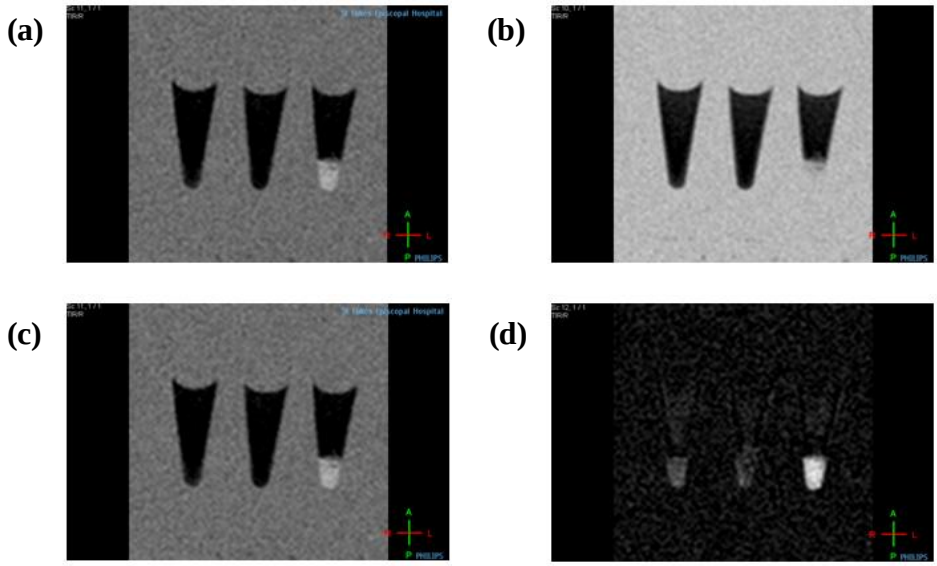

Figure 3.5 – T_1-weighted MR images at 1.5 T and 25 °C of (left to right) unlabeled MSCs, Gd-DTPA-labeled MSCs, and GNT-labeled MSCs at TI = (a) 150 ms, (b) 300 ms, (c) 500 ms, and (d) 800 ms.

With a nearly two-fold decrease in the measured T_1 relaxation time of GNT-labeled MSCs compared to unlabeled MSCs, the GNTs serve as effective *in vitro* magnetic labeling agents, even at low loading concentrations. In comparison to Gd-DTPA, which did not label cells at all under the same conditions, GNTs produced a significant contrast enhancement. However, several challenges still need to be addressed for *in vivo* MRI, such as longer relaxation times and lower contrast produced by tissues, the presence of imaging artifacts, and the inherently low sensitivity of clinical MRI scanners to image on the cellular level. Regardless, the significant T_1 reduction of GNT-labeled MSCs and the lack of cytotoxicity of the GNTs make these carbon nanostructures serious candidates as MRI cell labeling agents for *in vivo* cell monitoring studies.

Chapter 4

Cellular Response to the Intracellular Incorporation of Gadonanotubes

4.1. Introduction

Although GNTs have been shown to effectively label MSCs without compromising cell viability, further assessment of the short- and long-term cellular behavior of GNT-labeled MSCs must be completed before GNTs can be considered for clinical use. Since their regenerative properties, differentiation potential, and immunologic characteristics make MSCs attractive candidates for cellular cardiomyoplasty, these functional properties must be retained after the cells have internalized the GNTs. However, the response of mammalian cells to the intracellular incorporation of CNTs is not well-understood and highly disputed, primarily because the cellular effects observed are highly dependent on the cells examined and the type, length, surface chemistry, and purity of the CNTs used.[59–61] While SWNTs and MWNTs have been shown to inhibit proliferation and differentiation of MSCs[62] and induce oxidative

stress and apoptosis *in vitro*,[59,63–65] other studies have indicated that CNTs are nontoxic and do not adversely affect the behavior of cells and animals.[66–69]

Because of the inconsistent results found among the various toxicological reports on CNTs, a comprehensive study investigating the cellular response of MSCs to GNT internalization is required. More importantly, it must be established whether GNT-labeled MSCs retain their regenerative properties and are suitable for therapeutic applications after having been exposed to GNTs. This chapter reports for the first time a functional and genomic profiling of GNT-labeled MSCs, with a focus on cell phenotype and differential potential, growth kinetics, cell adhesion, and effects on cell cycle mechanisms.

4.2. Materials and Methods

4.2.1. Cell Culturing and Labeling

MSCs were harvested and isolated from the bone marrow of male pigs as described elsewhere.[53] MSCs were expanded in two successive passages at 2×10^3 cells/cm^2. Cells in the second passage (P_2) were then frozen in cryovials, and at appropriate times, MSCs were thawed and expanded once (P_3) prior to labeling. Cell cultures were incubated at 37 °C (95% relative humidity in 5% CO_2). Unless otherwise specified, MSCs were grown and maintained in alpha minimal essential medium (αMEM) containing 10% fetal bovine serum (FBS) and 1% antibiotic supplement

(200mM L-glutamine, 10,000 units/mL penicillin, and 10 mg/mL streptomycin). All labeling studies were performed with P_3 MSCs.

Three cell populations were cultured and used in the subsequent studies: (1) GNT-labeled MSCs, (2) Pluronic-treated MSCs, and (3) unlabeled MSCs. Unless otherwise noted, GNT-labeled MSCs were prepared, processed, and collected as earlier described in Section 3.2.3. For transcriptome analyses, the GNT-labeled MSCs used were prepared in the following manner: after incubation with GNTs (27 μM Gd^{3+}) for 24 h, MSCs were washed three times with 1×PBS and lifted upon exposure to trypsin-EDTA for 5 min. The cell suspension of GNT-labeled MSCs was then passed through a 70 μm nylon filter to eliminate large cell-GNT aggregates. For Pluronic-treated MSCs, cells were incubated in 0.17% Pluronic F-108 in αMEM (35% v/v) for 24 h, washed three times with 1×PBS, and lifted upon exposure to trypsin-EDTA for 5 min. The cell suspension was then passed through a 70 μm nylon filter to eliminate large cell aggregates.

4.2.2. Phenotyping of Cell Surface Markers

Unlabeled and GNT-labeled MSCs were labeled with FITC mouse anti-pig CD45 primary antibody (clone K252-1E4; AbD Serotec, Oxford, UK), PECy5 mouse anti-human CD90 (clone 5E10, BD Pharmingen), FITC mouse anti-human CD105 (clone MEM-229; Abcam), and FITC mouse anti-pig CD29 primary antibody (cloneNaM160-1A3, BD Pharmingen). Data acquisition was performed on a FACS Calibur Flow Cytometer (Becton Dickinson). Unlabeled and GNT-labeled MSCs were analyzed for the expression of various factors, including CD29, CD45, CD90, and a secondary antibody.

4.2.3. Cell Differentiation

GNT-labeled MSCs were grown under adipogenic, osteogenic, or chondrogenic conditions for 14-21 days to evaluate their differentiation potential. The differentiation of positive controls (unlabeled MSCs exposed to differentiation conditions) and negative controls (unlabeled MSCs exposed to only αMEM) were also prepared and monitored.

For adipogenic differentiation, GNT-labeled MSCs were plated and grown in 6-well tissue culture plates at 2×10^4 cells/well. Once 70% confluence was reached, the cells were first grown in adipogenic differentiation medium (10 μg/mL insulin, 10% FBS, 1 μM dexamethasone, 0.5 mM methyl-isobutylxanthine, and 100 μM indomethacine in high glucose DMEM) for 3 days and then grown in adipogenic maintenance medium (10 μg/mL insulin and 10% FBS in high glucose DMEM) for another 3 days. This alternating treatment was repeated twice more to obtain full adipogenic differentiation. The adipogenic cultures were stained with Oil Red O, which identifies the presence of lipid vacuoles within the MSCs.

For osteogenic differentiation, GNT-labeled MSCs were plated and grown in 6-well tissue culture plates at 3×10^4 cells/well. Once 70% confluence was reached, the cells were cultured in osteogenic differentiation medium (10% FBS, 50 μg/mL ascorbate 2 phosphate, 0.1 μM dexamethasone, and 10 mM β-glycerol phosphate in high glucose DMEM) for 21 days, with media replacement every 3-4 days. Upregulated alkaline phosphatase activity, a characteristic of early osteocytes, was observed in GNT-labeled MSCs upon staining the cultures with a Vector Red Alkaline Phosphatase Substrate Kit (Vector Laboratories, Inc.; Burlingame, CA, USA) with a fluorescent microscope.

For chondrogenic differentiation, 2×10^5 GNT-labeled MSCs were transferred into 15-mL conical tubes and centrifuged at 450 rpm for 5 min. The cell pellets were then cultured in the tubes for 21 days in chondrogenic differentiation medium (40 μg/mL proline, 100 μg/mL sodium pyruvate, 10 ng/mL TGF-β3, 0.1 μM dexamethasone, 50 μg/mL ascorbate 2 phosphate, 500 mg/mL BMP-6, and 1% ITS + premix in high glucose DMEM), with media replacement every 3-4 days. The MSCs formed a small spherical mass at the bottom of the tube and were then fixed with 4% paraformaldehyde, embedded in paraffin, and stained with Alcian Blue, which identifies glycosaminoglycans.

4.2.4. Colony-forming unit fibroblast assay

GNT-labeled MSCs were plated in 75 cm^2 tissue culture flasks at 1×10^3 cells/flask in 12 mL αMEM. The cells were cultured for 7 days, with medium replacement every 3-4 days. Control flasks were plated with unlabeled MSCs. To enumerate CFU-F content, cultures were washed with 1×PBS, fixed with methanol, and stained with Giemsa stain. Colonies with 40 or more cells were counted under a stereomicroscope (2-5×).

4.2.5. Population doubling time assay

Unlabeled MSCs, Pluronic-treated MSCs, and GNT-labeled MSCs were prepared and separately replated on 96-well tissue culture plates at 1×10^3 cells/well. At specific time points up to 144 h after seeding, cell proliferation was measured using a CyQUANT® Cell Proliferation Assay Kit (Molecular Probes, Inc.; Eugene, OR, USA)

during the cell growth long lag phase as described by Griffiths et al.[70] In this kit, a green fluorescent dye, CyQUANT® GR dye, exhibits strong fluorescence enhancement when bound to cellular nucleic acids. Briefly, the medium was aspirated from the wells at specific time points and replaced with the CyQUANT® reagent. Fluorescence detection was measured on a microplate reader (TECAN Safire2^{TM}) with filters appropriate for 485/528 nm (excitation/emission). This assay is designed to produce a linear analytical response; therefore, a standard curve was generated by plating known numbers of MSCs on 96-well tissue culture plates and the fluorescence intensity values obtained from them after labeling with the CyQUANT® reagent were used to calculate cell numbers.

4.2.6. Cell Adhesion

Unlabeled, Pluronic-treated, and GNT-labeled MSCs were divided into two groups. The first group was processed with the acid-stripping protocol as described earlier in Section 3.2.3. The second group was prepared in the following manner: after incubation/labeling for 24 h, MSCs were washed three times with 1×PBS and lifted upon exposure to trypsin-EDTA for 5 min. The cell suspension was then passed through a 70 μm nylon filter to eliminate large cell aggregates.

Both groups were exposed to calcein AM (Invitrogen) for 30 min at 37 °C. The cells were then centrifuged for 3 min at 1500 rpm and resuspended in medium. Cells were plated at 2×10^5 cells/well on a 96-well plate treated with various concentrations of either human plasma fibronectin (0-10 mg/mL) or pig collagen I (0-100 mg/mL) and blocked with 2% bovine serum albumin in tris-buffered saline (pH 7.5). After incubating for 30 min at 37 °C, the plate was then gently washed three times with 1×PBS (0.6 mM

$MgCl_2$, 1.2 mM $CaCl_2$) to remove unattached cells. A lysis buffer (50 mM Tris pH 7.5, 1% NP-40, and 5 mM EDTA) was added to allow the fluorescent dye to be released from the cells. Fluorescence measurements were performed on a microplate reader (TECAN Safire2^{TM}) with filters appropriate for 485/530 nm (excitation/emission).

4.2.7. Transcriptome Analysis

Total RNA samples of three sets of GNT-labeled MSCs and unlabeled MSCs from two different pig bone marrow donors were isolated using the Qiagen Micro RNeasy kit and QIAShredder homogenizer (Qiagen, Valencia, CA, USA) following the manufacturer's protocol. The quantity of the extracted total RNA was measured by a Nanodrop ND-1000 spectrophotometer (Nanodrop Technologies, Inc., Wilmington, DE, USA), and RNA integrity was assessed with an Agilent 2100 Bioanalyzer (Agilent, Palo Alto, CA, USA). Transcriptional profiles were assessed using GeneChip Porcine Genome Arrays (Affymetrix; Santa Clara, CA, USA) by the Genomic and RNA Profiling Core at Baylor College of Medicine (Houston, TX, USA). Signal intensities were evaluated by the in-house bioinformatician using the GeneChip Operating Software (Affymetrix). The data was preprocessed using the ITER normalization algorithm (Expression Console Software, Affymetrix). The differential expression analysis was performed using the Significant Analysis of microarrays (SAM) to identify the gene expressions that varied significantly between sample groups.[71] The probe list obtained from the analysis was annotated using the annotation file provided by Tsai et al. 2006.[72] This file identifies 19675 of 24123 transcripts on the Affymetrix Porcine microarray, representing 11265 unique genes, and provides conversion to the human gene accession IDs. The gene list

was uploaded to Metacore (GeneGo, Inc.), and pathway analyses were performed using the GeneGo Pathway Maps ontology. The False Discovery Rate (FDR) was 5%.

4.2.8. Flow Cytometry of Cell Cycle Proteins

Unlabeled MSCs, Pluronic-treated MSCs, and GNT-labeled MSC were prepared and suspended in fresh media at 1×10^6 cells/mL. The cells were pelleted, washed once with 1×PBS, and the supernatant was discarded. To fix cells, the pellets were resuspended in 2 mL methanol and were allowed to sit overnight at -20 °C. The cells were then pelleted, washed once with 1×PBS, and suspended in 500 µL 0.25% Triton X in 1×PBS to permeabilize cellular membranes. The cells were kept on ice for 5 min and washed again with 1×PBS. Next, the cells were resuspended in 100 µL rinsing buffer (1% BSA in 1×PBS) containing 0.5 µg of the primary antibody (rabbit cyclin B1 (clone H-433; Santa Cruz Biotechnology, Inc.; Santa Cruz, CA, USA)) and were left in the dark for 1 h at 4 °C. The cells were then washed with rinsing buffer, resuspended in 100 µL rinsing buffer containing 0.5 µg of the secondary antibody (goat anti-rabbit IgG-FITC (ab6717, Abcam)), and incubated in the dark at RT for 30 min. The cells were washed in rinsing buffer, resuspended in the PI/RNase staining buffer (BD Pharmingen), and incubated in the dark for 20 min at RT. Flow cytometry was done on an LSRII Flow Cytometer (Becton Dickinson). FITC was excited with a 488 nm laser and FITC data were collected through a 530 ± 20 nm band pass filter. A 620 nm long pass filter was used to collected PI emission.

4.2.9. Quantitative Real-time Polymerase Chain Reaction

Total RNA samples of three sets of GNT-labeled MSCs and unlabeled MSCs from three animals were isolated using the Qiagen Micro RNeasy kit and QIAShredder homogenizer (Qiagen, Valencia, CA, USA) following the manufacturer's protocol. Total RNA was transcribed into cDNA using the RT² First Strand Kit (SABiosciences; Valencia, CA, USA) according to the manufacturer's protocol. Expression levels of CKS2 and E2F1 were analyzed by quantitative real-time polymerase chain reaction (RT-PCR) using oligonucletide primers designed from the *Sus scrofa* (pig) mRNA sequence database found on the NCBI website. The sequences of these oligonucleotides are detailed in Table 4.1. All reactions were performed in triplicate using the RT² SYBR® Green qPCR Mastermix (SABiosciences; Valencia, CA, USA) and following the manufacturer's protocol on a 7900HT Fast Real-time PCR System (Applied Biosystems; Foster City, CA, USA). Hypoxanthine phosphoribosyltransferase (HPRT1) was chosen as the reference gene to normalize the amount of total RNA added to the reaction. Data are from at least three different experiments and are presented as relative intensities, normalized to HPRT1 cycle threshold (Ct) values.

4.2.10. Statistical Analysis

Unless otherwise noted, all experiments were conducted in triplicate. Results are presented as mean ± SEM. Statistical analysis between any two groups was performed using a two-tailed paired Student's t test. Differences were considered statistically significant when $p < 0.05$.

Gene	Forward Primer	Reverse Primer	Length (bp)
CKS2	5’-TCAAACCGGGCTCGTTCGGC-3’	5’-TGCAAGAGGGCGGGTAGCCT-3’	139
E2F1	5’-ATCAGCCCCGGGAAGACCCC-3’	5’-CTGGGATCCGTGGCAGGGGA-3’	125
HPRT1	5’-CCGAGGATTTGGAAAAGGT-3’	5’-CTATTTCTGTTCAGTGCTTTGATGT-3’	183

Table 4.1 – Forward and reverse primer sequences of genes analyzed in RT-PCR studies. bp = base pair.

4.3. Results and Discussion

4.3.1. Cell Characteristics after Labeling

As multipotent progenitor cells, MSCs have the ability to differentiate into a variety of cell types. As seen in Figure 4.1, GNT-labeled cultures successfully differentiated into adipocytes, osteocytes, and chondrocytes. Upon appropriate induction, intracellular lipid vacuoles, alkaline phosphatase activity, and glycosaminoglycans were evidenced, respectively demonstrating adipo-, osteo-, and chondrogenic differentiation capacity of GNT-labeled MSCs. This establishes that the magnetic labeling of MSCs with GNTs did not affect the differentiation potential of the MSCs, which suggests that GNT-labeled MSCs may retain their therapeutic potential, which is critical for stem cell therapy. Quantitative analyses will be required to further corroborate the differentiation abilities of GNT-labeled MSCs.

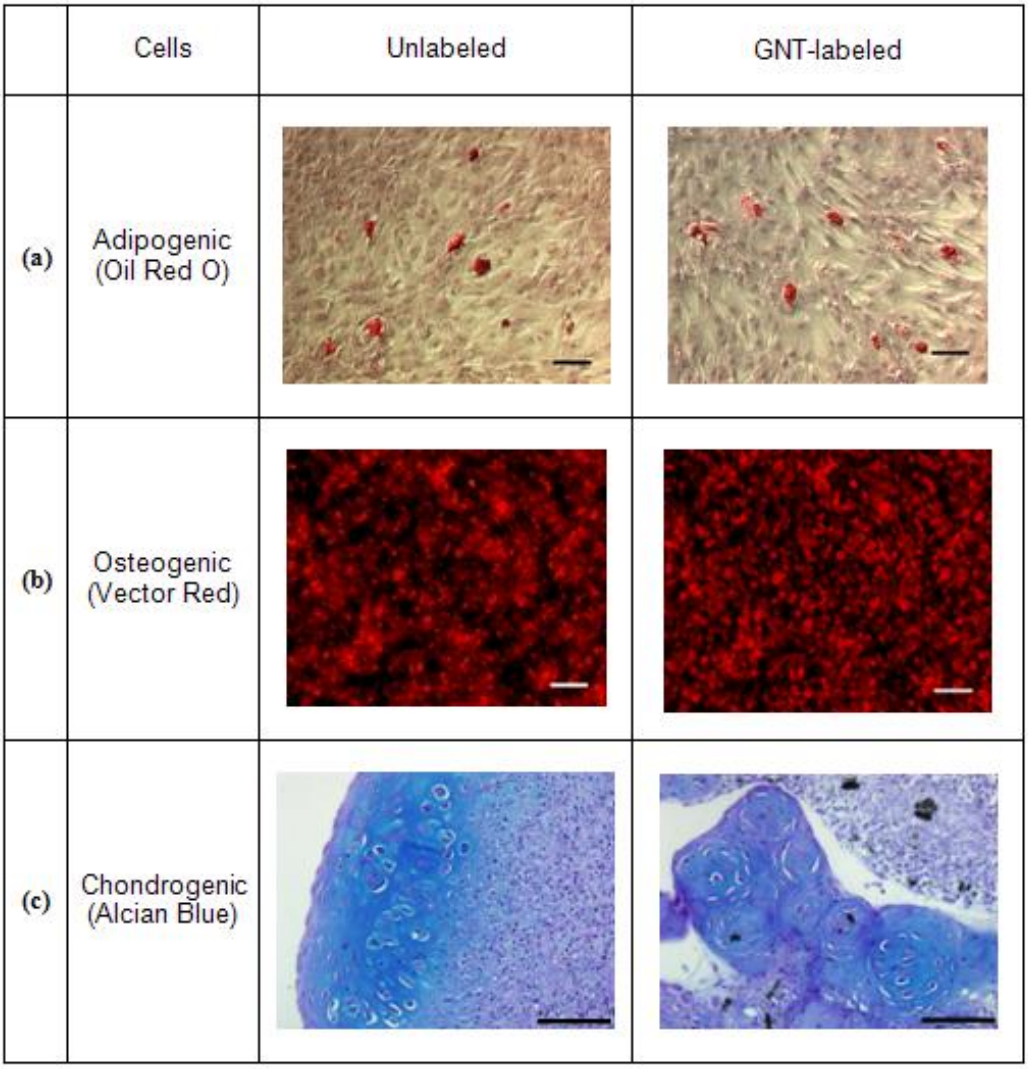

Figure 4.1 – Histochemical stains of unlabeled and GNT-labeled MSCs exposed to (a) adipogenic, (b) osteogenic, or (c) chondrogenic media. In (a), the presence of intracellular lipid vacuoles is stained with Oil Red O; in (b), Vector red fluorescence marks the presence of alkaline phosphatase; in (c), Alcian blue stains the presence of glycosaminoglycans. Scale bar = (a) 50 µm, (b) 50 µm, and (c) 100 µm.

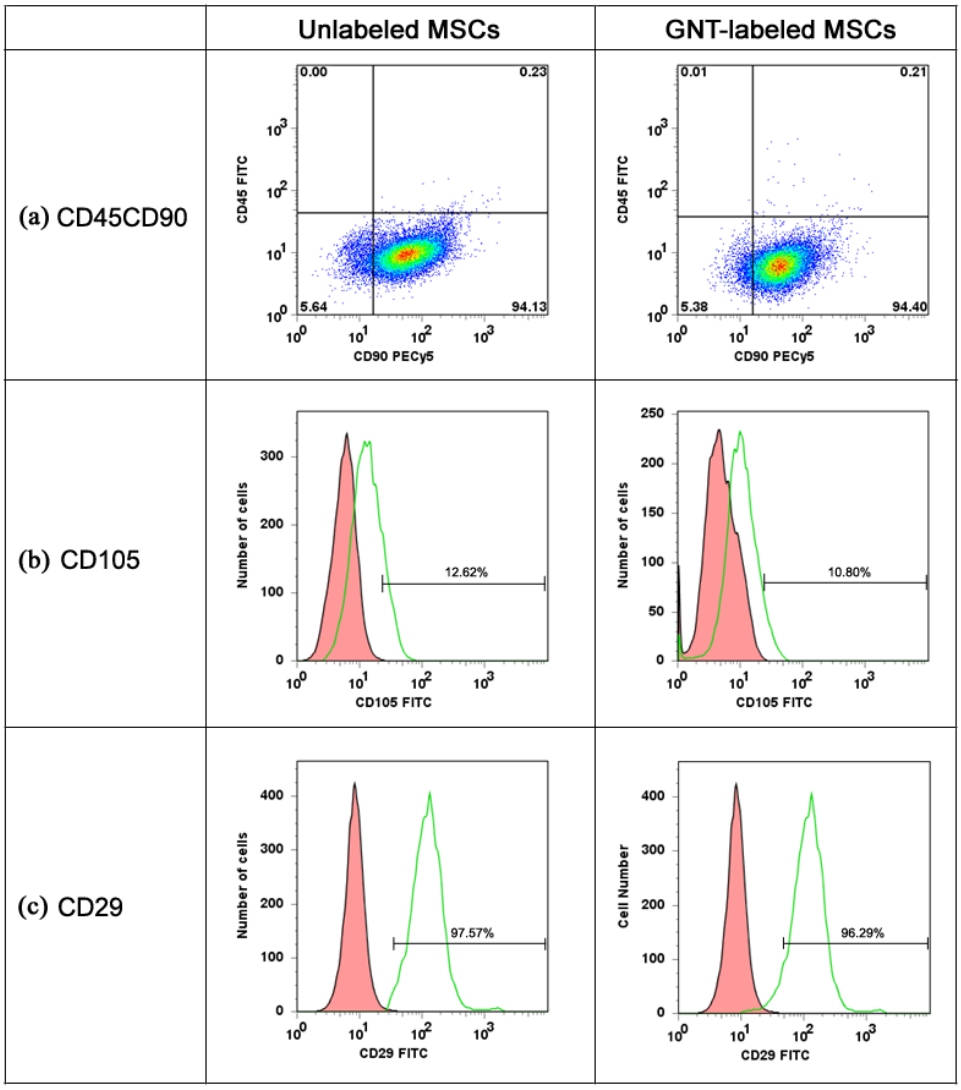

Figure 4.2 – Flow cytometry analysis performed on both unlabeled and GNT-labeled MSCs to determine the expression of CD45, CD90, CD105, and CD29. Histograms represent (a) cells incubated with FITC-labeled mouse anti-pig CD45 and PECy5-labeled mouse anti-human CD90, (b) cells incubated with the FITC-labeled CD105, and (c) cells incubated with FITC-labeled mouse anti-pig CD29. Isotype control, red; MSC samples, green.

Another important cell characteristic is the cell surface marker expression on GNT-labeled MSCs. As such, flow cytometry was used to evaluate the expression of cell surface markers typically used to phenotype human MSCs (CD45, a marker for myeloid cells; CD90, a marker of primitive progenitor cells, and CD105, a truncated TGF-β receptor) upon the GNT-labeled pig MSCs. As seen in Figure 4.2, MSCs are $CD45^-$ $CD90^+$, as expected; however, a small fraction of pig MSCs were $CD105^+$, which differs from human MSCs. Labeled cells displayed similar rates of expression for $CD45^-CD90^+$ (GNT-labeled MSCs: 94.40%; unlabeled MSCs: 94.13%) and also for CD105 (GNT-labeled MSC: 10.80%; unlabeled MSCs: 12.62%) to their unlabeled counterparts. $CD29^+$ (β1 integrin), a ubiquitous cell marker, was expressed by the majority of both unlabeled (97.57%) and GNT-labeled MSCs (96.29%). According to these findings, GNT labeling does not affect the expression of cell surface markers, but a more comprehensive analysis of gene and protein expression is necessary to validate GNTs as innocuous agents for cell labeling. Currently, the effect of GNT labeling on gene expression is being investigated in our laboratories by microarray analysis.

4.3.2. Growth Kinetics

To evaluate the self-renewal properties and proliferation capacity of GNT-labeled MSCs, colony-forming unit fibroblast (CFU-F) and population doubling time (PDT) assays were performed. As seen in Table 4.2, both studies suggest that GNTs do not impair either the self-renewal or the proliferation kinetics of MSCs. In fact, the GNT labeling and Pluronic treatment increased the self-renewal rate of MSCs by approximately 27% and 19%, respectively, after 7 days.

Cells	PDT (h)	Plating Density (cells/well)	CFU-F after 7 days
Unlabeled	25.5	1000	252 ± 11
Pluronic-treated	21.0	1000	301 ± 7
GNT-labeled	22.1*	1000	319 ± 9*

Table 4.2 – Population doubling time (PDT) and colony-forming unit fibroblast (CFU-F) results of unlabeled MSCs, Pluronic-treated MSCs, and GNT-labeled MSCs. *Statistical differences ($P < 0.05$) were observed for both PDT and CFU-F comparisons when compared to unlabeled MSCs.

Since an extended lag phase was observed earlier in the pulse-chase experiment (Section 3.3.2), growth curves of cells derived from three additional animals were generated to depict and confirm the extended lag phase experienced by the GNT-labeled MSCs. As seen in Figure 4.3, both Pluronic-treated MSCs and GNT-labeled MSCs exhibited an extended lag phase lasting 48 h and 72 h, respectively. Interestingly, after starting the growth log phase, both the Pluronic- and GNT-labeled MSCs were able to reach similar cell numbers as unlabeled MSCs by 144 h, suggesting that their rate of cell division was equivalent to the control after the initial growth delay, which is in agreement with the calculated PDT and CFU-F values in Table 4.1.

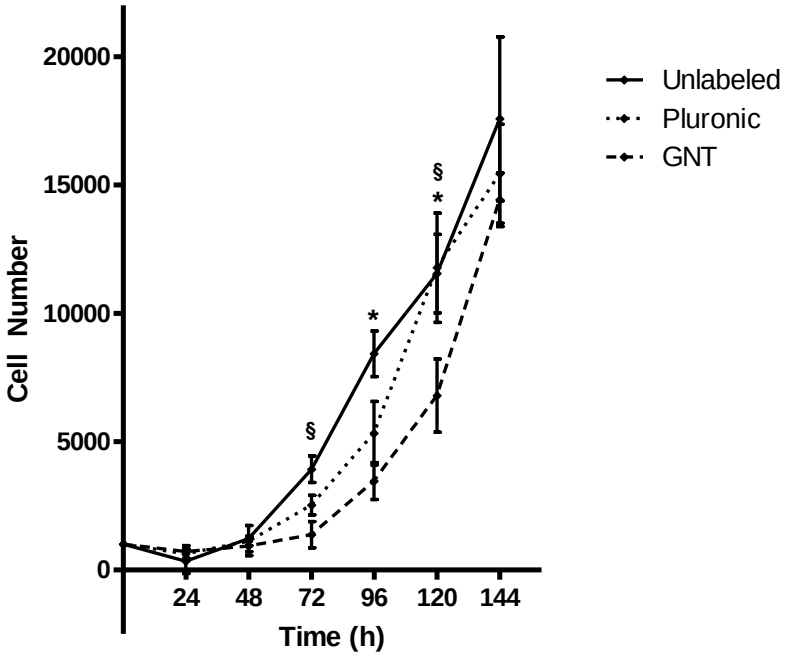

Figure 4.3 – Growth kinetics of unlabeled MSCs, Pluronic-treated MSCs, and GNT-labeled MSCs over 144 h after cell labeling. * indicates $p < 0.05$ when compared to Unlabeled MSCs, and § indicates $p < 0.05$ when compared to Pluronic-treated MSCs.

4.3.3. Cell Adhesion

The effects of GNT labeling on MSC adhesion properties were studied. A cell adhesion assay was used to evaluate the interaction of unlabeled, Pluronic-treated, and GNT-labeled MSCs with collagen I and fibronectin, which are two major components of the extracellular matrix (ECM). Besides serving as structural support for cell adhesion, fibronectin and collagen I are involved in vital cell signaling pathways through their interactions with cell adhesion receptors, such as integrins.[73,74] Ideally, a dose-response curve is observed when measuring the intensity of fluorescently-labeled MSCs that successfully bind to culture plates treated with increasing ECM protein concentration.

Although it has been previously established that the class of Pluronic surfactants can be used as excellent anti-adhesives for cell cultures,[75] Figure 4.4a and b suggests that Pluronic F-108 does not hinder cell adhesion to ECM proteins as significantly as GNTs do. MSCs incubated with Pluronic F-108 behaved similarly to unlabeled MSCs, while GNT-labeled MSCs showed a decreased response to both fibronectin and collagen I. This observation that Pluronic F-108 does not inhibit cell adhesion while in the presence of ECM proteins has similarly been evidenced with neuroblastoma cells.[76] Additional studies are currently underway in our laboratories to determine whether the GNTs are physically blocking cell adhesion receptor sites or chemically altering the cell adhesion properties of the labeled MSCs.

However, it was determined that the acid-stripping protocol used to clean the GNT-labeled MSCs deterred cell adhesion to collagen I (Figure 4.4d). The unlabeled, Pluronic-treated, and GNT-labeled MSCs all lost their ability to adhere to collagen I when treated with the acid strip buffer solution, while those not treated with the acid-strip buffer solution retained their cell adhesion properties. Additionally, the acid-stripping protocol did not affect the cell adhesion response to fibronectin (Figure 4.4c). This suggests that the acid-stripping protocol may be modifying the integrins involved in collagen I adhesion and not those involved in fibronectin adhesion. While the loss of collagen I adhesion may be disadvantageous in some respects, our studies have demonstrated that the acid-stripped GNT-labeled MSCs do not lose their important stem cell characteristics.

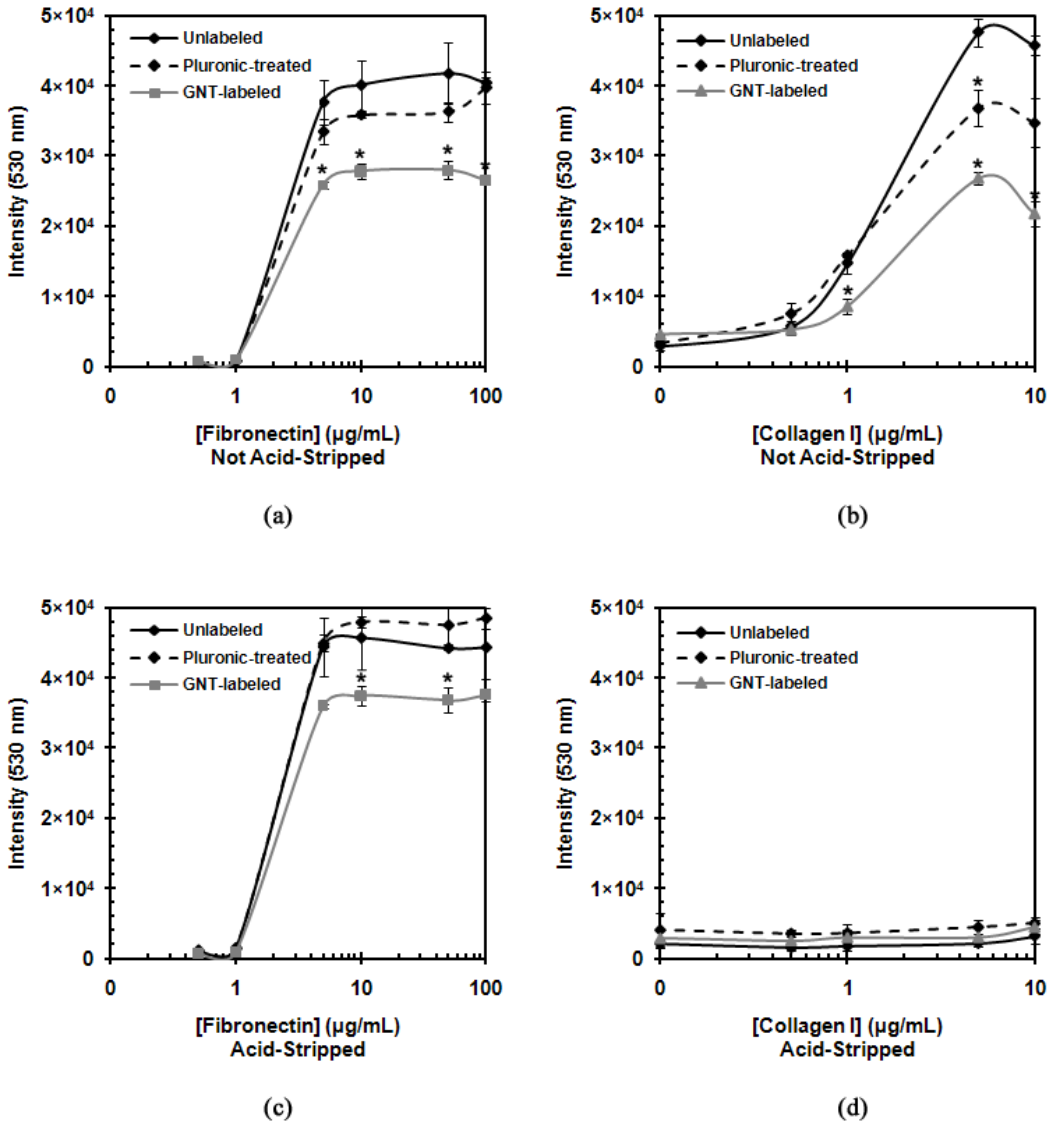

Figure 4.4 – Cell adhesion properties of unlabeled, Pluronic-treated, and GNT-labeled MSCs. Non-acid-stripped MSC response to (a) fibronectin and (b) collagen I. (d) Acid-stripped MSC response to (c) fibronectin and (d) collagen I. Note: error bars may be smaller than the symbols; * represents statistical difference ($P < 0.05$).

4.3.1. Transcriptome Analysis

Transcriptome analysis was performed on samples of concurrently prepared unlabeled MSCs and GNT-labeled MSCs derived from two different animals. Appendix B contains the heat maps corresponding to the 123 genes that were differentially expressed in GNT-labeled MSCs, with 64 genes that were significantly upregulated and 59 downregulated. The differences for both up- and down-regulated gene expression levels were relatively moderate (-5.1 to 5.6), which largely mirrors the observations from the functional evaluation of GNT-labeled MSCs previously described, i.e. a non-apoptotic transient cell cycle arrest (Figure 4.3 and Figure A2 from Appendix A) and some degree of disturbance in cell adhesion properties (Figure 4.4). A survey of the affected genes and their related pathways suggested that GNT labeling led to changes in cellular inflammatory/stress response, oxidative stress response, and the cell cycle (Appendix C).

The cellular stress response is a defense reaction of cells towards damage inflicted by environmental forces on macromolecules (DNA or proteins). The cellular stress response involves physiological mechanisms of sensing membrane lipid, protein, and DNA damage,[77] redox sensing and regulation, cell cycle control, macromolecular stabilization/repair, and control of energy metabolism. If tolerance levels of stress are surpassed, cells are able to activate programmed death (apoptosis). Among the upregulated transcripts detected in GNT-labeled MSCs, several members belong to the *minimal stress proteome*,[77] which are a group of stress proteins found to be conserved in all three living organism kingdoms. These conserved proteins include Superoxide Dismutase (SOD2; +3.9-4.1) and Aldo-keto Reductase (AKR1C4/L1; +3.8). Transcripts

for inflammatory cytokines such as Interleukin-6 (IL6; +4.7) and Leukemia Inhibitory Factor (LIF; +3.9) were also upregulated.

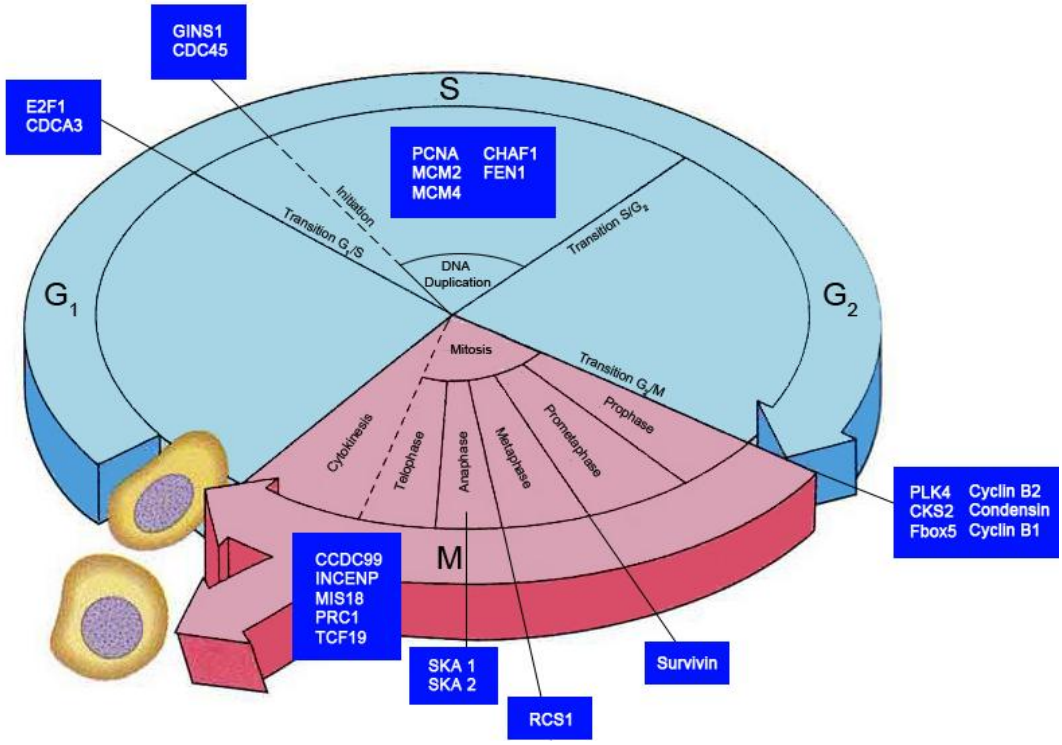

Figure 4.5 – A depiction of the cell cycle and the relevant genes downregulated after the incorporation of GNTs into MSCs.

Transcriptional patterns of apoptosis-associated genes were limited to a few transcripts, such as BIRC5 (also known as Survivin; -3.1) and BNIP3 (+3.1). Another evidence of the stress response by GNT-labeled MSCs comes from the upregulation the nuclear factor of kappa light polypeptide gene enhancer in B-cells inhibitor alpha (NFKBIA; +3.5), which inhibits NF-κB transcription factors from binding to DNA to induce transcription and keeps them sequestered in an inactive state in the cytoplasm.

The transcriptome data analysis clearly corroborates the observations seen in the growth kinetics study in which a transient cell cycle arrest was detected. As shown in Figure 4.5, GNT-labeled MSCs showed a downregulation of 24 transcripts for cell cycle regulators encompassing G1/S transition (E2F1 (-4.2) and CDCA3 (-4.1)), DNA replication (GINS1 (-4.0), CDC45 (-2.8), CHAF1 (-3.7), PCNA (-5.1), FEN-1 (-3.2), MCM-2 (-3.1), and MCM-4 (-3.3)), and termination of the mitotic phase (CKS2 (-3.8), Cyclin B1 (-3.7), Cyclin B2 (-3.1), Condensin (also known as NCAPG; -3.5), SKA 1 (-3.1), SKA 2 (-2.9 to -3.2), Fbox-5 (-4.1), INCENP (-2.9), CCDC99 (-4.3), MIS18 (-3.4), Survivin (-3.1), RCS1 (also known as FAM64; -3.3), KIF23 (-3.4), PLK4 (-3.2), and PRC1 (-3.3)). In addition, significant changes in cell cycle inhibitors were observed, such as the downregulation of TCF19 (-3.9) and the upregulation of Cyclin G2 (+3.4). A description of the 24 transcripts is detailed in Appendix D.

To validate the findings of GNT effects on cell cycle, additional studies were performed using RT-PCR (Figure 4.6) to confirm transcript abundance for CKS2, a protein that binds to the catalytic domain of cyclin-dependent protein kinases and constitutes an essential component for their activity in cell cycle regulation, and E2F1, an essential transcription activator of proteins involved in DNA replication and cell cycle progression from the G1 to S phase. The validation studies were performed with MSCs isolated from animals different (validation samples) from those used for the microarray analysis. The downregulation of CKS2 by GNT-labeled MSCs was confirmed only in samples after overnight exposure to GNTs (Figure 4.6a). No differences were found at 24 and 48 h post-labeling. CKS2 in GNT-labeled MSCs increased with time, indicating that cell cycle mechanisms had been restored. Similarly, E2F1 expression was downregulated

after overnight exposure to GNTs and gradually increased over time (Figure 4.6b). Although statistical significance was not observed due to the small sample size, the data is encouraging but will nevertheless require additional samples.

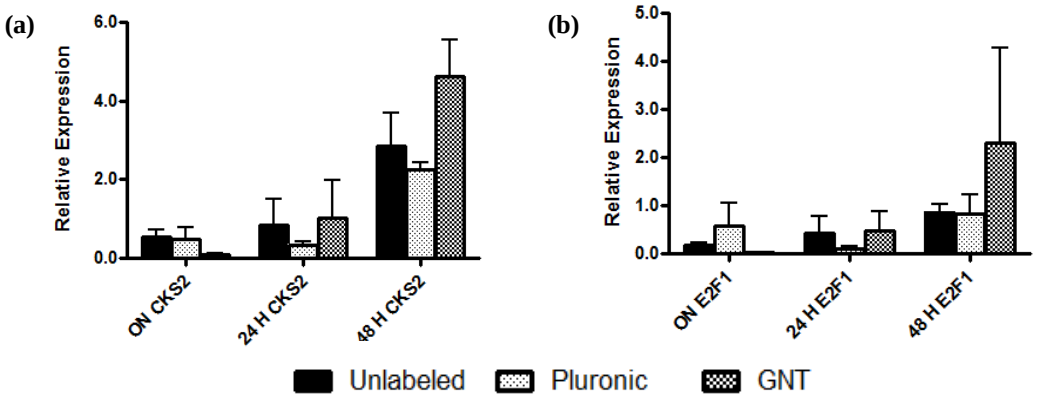

Figure 4.6 – Quantitative Real-time PCR data depicting the relative expression levels of (a) CKS2 and (b) E2F1 over 48 h by unlabeled MSCs, Pluronic-treated MSCs, and GNT-labeled MSCs. All results were normalized to the Ct values of the HPRT1 reference gene.

Cell cycle in GNT-labeled MSCs of the validation samples was further analyzed by flow cytometry using an anti-pig Cyclin B1 FITC-labeled antibody and propidium iodide (PI) staining to determine cell cycle phases by DNA content. Complete flow cytometry figures are provided in Appendix E. Figure 4.7 displays the distribution of cells throughout the distinct cell cycle phases. Figure 4.7b showed a decreased amount of cells in the S phase for GNT-labeled MSCs and Pluronic-treated MSCs, in comparison to unlabeled MSCs, indicating that these cells were less engaged in proliferation than the controls. Cell cycle arrest can be defined by an accumulation of cells in G2/M phase and lower expression of Cyclin B1. As anticipated, an increased amount of GNT-labeled

MSCs in the G2/M population after 24 h (Figure 4.7c) and a significant decrease in Cyclin B1 expression (Figure 4.7d) were observed, which was extended up to 48 h after labeling. With these findings corroborating the previously described results of the functional evaluations, the transcriptome analysis supported the fundamental conclusions that the incorporation of GNTs by MSCs leads to a transient, non-apoptotic cell cycle arrest.

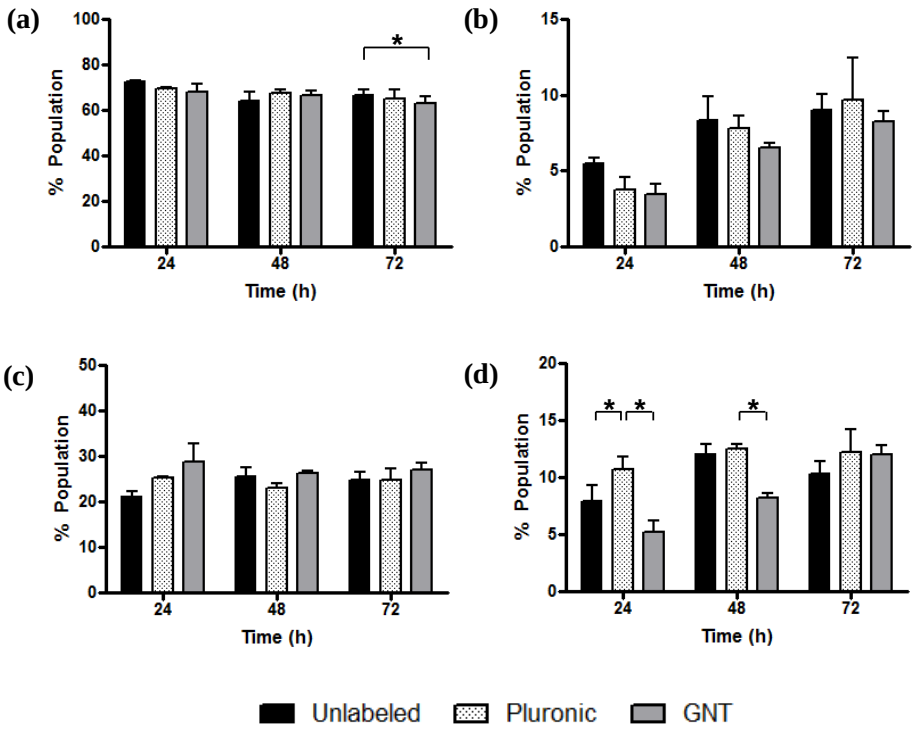

Figure 4.7 – Flow cytometry data depicting the cell population (n = 10,000) distribution in the (a) G0/G1, (b) S, and (c) G2/M phases of the cell cycle and (d) Cyclin B1 expression levels for unlabeled MSCs, Pluronic-treated MSCs, and GNT-labeled MSCs. * indicates statistical significance ($p < 0.05$).

Chapter 5

Gadonanotubes as Magnetic Facilitators for Enhancing Stem Cell Retention

5.1. Introduction

In addition to the inability to noninvasively track cells within the body in real-time, the low rate of retention and survival of transplanted cells remains a challenge in the development of stem cell therapy, irrespective of the cell type, model, and injection method used.[78] When delivering cells to the heart, the high loss of transplanted cells is attributed to the mechanical obstacles presented at the sites of injection, particularly cardiac contraction and blood flow.[79] Because the success of stem cell therapy is strongly dependent on the successful delivery, survival, and integration of the cells, researchers have recently been developing strategies to improve cell retention and viability upon transplantation. One current approach is to target biomolecules such as antibodies, adhesion molecules, and other proteins in order to augment cell adhesion and engraftment.[78] Physical methods have also been developed, such as transplanting cells

embedded into hydrogels[80] or as 3D constructs,[18] to help cells withstand the mechanical challenges in the heart. Additionally, magnetic targeting of superparamagnetic iron-labeled cells has been used to induce cell homing to grafts, stents, and cardiac tissue. This particular approach has proven to be safe and easily translatable to the clinical setting, in addition to being effective in improving both short- and long-term cell retention in the heart.[23,34,81]

Along with being developed as a T_1-weighted intracellular MRI CA, GNTs are presently being used to magnetically improve the retention of transplanted MSCs during cardiac injections. When internalized by MSCs, the superparamagnetic GNTs render the cells magnetically active, thus allowing for GNT-labeled MSCs to be magnetically attracted to an external magnetic field. This chapter describes the *in vitro*, *ex vivo*, and *in vivo* experiments that exploits this phenomenon to develop a new therapeutic application of GNTs as a magnetic facilitator to increase the retention of transplanted stem cells.

5.2. Materials and Methods

5.2.1. Cell Culture and Labeling

MSCs were harvested and isolated from the bone marrow of male pigs as described elsewhere.[53] MSCs were expanded in two successive passages at 2×10^3 cells/cm2. Cells in the second passage (P_2) were then frozen in cryovials, and at appropriate times, MSCs were thawed and expanded once (P_3) prior to labeling. Cell cultures were incubated at 37 °C (95% relative humidity in 5% CO_2). Unless otherwise specified, MSCs were grown and maintained in alpha minimal essential medium

(αMEM) containing 10% fetal bovine serum (FBS) and 1% antibiotic supplement (200 mM L-glutamine, 10,000 units/mL penicillin, and 10 mg/mL streptomycin). All labeling studies were performed with P_3 MSCs.

Four cell populations were cultured and used in the subsequent studies: (1) GNT-labeled MSCs, (2) MSCs labeled with ultrasmall superparamagnetic iron oxide nanoparticles (USPIO-labeled MSCs), (3) MSCs labeled with 20 nm colloidal diamagnetic lutetium (Lu-labeled MSCs), and (4) unlabeled MSCs. GNT-labeled MSCs were prepared by incubating MSCs with GNTs (27 μM Gd^{3+}) for 24 h on 175 cm^2 cell culture flasks and processed as earlier described in Section 3.2.3. For preparing USPIO-labeled MSCs, 125 μL of USPIO nanoparticles (Molday ION(-); 10 mg Fe/mL; Biophysics Assay Laboratory, Inc.; Worcester, MA, USA) was diluted with 400 μL cell culture grade water. To this solution, 12.5 μL PLL (10 mg/mL; Biophysics Assay Laboratory, Inc.; Worcester, MA, USA) was added. The USPIO-PLL conjugate solution was gently vortexed, incubated at 25 °C for 20 min, and stored at 4 °C. Prior to cell labeling, the solution was revortexed, incubated at 25 °C for 20 min, diluted in 12 mL αMEM, and thoroughly mixed. The SPIO-PLL solution was added to 12.5 mL αMEM into each 175 cm^2 cell culture flask to yield a final concentration of 50 μg Fe/mL and 5 μg/mL PLL. After 24 h incubation, the USPIO-labeled MSCs were washed three times with 1×PBS and passed through a 70 μm nylon filter to remove large cell aggregates. To prepare Lu-labeled MSCs, MSCs were incubated in 2 v/v% colloidal lutetium (BioPAL CellTrack™; Biophysics Assay Laboratory, Inc.; Worcester, MA, USA) in αMEM for 24 h, washed three times with 1×PBS, and passed through a 70 μm nylon filter.

5.2.2. Magnetic Cell Adhesion

GNT-labeled MSCs, USPIO-labeled MSCs, and unlabeled MSCs were separately prepared, collected, and suspended at 5×10^5 cells/mL in running buffer (10 mM Tris, 103 mM NaCl, 24 mM $NaHCO_3$, 5.5 mM glucose, 5.4 mM KCl and 2 mg/ml BSA, pH 7.4). Cells were then tested using a parallel plate flow-fluid shear stress rolling assay, which was modified from a previous procedure.[82] Briefly, 24×50 mm slides were cut from 15×100 mm polystyrene Petri dishes. The slides were then washed with 1×PBS, blocked with 2% BSA for 2 h at 25 °C and assembled to a parallel plate flow chamber. To assess the magnetic adhesion of MSCs, a 1.3 T ring NdFeB magnet (RX4C2, K&J Magnetics; Jamison, PA, USA) was attached to the slide. The cells were then injected into the flow chamber and running buffer was drawn through the chamber at a constant force of 1 dyne/cm^2 for 5 min using a computer-controlled syringe pump (Harvard Apparatus; Holliston, MA, USA). The number of adherent cells remaining was recorded by digital microscopy (VI-470 charge-coupled device (CCD) video camera; Optronics Engineering) at 20× on an inverted Nikon DIAPHOT-TMD microscope. The buffer solution that was passed through the chamber was collected and centrifuged to recover cells that were not magnetically retained in the chamber. The recovered cells were fixed with 2% paraformaldehyde in 1×PBS and analyzed by flow cytometry (FACS Calibur BD). A gate using forward and side scatter to distinguish live cells (from debris) was employed. The number of gated events was used to quantify recovered cells (% of cells not retained in the chamber by the magnet), which in turn was used to determine the amount of magnetically adherent cells (% of cells retained in the chamber by the magnet).

5.2.3. *Ex Vivo* Perfusion

An excised bovine heart received three separate 0.2 mL transepicardial bolus cell injections (100×10^6 cells/mL in 2% FBS) approximately 5 mm into the left ventricle (Figure 5.1): (1) GNT-labeled MSCs with a 1.3 T cylindrical NdFeB magnet (D66SH; K&J Magnetics; Jamison, PA, USA) held in place over the injection site using surgical tape, (2) GNT-labeled MSCs without a magnet, and (3) unlabeled MSCs. The injection sites were demarcated with sutures. The heart was perfused with cold saline solution for 72 h, kept in 10% formalin for 24 h, and prepared for histopathological analysis. A 1.7 cm slice, perpendicular to the long axis of the heart, was taken, approximately 6 mm above and 6 mm below the suture marks. The portion of wall containing each injection site was removed from the slice and subsequently sectioned into 5 levels. Adjacent tissue sections were stained with hematoxylin and eosin.

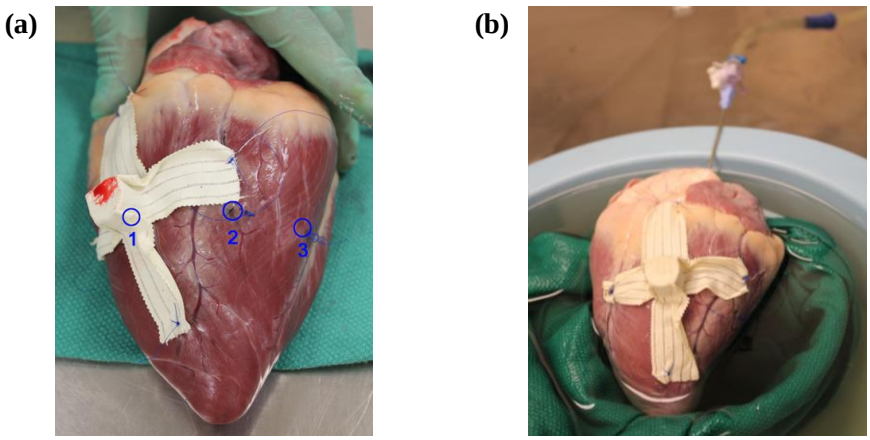

Figure 5.1 –Photographs depicting the *ex vivo* perfusion of an excised bovine heart. (a) Prior to perfusion, GNT-labeled MSCs were injected into the left ventricle at Sites 1 and 2, while unlabeled cells were injected at Site 3. At Site 1, a 1.3 T cylindrical NdFeB magnet was held in place by surgical tape over the injection site. (b) After injection, the heart was perfused with cold saline solution for 72 h.

5.2.4. *In Vivo* Retention

GNT-labeled MSCs and Lu-labeled MSCs were prepared, collected, separately suspended in 2% FBS, and kept on ice in sterile polystyrene tubes until injection. Three aliquots ($0.2\text{-}2\times10^6$) of each cell population were also collected in glass scintillation vials for elemental analysis. All animal care was in accordance to the Institutional Animal Care and Use Committee (IACUC) guidelines of the Texas Heart Institute. Left thoracotomy was performed on female juvenile pigs (n = 12 total) under general anesthesia. A sterilized 1.3 T NdFeB ring magnet (RX4C2; K&J Magnetics; Jamison, PA, USA) was sutured with prolene stitches onto the anterior wall of the left ventricle (Figure 5.2). Cells were gently pipetted prior to the transepicardial injections, which were completed with a 21-gauge butterfly needle around the inner and outer perimeters of the ring magnet. The pigs were divided into the following four groups:

- In Group A (n = 3), 12×10^6 Lu-labeled MSCs were administered in three 0.1 mL injections, followed by 12×10^6 GNT-labeled MSCs in a similar manner. After being maintained in the operating room for 1 h, the animals were euthanized. The left ventricle (LV) encompassing the injection site, the right ventricle (RV), and the paratracheal/periaortic lymph nodes (LN) were collected for analysis.

- In Group B (n = 3), 12×10^6 Lu-labeled MSCs were administered in three 0.1 mL injections, followed by 12×10^6 GNT-labeled MSCs in a similar manner. The thoracic incisions were closed and the animals were monitored during recovery. After 48 h, the animals were euthanized. The LV encompassing the injection site, the RV, and the LN were collected for analysis.

- In Group C (n = 3), 9.6×10^6 Lu-labeled MSCs were administered in six 0.2 mL injections, followed by 9.6×10^6 GNT-labeled MSCs in a similar manner. After being maintained in the operating room for 0.5 h, the thoracic incisions were closed and the animals were monitored during recovery. At 24 h after the time of injection, the animals were euthanized. The LV encompassing the injection site, the RV, and the LN were collected for analysis.

- In Group D (n = 3), 9.6×10^6 Lu-labeled MSCs were administered in six 0.2 mL injections, followed by 9.6×10^6 GNT-labeled MSCs in a similar manner. After being maintained in the operating room for 1 h, the thoracic incisions were closed and the animals were monitored during recovery. At 24 h after the time of injection, the animals were euthanized. The left LV encompassing the injection site, the RV, and the LN were collected for analysis.

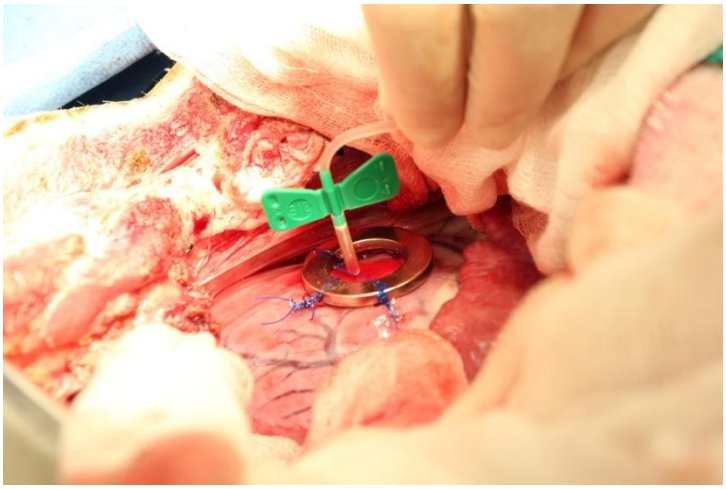

Figure 5.2 – Photograph depicting a typical *in vivo* MSC injection procedure around a 1.3 T NdFeB ring magnet sutured to the left ventricle of the porcine model.

5.2.5. Sample Digestion and Elemental Analysis

All tissue samples were frozen for 24 h and lyophilized for 48 h to remove all water content. In Erlenmeyer flasks with borosilicate glass beads, diced tissue samples were slowly added to 70% trace-metal grade HNO_3 at 110 °C until all tissues were completely dissolved. After having dried for 12 h at 220 °C, samples were treated twice with alternating additions of 25% $HClO_3$ and 70% HNO_3 at 110 °C, allowing for samples to dry in between each acid addition. Samples were allowed to cool, diluted to 30 mL with 2% trace-metal grade HNO_3, and filtered through a 0.22 µm syringe filter.

Cell samples were heated with 500 µL 25% $HClO_3$ until boiling. Once the samples turned from yellow to colorless, an additional aliquot of $HClO_3$ was added and heated to evaporation. The samples were then diluted to 10 mL with 2% trace-metal grade HNO_3 and filtered through a .22 µm syringe filter.

Inductively-coupled plasma-mass spectrometry (ICP-MS) analyses were performed by a PerkinElmer Elan 9000 Inductively-Coupled Plasma-Mass Spectrometer. From the concentration of gadolinium or lutetium ions and the total cell number in each sample, the average metal ion uptake by each cell was calculated and was applied to calculating the amount of cells retained in tissue samples. The measurements were performed in triplicate and the mean and standard deviations of the results were calculated.

5.2.6. Statistical Analysis

Unless otherwise noted, all experiments were conducted in triplicate. Results are presented as mean ± SEM. Statistical analysis between any two groups in the *in vitro* rolling assay was performed using a two-tailed unpaired Student's t test. Statistical analysis between any two groups in the *in vivo* retention studies was performed using a one-tailed paired Student's t test. Differences were considered statistically significant when $p < 0.05$.

5.3. Results and Discussion

5.3.1. Cell Adhesion

To assess whether cellular magnetic labels, such as GNTs and USPIOs, render MSCs magnetically active, a modified parallel-plate fluid flow chamber rolling assay was performed. Conventionally, this assay is used to evaluate cell adhesion to and movement over various proteins and other small molecules that have been immobilized on a glass slide, over which a fluid sheer stress is applied to mimic the dynamic fluid flow in physiological environments.[82] Rather than studying chemical adhesion, this present study observed the magnetic adhesion of GNT-labeled MSCs, USPIO-labeled MSCs, and unlabeled MSCs to a 1.3 T NdFeB ring magnet attached to the glass slide. After having been challenged with a constant fluid shear force of 1 dyne/cm^2 for 5 min, approximately 56.9% of GNT-labeled MSCs were magnetically retained on the slide; in comparison, 90.7% of USPIO-labeled MSCs were magnetically adherent (Figure 5.3). While not as

magnetically active as USPIO-labeled MSCs, GNT-labeled MSCs demonstrated a significant attraction to an external magnetic field, even when challenged under similar mechanical stress normally experienced by vascular smooth muscle cells.[83]

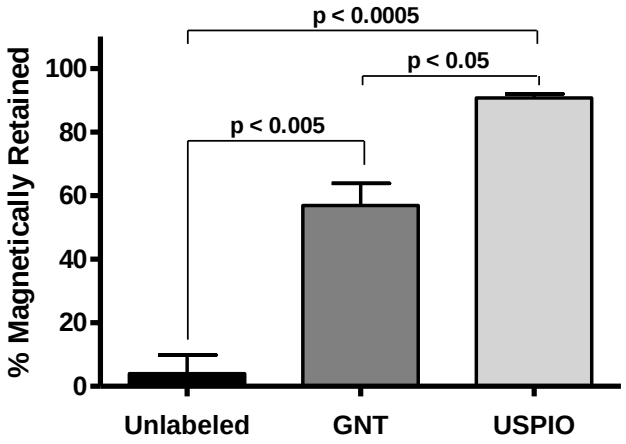

Figure 5.3 – Magnetic retention of unlabeled MSCs, GNT-labeled MSCs, and USPIO-labeled MSCs in a modified parallel-plate fluid flow chamber rolling assay.

5.3.2. *Ex Vivo* Perfusion

Upon discovering that GNT-labeled MSCs are attracted to a nearby external magnetic field, *ex vivo* perfusion studies using bovine hearts were completed to demonstrate that the proximity of an external magnet improves the retention of GNT-labeled MSCs injected into cardiac muscle. After 72 h perfusion, drainage of the dark GNT-labeled MSCs was observed in the epicardial vein above Site 2 (Figure 5.4a).

Pathological analysis of the bovine heart suggests that the external magnet assists in concentrating the injected GNT-labeled MSCs at the target site, as opposed to both

unlabeled MSCs and GNT-labeled MSCs without a magnet, which disseminate throughout the tissue and vasculature (Figure 5.4b and c). The tissue slice containing Site 1 showed an area of GNT-labeled MSCs 4-5 mm in diameter located approximately 5 mm from the epicardial surface. Microscopic analysis showed concentrated clusters of GNT-labeled MSCs at interstitial spaces, with little signs of additional dissemination. At Site 2, a smaller area of GNT-labeled MSCs approximately 3 mm in diameter consisting of several small black clusters was found less than 2 mm from the epicardial surface. In addition, the subendocardial region showed areas of grayish discoloration, suggestive of the presence of disseminated GNT-labeled MSCs. The GNT-labeled MSCs were found in interstitial spaces in smaller clusters than those at Site 1, as well as in the lumen of various epicardial capillaries and veins. Similarly for Site 3, small clusters of unlabeled MSCs were found approximately 2 mm from the epicardial surface. Dissemination of the MSCs was also apparent throughout various nearby venous cavities.

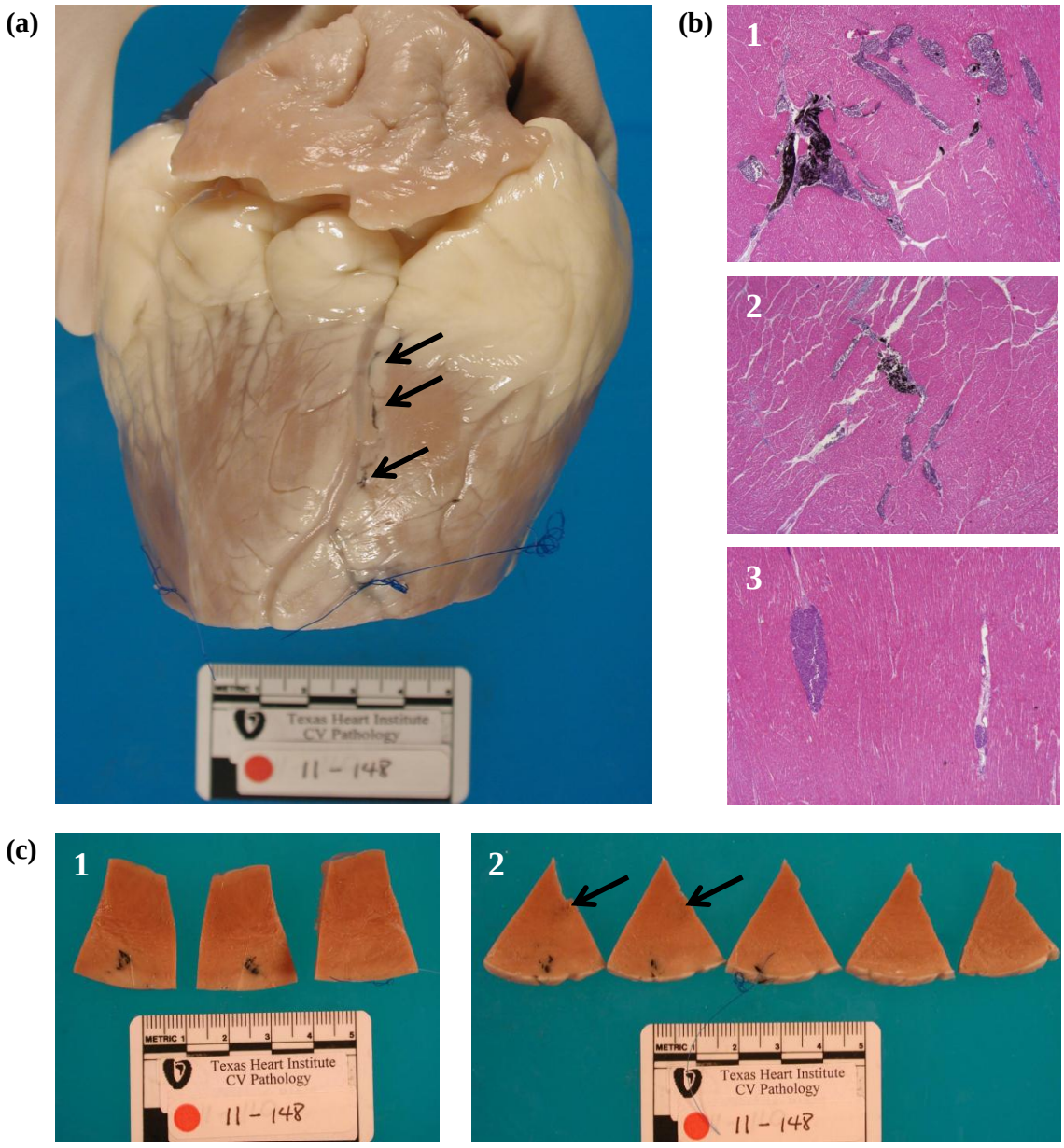

Figure 5.4 – (a) Photograph of the perfused heart after formalin fixation. Arrows denote venous drainage of GNT-labeled MSCs was seen above Site 2. (b) H&E staining of Injection Sites 1, 2, and 3. Magnification: 4×. (c) Various levels of the tissue segments containing Injection Sites 1 and 2. Arrows denote an area of grayish discoloration, suggestive of disseminated GNT-labeled MSCs.

5.3.3. *In Vivo* Retention

To simultaneously assess the retention efficiency of magnetically-facilitated cell injections and the biocompatibility of a sutured strong magnet to the left ventricular epicardium, four *in vivo* porcine model groups were studied, each with varied times of magnet exposure and times of sacrifice. In addition to being a well-established model in safety and efficacy for cardiovascular studies, swine is preferred over smaller animal models (such as mice and rats) for its similarities to human cardiovascular anatomy, physiology, and remodeling kinetics. Groups A and B evaluated the short-term (1 h) and long-term (48 h) tolerance of the magnet, while Groups C and D examined the optimal amount of time needed (0.5 or 1 h, respectively) for the magnet to be applied to the heart before the pigs were sacrificed at 24 h after cell injection. To serve as a control, a population of MSCs was labeled with diamagnetic colloidal lutetium, which can be quantifiable upon elemental analysis.

All treated pigs remained viable and showed no signs of physiological or behavioral trouble for the duration of the experiment. However, an inflammatory response was apparent around the magnet after having been sutured to the heart for 48 h in Group B (Figure 5.5). Test groups evaluating longer-term *in vivo* magnet exposure for 7 days and 30 days are currently underway.

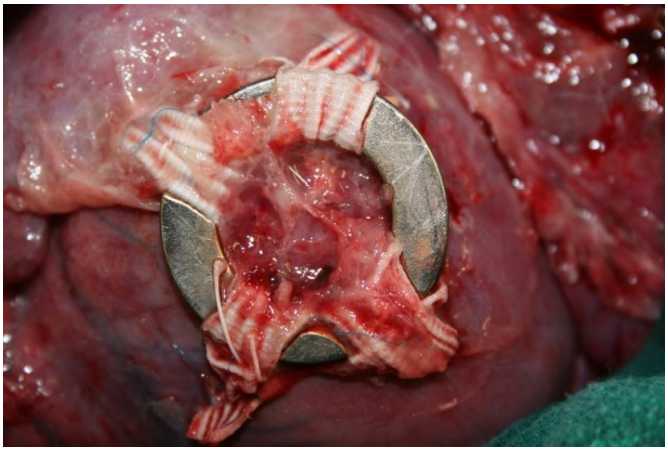

Figure 5.5 – Photograph depicting the heart's inflammatory response to the sutured magnet after 48 h in a pig of Group B. Courtesy of Luiz Sampaio, M.D.

In vivo injection studies corroborated the *ex vivo* perfusion study results, demonstrating that magnetic facilitation can improve transplanted MSC retention at target injection sites in the heart. As seen in Figure 5.6, the retention efficiency of GNT-labeled MSCs is approximately twice as that of Lu-labeled MSCs. While one out of every three pigs in each group retained equivalent amounts of GNT-labeled MSCs and Lu-labeled MSCs at the injection site (Figure 5.6 insets), the majority of the pigs retained between 1.5 to 3.3 times more of GNT-labeled MSCs than the diamagnetic Lu-labeled MSC control, irrespective of magnet exposure or sacrifice times. This is similar to the retention rates exhibited by magnetically targeted iron-labeled cardiosphere-derived cells injected into mouse hearts after 24 h.[23] Interestingly, a significant amount of GNT-labeled MSCs were detected in the right ventricle and the paratracheal/periaortic lymph nodes, with retention numbers increasing with longer sacrifice times; however, negligible amounts of Lu-labeled MSCs were detectable in the these control tissue samples, suggesting the majority of these cells are primarily lost by vasculature flow.

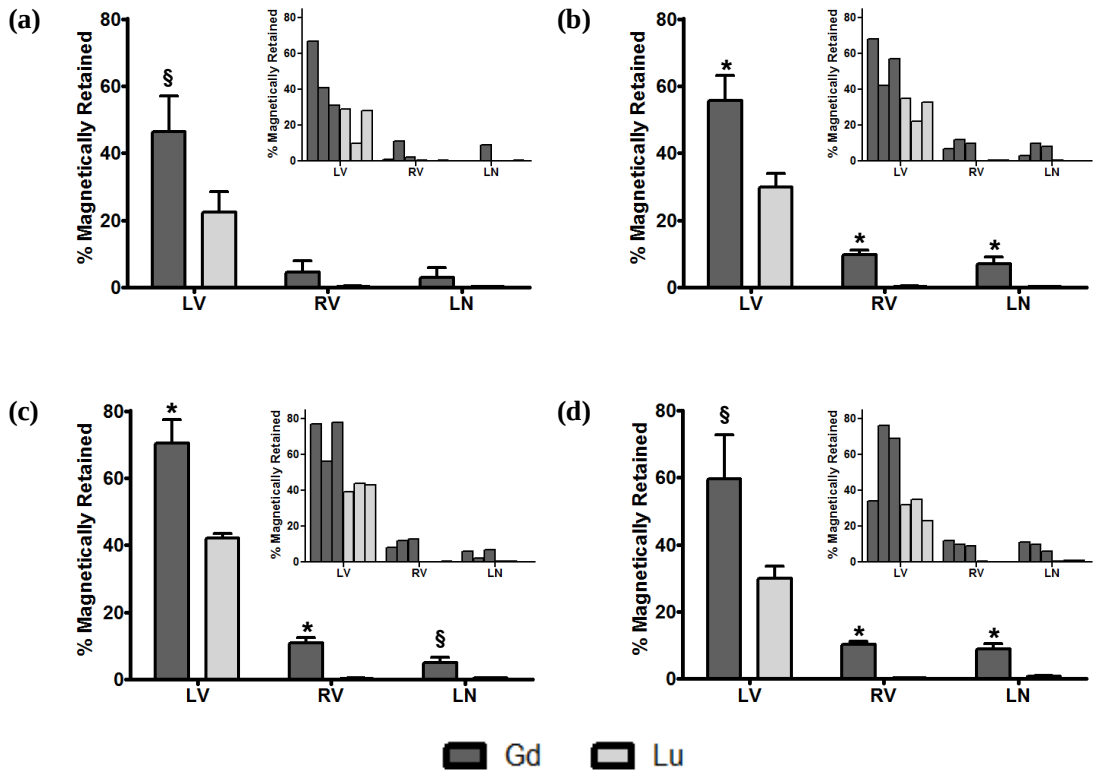

Figure 5.6 – Retention efficiencies of GNT-labeled MSCs (Gd) and Lu-labeled MSCs (Lu) in the left ventricle (LV), right ventricle (RV), and paratracheal/periaortic lymph nodes (LN) of each *in vivo* porcine model of (a) Group A, (b) Group B, (c) Group C, and (d) Group D. Insets illustrate the histographic distribution of each pig sample (n = 3). * indicates $p < 0.05$ when compared to Lu, and § indicates $p < 0.1$ when compared to Lu.

Because there is no clear advantage to longer magnet application times (48 h) over shorter times in terms of retention efficiencies, future studies should have short magnet application times for surgical simplicity. Similarly, cell retention rates are similar between Groups C and D (Figure 5.6c and d, respectively), suggesting more experiments are warranted to determine the optimal magnet application time.

The presented *in vivo* study has several limitations that must be addressed in future studies. First, the current method of transepicardial injections may not be the most practical and optimal means of cell transplantation. During many of the experiments, cell injection solutions leaked from the tissue injection sites immediately after syringe needle extraction due to the backpressure of the tissue, resulting in a significant source of cell loss. Additionally, dark gray residue, suggestive of GNT-labeled MSCs, was found on the surface of the sutured magnet after tissue extraction in Group B. This observation implies that the magnet may be extracting GNT-labeled cells through the channels created by the syringe needle over time, which presents another source of cell loss. A possible solution to this issue is to endocardially deliver cells around an epicardially-sutured magnet, which would allow for cardiac muscle to physically separate the magnet from the cells and needle channels created. Additionally, the inability to avoid injecting cells directly into cardiac veins and other types of vasculature presents an inherent source of cell loss. While the present results are promising, the number of test subjects in each group must be increased to provide more statistically-relevant results.

Second, different experimental variables must be optimized to determine the most effective method of cell transplantation and magnetic retention. The optimal cell type, cell dose, timing of delivery, location of delivery, and delivery technique all currently remain unknown to researchers studying cardiac cell therapy.[84] These factors must first be determined in order to better realize the benefit of magnetically facilitating cell retention with an external magnetic source. Also, the most effective magnet type, strength, and placement method must be established.

Lastly, more effort is needed to improve the clinical feasibility and translatability of the current method. Conventionally, transendocardial and intracoronary injections are preferred for stem cell therapy, with the intention of keeping procedures as noninvasive as possible.[85] As such, a new method must be developed to introduce a strong magnet field source proximal to the injection sites in a minimally invasive manner. The magnetic source must also be biocompatible and clinically practical (i.e. not interfering with surgical procedures and medical equipment). Additionally, ischemic models should also be used in future studies to better mimic the physiological conditions found in patients' hearts and to better assess the effectiveness of magnetic cell retention.

Although the present study is nascent and requires further improvement, the current results have clearly demonstrated that GNTs are effective magnetic facilitators. In addition to being preclinically safe, the proposed method of cell transplantation has proven to be effective in increasing GNT-labeled MSC retention in the presence of an external magnetic field when compared to control cells. As possibly the first T_1-weighted MRI intracellular theranostic agent, it is expected that the GNTs may greatly improve the efficacy of current cell therapies for the treatment of cardiac disease.

Chapter 6

Conclusions and Future Work

6.1. Conclusions

With over 2,000 stem cell-based clinical trials currently underway, the need for better *in vivo* cell tracking technologies is apparent. With such technologies in place, the development of stem cell-based therapeutics for the prevention, detection, and treatment of human diseases should progress more rapidly, since cell tracking helps elucidate stem cell migration and tissue integration, determine the effective dose of delivered stem cells to a target organ, and monitor cell-based therapeutic delivery.

This work describes the successful intracellular labeling of MSCs with GNTs, as confirmed by TEM imaging and elemental analysis. It is also seen that GNTs are not released from the cells for up to 72 hours after incorporation. The GNT-labeled MSCs produce a brighter T_1-weighted MR phantom image and exhibited a nearly two-fold decrease in T_1 relaxation when compared to unlabeled MSCs, implying that the GNTs

represent a new, high-performance biotechnology for stem cell labeling and possibly *in vivo* cell tracking by real-time MRI. With the possibility of becoming the first T_1-weighted MRI intracellular imaging agent, the GNTs could become a new paradigm for the *in vivo* labeling of any mammalian cell.

Before translating this technology into the clinic, the short- and long-term cellular response to the intracellular incorporation of GNTs needs to be assessed. As profiled by various *in vitro* assays, GNTs can successfully be internalized by MSCs without affecting cell viability, differentiation potential, or phenotypic characteristics. However, GNT-labeled MSCs show decreased adhesion to collagen and fibronectin and demonstrate an extended growth lag phase (48 h) when compared to unlabeled MSCs (24 h). A comprehensive transcriptome analysis indicates that more than 130 genes were significantly altered, including those involved in cell cycle, DNA damage, and stress response pathways. Supporting data confirm that a non-proliferative, non-apoptotic growth arrest is effectively occurring in GNT-labeled MSCs. Nonetheless, these events are found to be transient, as GNT-labeled MSCs exhibit the same adhesion properties and growth kinetics profile as unlabeled MSCs shortly after this lag phase.

Along with being developed as an intracellular MRI agent, the magnetically-active GNTs can be used as a magnetic facilitator to improve the retention of GNT-labeled MSCs in cardiac tissue during cardiomyoplasty. Because transplanted cell retention is low by any current method of delivery,[14] innovative and translatable strategies to improve cell homing and survival, which translate into better therapeutic outcomes of cardiomyoplasty, are highly desirable. Upon discovering that GNT-labeled MSCs are attracted to an external magnetic source, results from *in vitro* rolling assays

and *ex vivo* perfusion studies further corroborate that the proximity of an external magnet concentrates GNT-labeled MSCs at targeted sites of injection, even after being challenged by fluid shear force perfusion mechanics. The completed *in vivo* porcine injection studies clearly demonstrate that the GNTs are effective magnetic facilitators in improving the retention of transplanted cells by up to three times more than unlabeled MSCs in cardiac tissue. Additionally, these *in vivo* experiments have proven the epicardial suturing of a strong magnet to be safe and feasible to translate towards clinical use. With the joint properties of producing T_1-weighted MRI contrast and magnetically improving cell retention, the GNTs are conceived to be the first T_1-weighted MRI intracellular theranostic agent, which can be used to augment the efficacies of stem cell-based cardiomyoplasty and other cell therapies for the treatment of human diseases.

6.2. Future Work

6.2.1. Cell Labeling

The intracellular mechanisms of GNT uptake and eventual release need to be elucidated. Although it has established that GNTs readily internalize into MSCs and are retained up to 72 h, more work needs to be performed to determine the exact type of endocytic and exocytic pathways employed. Additionally, it would be interesting to observe the intercellular distribution of GNTs during cell division. Kim et al. noted that polystyrene nanoparticles are not expelled from cells but are rather divided between daughter cells when the parent cell divides, eventually leading to the dilution of the

nanoparticles over several cycles of cell division.[86] It would be interesting to determine whether GNTs follow a similar dilution fate, which would impact the long-term MRI visualization of daughter cells, as described below.

6.2.2. Cellular MRI

A recent study by Tang et al. noted that GNTs exhibited a decrease in T_1 enhancement and an increase in T_2 and T_2* performance when internalized into macrophages.[44] The authors postulated that this phenomenon can be attributed to the slower water exchange rate within cells, the high-density intracellular compartmentalization of GNTs, and the possible susceptibility effects produced by the residual catalyst impurities remaining from their SWNT precursors, which have also been shown to be T_2-weighted agents.[87]

After observing the dense intracellular GNT aggregation from the TEM images in Figure 3.2, it is expected that GNT-labeled MSCs should also exhibit a reduction in T_1 enhancement, which was evidenced by only a two-fold decrease in T_1 relaxation time when imaging cells in a 1.5 T clinical MRI scanner. It is also anticipated that the large GNT aggregates could also amplify the T_2/T_2* performance of the GNTs; therefore, a comprehensive T_2-weighted imaging study should be completed to observe this effect. Another interesting approach would be to examine the dependence of T_1 and T_2 performance on intracellular GNT aggregation and to perform a time-dependent MR imaging study of MSCs internalizing GNTs. Assuming that the water exchange dynamics is faster and GNT aggregation is lower outside of cells, the T_1 performance of the GNTs

should be higher when residing extracellularly; in contrast, T_2 enhancement dominates intracellularly due to the slower water dynamics and the existence of dense GNT aggregates. Therefore, it is expected that diminished T_1 performance and a respective increase in T_2 enhancement should be observed as GNTs are gradually internalized by MSCs. The opposite result is expected if GNTs are diluted through several cell divisions, allowing for T_1 to dominate for daughter cells.

6.2.3. Cellular Response

Although Chapter 4 primarily focused on the changes in cell cycle mechanisms of GNT-labeled MSCs, the information collected by the completed transcriptome analysis, which detected over 130 genetic changes, can spawn several future studies that detail the downstream outcome of intracellular GNT incorporation. Other cellular pathways of interest include cellular adhesion behavior, endocytic and exocytic mechanisms, and immune response to GNTs. In addition to adding more test samples to demonstrate statistical significance for the genetic profiling of GNT-labeled MSCs, more work analyzing the cell proliferation and adhesion behavior of GNT-labeled MSCs over longer periods of time is needed to determine whether GNT-labeled MSCs fully recover from the mild effects experienced by the cells after GNT incorporation.

6.2.4. Magnetic Retention of Cells

In addition to the future work discussed at the end of Chapter 5, it is suggested to repeat all magnetic retention studies using GNT-labeled MSCs that have been labeled 48 h prior to cell injection. As described in the previous studies, GNT-labeled MSCs that have been cultured for 48 h recover from their transient growth lag phase and regain their cell adhesion properties, while retaining the same amount of GNTs as from the time of cell labeling. The recovery of normal cell growth and adhesion may be critical for increasing the chances of cell survival and engraftment after transplantation, which in turn may lead to a more positive therapeutic outcome.

To fully realize the theranostic potential of the GNTs for cellular cardiomyoplasty, all future *in vivo* experiments should be interfaced with concurrent MRI tracking studies of the engrafted cells within the animal models. Rather than performing elemental analyses of extracted tissues, MRI visualization will be preferred in the clinical setting as a noninvasive method to help quantify the retention and survival of transplanted GNT-labeled MSCs in the heart. Both T_1- and T_2- weighted imaging of the GNT-labeled MSCs should be performed, and long-term studies should be completed to assess MSC integration into cardiac tissue and functional improvement of the heart.

Another innovative study that can be explored using the magnetic properties of GNT-labeled MSCs is the magnetically-guided construction of three-dimensional cell constructs for tissue engineering. Magnetically guiding cell growth can lead to tubular construction for angiogenesis, 3D patches for cell implantation, and the formation of other complex structures for organ development.

References

1. Frimpong, R. A.; Hilt, J. Z. Magnetic Nanoparticles in Biomedicine: Synthesis, Functionalization and Applications. *Nanomedicine* **2010**, *5*, 1401–1414.

2. Emerich, D. F.; Halberstadt, C.; Thanos, C. Role of Nanobiotechnology in Cell-Based Nanomedicine: A Concise Review. *J. Biomed. Nanotechnol.* **2007**, *3*, 235–244.

3. Xie, J. Magnetic Nanoparticle-Based Theranostics. *Theranostics* **2012**, 122.

4. Tran, L. A.; Krishnamurthy, R.; Muthupillai, R.; Cabreira-Hansen, M. da G.; Willerson, J. T.; Perin, E. C.; Wilson, L. J. Gadonanotubes as Magnetic Nanolabels for Stem Cell Detection. *Biomaterials* **2010**, *31*, 9482–9491.

5. Pittenger, M. F.; Martin, B. J. Mesenchymal Stem Cells and Their Potential as Cardiac Therapeutics. *Circ. Res.* **2004**, *95*, 9–20.

6. Javazon, E. H.; Beggs, K. J.; Flake, A. W. Mesenchymal Stem Cells: Paradoxes of Passaging. *Exp. Hematol.* **2004**, *32*, 414–425.

7. Chamberlain, G.; Fox, J.; Ashton, B.; Middleton, J. Concise Review: Mesenchymal Stem Cells: Their Phenotype, Differentiation Capacity, Immunological Features, and Potential for Homing. *Stem Cells* **2007**, *25*, 2739–2749.

8. Aggarwal, S.; Pittenger, M. F. Human Mesenchymal Stem Cells Modulate Allogeneic Immune Cell Responses. *Blood* **2005**, *105*, 1815–1822.

9. Devine, S. M.; Bartholomew, A. M.; Mahmud, N.; Nelson, M.; Patil, S.; Hardy, W.; Sturgeon, C.; Hewett, T.; Chung, T.; Stock, W. *et al.* Mesenchymal Stem Cells Are Capable of Homing to the Bone Marrow of Non-human Primates Following Systemic Infusion. *Exp. Hematol.* **2001**, *29*, 244–255.

10. Kassem, M.; Kristiansen, M.; Abdallah, B. M. Mesenchymal Stem Cells: Cell Biology and Potential Use in Therapy. *Basic Clin. Pharmacol. Toxicol.* **2004**, *95*, 209–214.

11. Abdel-Latif, A.; Bolli, R.; Tleyjeh, I. M.; Montori, V. M.; Perin, E. C.; Hornung, C. A.; Zuba-Surma, E. K.; Al-Mallah, M.; Dawn, B. Adult Bone Marrow-Derived Cells for Cardiac Repair: A Systematic Review and Meta-analysis. *Arch. Intern. Med.* **2007**, *167*, 989–997.

12. Shake, J. G.; Gruber, P. J.; Baumgartner, W. A.; Senechal, G.; Meyers, J.; Redmond, J. M.; Pittenger, M. F.; Martin, B. J. Mesenchymal Stem Cell Implantation in a Swine Myocardial Infarct Model: Engraftment and Functional Effects. *Ann. Thorac. Surg.* **2002**, *73*, 1919–1926.

13. Freyman, T.; Polin, G.; Osman, H.; Crary, J.; Lu, M.; Cheng, L.; Palasis, M.; Wilensky, R. L. A Quantitative, Randomized Study Evaluating Three Methods of Mesenchymal Stem Cell Delivery Following Myocardial Infarction. *Eur. Heart J.* **2006**, *27*, 1114–1122.

14. Hou, D.; Youssef, E. A.-S.; Brinton, T. J.; Zhang, P.; Rogers, P.; Price, E. T.; Yeung, A. C.; Johnstone, B. H.; Yock, P. G.; March, K. L. Radiolabeled Cell

Distribution After Intramyocardial, Intracoronary, and Interstitial Retrograde Coronary Venous Delivery Implications for Current Clinical Trials. *Circulation* **2005**, *112*, I–150–I–156.

15. Perin, E. C.; Silva, G. V.; Assad, J. A. R.; Vela, D.; Buja, L. M.; Sousa, A. L. S.; Litovsky, S.; Lin, J.; Vaughn, W. K.; Coulter, S. *et al.* Comparison of Intracoronary and Transendocardial Delivery of Allogeneic Mesenchymal Cells in a Canine Model of Acute Myocardial Infarction. *J. Mol. Cell. Cardiol.* **2008**, *44*, 486–495.

16. Penn, M. S. *Stem Cells And Myocardial Regeneration*; Humana Press, 2007.

17. Wagner, J.; Kean, T.; Young, R.; Dennis, J. E.; Caplan, A. I. Optimizing Mesenchymal Stem Cell-based Therapeutics. *Curr. Opin. Biotechnol.* **2009**, *20*, 531–536.

18. Li, T.; Cheng, K.; Lee, S.; Matsushita, S.; Davis, D.; Malliaras, K.; Zhang, Y.; Matsushita, N.; Smith, R. R.; Marbán, E. Cardiospheres Recapitulate a Niche-Like Microenvironment Rich in Stemness and Cell-Matrix Interactions, Rationalizing Their Enhanced Functional Potency for Myocardial Repair. *Stem Cells* **2010**, *28*, 2088–2098.

19. Segers, V. F. M.; Lee, R. T. Stem-cell Therapy for Cardiac Disease. *Nature* **2008**, *451*, 937–942.

20. Ferreira, L.; Karp, J. M.; Nobre, L.; Langer, R. New Opportunities: The Use of Nanotechnologies to Manipulate and Track Stem Cells. *Cell Stem Cell* **2008**, *3*, 136–146.

21. Nguyen, P. K.; Lan, F.; Wang, Y.; Wu, J. C. Imaging Guiding the Clinical Translation of Cardiac Stem Cell Therapy. *Circ. Res.* **2011**, *109*, 962–979.

22. Nunn, A. D.; Linder, K. E.; Tweedle, M. F. Can Receptors Be Imaged with MRI Agents? *Q. J. Nucl. Med.* **1997**, *41*, 155–162.

23. Cheng, K.; Li, T.-S.; Malliaras, K.; Davis, D. R.; Zhang, Y.; Marbán, E. Magnetic Targeting Enhances Engraftment and Functional Benefit of Iron-Labeled Cardiosphere-Derived Cells in Myocardial Infarction. *Circ. Res.* **2010**, *106*, 1570–1581.

24. Cheng, K.; Malliaras, K.; Li, T.-S.; Sun, B.; Houde, C.; Galang, G.; Smith, J.; Matsushita, N.; Marbán, E. Magnetic Enhancement of Cell Retention, Engraftment and Functional Benefit After Intracoronary Delivery of Cardiac-derived Stem Cells in a Rat Model of Ischemia/reperfusion. *Cell Transplant.* **2012**, PMID: 22405128.

25. Hsiao, J.; Tai, M.; Chu, H.; Chen, S.; Li, H.; Lai, D.; Hsieh, S.; Wang, J.; Liu, H. Magnetic Nanoparticle Labeling of Mesenchymal Stem Cells Without Transfection Agent: Cellular Behavior and Capability of Detection with Clinical 1.5 T Magnetic Resonance at the Single Cell Level. *Magn. Reson. Med.* **2007**, *58*, 717–724.

26. Song, Y. S.; Ku, J. H. Monitoring Transplanted Human Mesenchymal Stem Cells in Rat and Rabbit Bladders Using Molecular Magnetic Resonance Imaging. *Neurourol. Urodyn.* **2007**, *26*, 584–593.

27. Arbab, A. S.; Yocum, G. T.; Bashaw Wilson, L.; Parwana, A.; Jordan, E. K.; Kalish, H.; Frank, J. A. Comparison of Transfection Agents in Forming Complexes with Ferumoxides, Cell Labeling Efficiency, and Cellular Viability. *Mol. Imaging* **2004**, *3*, 24–32.

28. Bulte, J. W. M.; Kraitchman, D. L. Iron Oxide MR Contrast Agents for Molecular and Cellular Imaging. *NMR Biomed.* **2004**, *17*, 484–499.

29. Hartman, K. B.; Wilson, L. J.; Rosenblum, M. G. Detecting and Treating Cancer with Nanotechnology. *Mol. Diagn. Ther.* **2008**, *12*, 1–14.

30. Yang, L.; Zhang, L.; Webster, T. J. Carbon Nanostructures for Orthopedic Medical Applications. *Nanomedicine* **2011**, *6*, 1231–1244.

31. Flahaut, E.; Durrieu, M.; Remy-Zolghadri, M.; Bareille, R.; Baquey, C. Study of the Cytotoxicity of CCVD Carbon Nanotubes. *J. Mater. Sci.* **2006**, *41*, 2411–2416.

32. Pantarotto, D.; Partidos, C. D.; Hoebeke, J.; Brown, F.; Kramer, E.; Briand, J.-P.; Muller, S.; Prato, M.; Bianco, A. Immunization with Peptide-Functionalized Carbon Nanotubes Enhances Virus-Specific Neutralizing Antibody Responses. *Chem. Biol.* **2003**, *10*, 961–966.

33. Tóth, É.; Bolskar, R. D.; Borel, A.; González, G.; Helm, L.; Merbach, A. E.; Sitharaman, B.; Wilson, L. J. Water-Soluble Gadofullerenes: Toward High-Relaxivity, pH-Responsive MRI Contrast Agents. *J. Am. Chem. Soc.* **2004**, *127*, 799–805.

34. Singh, R.; Pantarotto, D.; Lacerda, L.; Pastorin, G.; Klumpp, C.; Prato, M.; Bianco, A.; Kostarelos, K. Tissue Biodistribution and Blood Clearance Rates of Intravenously Administered Carbon Nanotube Radiotracers. *Proc. Natl. Acad. Sci.* **2006**, *103*, 3357–3362.

35. Sitharaman, B.; Tran, L. A.; Pham, Q. P.; Bolskar, R. D.; Muthupillai, R.; Flamm, S. D.; Mikos, A. G.; Wilson, L. J. Gadofullerenes as Nanoscale Magnetic Labels for Cellular MRI. *Contrast Media Mol. Imaging* **2007**, *2*, 139–146.

36. Shi Kam, N. W.; Jessop, T. C.; Wender, P. A.; Dai, H. Nanotube Molecular Transporters: Internalization of Carbon Nanotube−Protein Conjugates into Mammalian Cells. *J. Am. Chem. Soc.* **2004**, *126*, 6850–6851.

37. Hassan, A. A.; Chan, B. T.; Tran, L. A.; Hartman, K. B.; Ananta, J. S.; Mackeyev, Y.; Hu, L.; Pautler, R. G.; Wilson, L. J.; Lee, A. V. Serine-derivatized Gadonanotubes as Magnetic Nanoprobes for Intracellular Labeling. *Contrast Media Mol. Imaging* **2010**, *5*, 34–38.

38. Guven, A.; Rusakova, I. A.; Lewis, M. T.; Wilson, L. J. Cisplatin@US-tube Carbon Nanocapsules for Enhanced Chemotherapeutic Delivery. *Biomaterials* **2012**, *33*, 1455–1461.

39. Hartman, K. B.; Hamlin, D. K.; Wilbur, D. S.; Wilson, L. J. 211AtCl@US-Tube Nanocapsules: A New Concept in Radiotherapeutic-Agent Design. *Small* **2007**, *3*, 1496–1499.

40. Ashcroft, J. M.; Hartman, K. B.; Kissell, K. R.; Mackeyev, Y.; Pheasant, S.; Young, S.; Heide, P. a. W. Van der; Mikos, A. G.; Wilson, L. J. Single-Molecule I2@US-Tube Nanocapsules: A New X-ray Contrast-Agent Design. *Adv. Mater.* **2007**, *19*, 573–576.

41. Sitharaman, B.; Wilson, L. J. Gadofullerenes and Gadonanotubes: A New Paradigm for High-Performance Magnetic Resonance Imaging Contrast Agent Probes. *J. Biomed. Nanotechnol.* **2007**, *3*, 342–352.

42. Sitharaman, B.; Kissell, K. R.; Hartman, K. B.; Tran, L. A.; Baikalov, A.; Rusakova, I.; Sun, Y.; Khant, H. A.; Ludtke, S. J.; Chiu, W. *et al.* Superparamagnetic Gadonanotubes Are High-performance MRI Contrast Agents. *Chem. Commun.* **2005**, 3915–3917.

43. Raffa, V.; Ciofani, G.; Vittorio, O.; Riggio, C.; Cuschieri, A. Physicochemical Properties Affecting Cellular Uptake of Carbon Nanotubes. *Nanomedicine* **2010**, *5*, 89–97.

44. Tang, A. M.; Ananta, J. S.; Zhao, H.; Cisneros, B. T.; Lam, E. Y.; Wong, S. T.; Wilson, L. J.; Wong, K. K. Cellular Uptake and Imaging Studies of Gadolinium-loaded Single-walled Carbon Nanotubes as MRI Contrast Agents. *Contrast Media Mol. Imaging* **2011**, *6*, 93–99.

45. Hill, J. M.; Dick, A. J.; Raman, V. K.; Thompson, R. B.; Yu, Z.-X.; Hinds, K. A.; Pessanha, B. S. S.; Guttman, M. A.; Varney, T. R.; Martin, B. J. *et al.* Serial Cardiac Magnetic Resonance Imaging of Injected Mesenchymal Stem Cells. *Circulation* **2003**, *108*, 1009–1014.

46. Kraitchman, D.; Bulte, J. Imaging of Stem Cells Using MRI. *Basic Res. Cardiol.* **2008**, *103*, 105–113.

47. IMV: 2007 MRI Market Summary Report **2008**.

48. Brown, M. A.; Semelka, R. C. *MRI: Basic Principles and Applications*; John Wiley & Sons, 2010.

49. Caravan, P.; Ellison, J. J.; McMurry, T. J.; Lauffer, R. B. Gadolinium(III) Chelates as MRI Contrast Agents: Structure, Dynamics, and Applications. *Chem. Rev.* **1999**, *99*, 2293–2352.

50. Caravan, P. Physiochemical principles of MR contrast agents. In *Molecular and Cellular MR Imaging*; CRC Press: Boca Raton, 2007; pp. 13–36.

51. Gu, Z.; Peng, H.; Hauge, R. H.; Smalley, R. E.; Margrave, J. L. Cutting Single-Wall Carbon Nanotubes Through Fluorination. *Nano Lett.* **2002**, *2*, 1009–1013.

52. Ashcroft, J. M.; Hartman, K. B.; Mackeyev, Y.; Hofmann, C.; Pheasant, S.; Alemany, L. B.; Wilson, L. J. Functionalization of Individual Ultra-short Single-walled Carbon Nanotubes. *Nanotechnology* **2006**, *17*, 5033–5037.

53. Bosch, P.; Pratt, S. L.; Stice, S. L. Isolation, Characterization, Gene Modification, and Nuclear Reprogramming of Porcine Mesenchymal Stem Cells. *Biol. Reprod.* **2006**, *74*, 46–57.

54. Wiley, H. S.; Herbst, J. J.; Walsh, B. J.; Lauffenburger, D. A.; Rosenfeld, M. G.; Gill, G. N. The Role of Tyrosine Kinase Activity in Endocytosis, Compartmentation, and down-Regulation of the Epidermal Growth Factor Receptor. *J. Biol. Chem.* **1991**, *266*, 11083–11094.

55. Ito, A.; Hibino, E.; Honda, H.; Hata, K.; Kagami, H.; Ueda, M.; Kobayashi, T. A New Methodology of Mesenchymal Stem Cell Expansion Using Magnetic Nanoparticles. *Biochem. Eng. J.* **2004**, *20*, 119–125.

56. Jong, W. H. De; Borm, P. J. Drug Delivery and Nanoparticles: Applications and Hazards. *Int J Nanomedicine* **2008**, *3*, 133–149.

57. Mu, Q.; Broughton, D. L.; Yan, B. Endosomal Leakage and Nuclear Translocation of Multiwalled Carbon Nanotubes: Developing a Model for Cell Uptake. *Nano Lett.* **2009**, *9*, 4370–4375.

58. Kuchnir Fygenson, D.; Elbaum, M.; Shraiman, B.; Libchaber, A. Microtubules and Vesicles Under Controlled Tension. *Phys. Rev. E* **1997**, *55*, 850–859.

59. Bottini, M.; Bruckner, S.; Nika, K.; Bottini, N.; Bellucci, S.; Magrini, A.; Bergamaschi, A.; Mustelin, T. Multi-walled Carbon Nanotubes Induce T Lymphocyte Apoptosis. *Toxicol. Lett.* **2006**, *160*, 121–126.

60. Nimmagadda, A.; Thurston, K.; Nollert, M. U.; McFetridge, P. S. Chemical Modification of SWNT Alters in Vitro cell-SWNT Interactions. *Journal of Biomedical Materials Research Part A* **2006**, *76A*, 614–625.

61. Zhang, L. W.; Zeng, L.; Barron, A. R.; Monteiro-Riviere, N. A. Biological Interactions of Functionalized Single-Wall Carbon Nanotubes in Human Epidermal Keratinocytes. *Int. J. Toxicol.* **2007**, *26*, 103–113.

62. Liu, D.; Yi, C.; Zhang, D.; Zhang, J.; Yang, M. Inhibition of Proliferation and Differentiation of Mesenchymal Stem Cells by Carboxylated Carbon Nanotubes. *ACS Nano* **2010**, *4*, 2185–2195.

63. Cui, D.; Tian, F.; Ozkan, C. S.; Wang, M.; Gao, H. Effect of Single Wall Carbon Nanotubes on Human HEK293 Cells. *Toxicol. Lett.* **2005**, *155*, 73–85.

64. Kagan, V. E.; Tyurina, Y. Y.; Tyurin, V. A.; Konduru, N. V.; Potapovich, A. I.; Osipov, A. N.; Kisin, E. R.; Schwegler-Berry, D.; Mercer, R.; Castranova, V. *et al.* Direct and Indirect Effects of Single Walled Carbon Nanotubes on RAW 264.7 Macrophages: Role of Iron. *Toxicol. Lett.* **2006**, *165*, 88–100.

65. Shvedova, A.; Castranova, V.; Kisin, E.; Schwegler-Berry, D.; Murray, A.; Gandelsman, V.; Maynard, A.; Baron, P. Exposure to Carbon Nanotube Material: Assessment of Nanotube Cytotoxicity Using Human Keratinocyte Cells. *J. Toxicol. Environ. Health, Part A* **2003**, *66*, 1909–1926.

66. Schipper, M. L.; Nakayama-Ratchford, N.; Davis, C. R.; Kam, N. W. S.; Chu, P.; Liu, Z.; Sun, X.; Dai, H.; Gambhir, S. S. A Pilot Toxicology Study of Single-

walled Carbon Nanotubes in a Small Sample of Mice. *Nat. Nanotechnol.* **2008**, *3*, 216–221.

67. Garibaldi, S.; Brunelli, C.; Bavastrello, V.; Ghigliotti, G.; Nicolini, C. Carbon Nanotube Biocompatibility with Cardiac Muscle Cells. *Nanotechnology* **2006**, *17*, 391–397.

68. Kolosnjaj-Tabi, J.; Hartman, K. B.; Boudjemaa, S.; Ananta, J. S.; Morgant, G.; Szwarc, H.; Wilson, L. J.; Moussa, F. In Vivo Behavior of Large Doses of Ultrashort and Full-length Single-walled Carbon Nanotubes After Oral and Intraperitoneal Administration to Swiss Mice. *ACS Nano* **2010**, *4*, 1481–1492.

69. Fiorito, S.; Serafino, A.; Andreola, F.; Bernier, P. Effects of Fullerenes and Single-wall Carbon Nanotubes on Murine and Human Macrophages. *Carbon* **2006**, *44*, 1100–1105.

70. Griffiths, B. Scaling-up of animal cell cultures. In *Animal cell culture: a practical approach*; Oxford University Press: Oxford, 2000; pp. 19–68.

71. Tushar, V. G.; Tibshirani, R.; Chu, G. Significance Analysis of Microarrays Applied to the Ionizing Radiation Response. *Proc. Natl. Acad. Sci.* **2001**, *98*, 5116–5121.

72. Tsai, S.; Cassady, J. P.; Freking, B. A.; Nonneman, D. J.; Rohrer, G. A.; Piedrahita, J. A. Annotation of the Affymetrix1 Porcine Genome Microarray. *Anim. Genet.* **2006**, *37*, 423–424.

73. Leiss, M.; Beckmann, K.; Girós, A.; Costell, M.; Fässler, R. The Role of Integrin Binding Sites in Fibronectin Matrix Assembly in Vivo. *Curr. Opin. Cell Biol.* **2008**, *20*, 502–507.

74. Heino, J. The Collagen Family Members as Cell Adhesion Proteins. *BioEssays* **2007**, *29*, 1001–1010.

75. Liu, V. A.; Jastromb, W. E.; Bhatia, S. N. Engineering Protein and Cell Adhesivity Using PEO-terminated Triblock Polymers. *J. Biomed. Mater. Res.* **2002**, *60*, 126–134.

76. Corey, J. M.; Gertz, C. C.; Sutton, T. J.; Chen, Q.; Mycek, K. B.; Wang, B.; Martin, A. A.; Johnson, S. L.; Feldman, E. L. Patterning N-type and S-type Neuroblastoma Cells with Pluronic F108 and ECM Proteins. *J. Biomed. Mater. Res., Part A* **2010**, *93A*, 673–686.

77. Kültz, D. Molecular and Evolutionary Basis of the Cellular Stress Response. *Annu. Rev. Physiol.* **2005**, *67*, 225–257.

78. Chavakis, E.; Koyanagi, M.; Dimmeler, S. Enhancing the Outcome of Cell Therapy for Cardiac Repair Progress From Bench to Bedside and Back. *Circulation* **2010**, *121*, 325–335.

79. Al Kindi, A.; Ge, Y.; Shum-Tim, D.; Chiu, R. C.-J. Cellular Cardiomyoplasty: Routes of Cell Delivery and Retention. *Front. Biosci.* **2008**, *13*, 2421–2434.

80. Martens, T. P.; Godier, A. F. G.; Parks, J. J.; Wan, L. Q.; Koeckert, M. S.; Eng, G. M.; Hudson, B. I.; Sherman, W.; Vunjak-Novakovic, G. Percutaneous Cell Delivery Into the Heart Using Hydrogels Polymerizing In Situ. *Cell Transplant.* **2009**, *18*, 297–304.

81. Consigny, P. M.; Silverberg, D. A.; Vitali, N. J. Use of Endothelial Cells Containing Superparamagnetic Microspheres to Improve Endothelial Cell Delivery to Arterial Surfaces After Angioplasty. *J. Vasc. Intervent. Radiol.* **1999**, *10*, 155–163.

82. Woodside, D. G.; Kram, R. M.; Mitchell, J. S.; Belsom, T.; Billard, M. J.; McIntyre, B. W.; Vanderslice, P. Contrasting Roles for Domain 4 of VCAM-1 in the Regulation of Cell Adhesion and Soluble VCAM-1 Binding to Integrin A4β1. *J. Immunol.* **2006**, *176*, 5041–5049.

83. Wang, D. M.; Tarbell, J. M. Modeling Interstitial Flow in an Artery Wall Allows Estimation of Wall Shear Stress on Smooth Muscle Cells. *J. Biomech. Eng.* **1995**, *117*, 358–363.

84. Hamamoto, H.; Gorman, J. H.; Ryan, L. P.; Hinmon, R.; Martens, T. P.; Schuster, M. D.; Plappert, T.; Kiupel, M.; St. John-Sutton, M. G.; Itescu, S. *et al.* Allogeneic Mesenchymal Precursor Cell Therapy to Limit Remodeling After Myocardial Infarction: The Effect of Cell Dosage. *Ann. Thorac. Surg.* **2009**, *87*, 794–801.

85. Perin, E. C.; Dohmann, H. F. R.; Borojevic, R.; Silva, S. A.; Sousa, A. L. S.; Mesquita, C. T.; Rossi, M. I. D.; Carvalho, A. C.; Dutra, H. S.; Dohmann, H. J. F. *et al.* Transendocardial, Autologous Bone Marrow Cell Transplantation for Severe, Chronic Ischemic Heart Failure. *Circulation* **2003**, *107*, 2294–2302.

86. Kim, J. A.; Åberg, C.; Salvati, A.; Dawson, K. A. Role of Cell Cycle on the Cellular Uptake and Dilution of Nanoparticles in a Cell Population. *Nat. Nanotechnol.* **2012**, *7*, 62–68.

87. Ananta, J. S.; Matson, M. L.; Tang, A. M.; Mandal, T.; Lin, S.; Wong, K.; Wong, S. T.; Wilson, L. J. Single-Walled Carbon Nanotube Materials as T2-Weighted MRI Contrast Agents. *J. Phys. Chem. C* **2009**, *113*, 19369–19372.

88. Reed, J. C.; Bischoff, J. R. BIRinging Chromosomes Through Cell Division—And Survivin' the Experience. *Cell* **2000**, *102*, 545–548.

89. Chan, Y. W.; Fava, L. L.; Uldschmid, A.; Schmitz, M. H. A.; Gerlich, D. W.; Nigg, E. A.; Santamaria, A. Mitotic Control of Kinetochore-Associated Dynein and Spindle Orientation by Human Spindly. *J. Cell. Biol.* **2009**, *185*, 859–874.

90. Shaikh, T. H.; Gottlieb, S.; Sellinger, B.; Chen, F.; Roe, B. A.; Oakey, R. J.; Emanuel, B. S.; Budarf, M. L. Characterization of <i>CDC45L:</i> a Gene in the 22q11.2 Deletion Region Expressed During Murine and Human Development. *Mamm. Genome* **1999**, *10*, 322–326.

91. Ayad, N. G.; Rankin, S.; Murakami, M.; Jebanathirajah, J.; Gygi, S.; Kirschner, M. W. Tome-1, a Trigger of Mitotic Entry, Is Degraded During G1 via the APC. *Cell* **2003**, *113*, 101–113.

92. Kaufman, P. D.; Kobayashi, R.; Kessler, N.; Stillman, B. The P150 and P60 Subunits of Chromatin Assemblyfactor I: A Molecular Link Between Newly Synthesized Histories and DNA Replication. *Cell* **1995**, *81*, 1105–1114.

93. Martinsson-Ahlzén, H.-S.; Liberal, V.; Grünenfelder, B.; Chaves, S. R.; Spruck, C. H.; Reed, S. I. Cyclin-Dependent Kinase-Associated Proteins Cks1 and Cks2 Are Essential During Early Embryogenesis and for Cell Cycle Progression in Somatic Cells. *Mol. Cell. Biol.* **2008**, *28*, 5698–5709.

94. Ono, T.; Losada, A.; Hirano, M.; Myers, M. P.; Neuwald, A. F.; Hirano, T. Differential Contributions of Condensin I and Condensin II to Mitotic Chromosome Architecture in Vertebrate Cells. *Cell* **2003**, *115*, 109–121.

95. Gong, D.; Ferrell, J. E. The Roles of Cyclin A2, B1, and B2 in Early and Late Mitotic Events. *Mol. Biol. Cell* **2010**, *21*, 3149–3161.

96. Chittka, A.; Arevalo, J. C.; Rodriguez-Guzman, M.; Pérez, P.; Chao, M. V.; Sendtner, M. The p75NTR-Interacting Protein SC1 Inhibits Cell Cycle Progression by Transcriptional Repression of Cyclin E. *J. Cell. Biol.* **2004**, *164*, 985–996.

97. Kaelin, W. G.; Krek, W.; Sellers, W. R.; DeCaprio, J. A.; Ajchenbaum, F.; Fuchs, C. S.; Chittenden, T.; Li, Y.; Farnham, P. J.; Blanar, M. A. *et al.* Expression

Cloning of a cDNA Encoding a Retinoblastoma-binding Protein with E2F-like Properties. *Cell* **1992**, *70*, 351–364.

98. Chiaur, D. S.; Murthy, S.; Cenciarelli, C.; Parks, W.; Loda, M.; Inghirami, G.; Demetrick, D.; Pagano, M. Five Human Genes Encoding F-box Proteins: Chromosome Mapping and Analysis in Human Tumors. *Cytogen. Genome Res.* **2000**, *88*, 255–258.

99. Saharia, A.; Teasley, D. C.; Duxin, J. P.; Dao, B.; Chiappinelli, K. B.; Stewart, S. A. FEN1 Ensures Telomere Stability by Facilitating Replication Fork Re-Initiation. *J. Biol. Chem.* **2010**, *285*, 27057–27066.

100. Labib, K.; Gambus, A. A Key Role for the GINS Complex at DNA Replication Forks. *Trends Cell Biol.* **2007**, *17*, 271–278.

101. Goto, H.; Kiyono, T.; Tomono, Y.; Kawajiri, A.; Urano, T.; Furukawa, K.; Nigg, E. A.; Inagaki, M. Complex Formation of Plk1 and INCENP Required for Metaphase-anaphase Transition. *Nat. Cell Biol.* **2005**, *8*, 180–187.

102. Nislow, C.; Lombillo, V. A.; Kuriyama, R.; Mclntosh, J. R. A Plus-end-directed Motor Enzyme That Moves Antiparallel Microtubules in Vitro Localizes to the Interzone of Mitotic Spindles. *Nature* **1992**, *359*, 543–547.

103. Kearsey, S. E.; Maiorano, D.; Holmes, E. C.; Todorov, I. T. The Role of MCM Proteins in the Cell Cycle Control of Genome Duplication. *BioEssays* **2005**, *18*, 183–190.

104. Fujita, Y.; Hayashi, T.; Kiyomitsu, T.; Toyoda, Y.; Kokubu, A.; Obuse, C.; Yanagida, M. Priming of Centromere for CENP-A Recruitment by Human hMis18α, hMis18β, and M18BP1. *Dev. Cell* **2007**, *12*, 17–30.

105. Hübscher, U.; Maga, G. DNA Replication and Repair Bypass Machines. *Curr. Opin. Chem. Biol.* **2011**, *15*, 627–635.

106. Cárcer, G. de; Manning, G.; Malumbres, M. From Plk1 to Plk5: Functional Evolution of Polo-like Kinases. *Cell Cycle* **2011**, *10*, 2255–2262.

107. Roostalu, J.; Schiebel, E.; Khmelinskii, A. Cell cycle control of spindle elongation. *Cell Cycle 9*, 1084–1090.

108. Zhao, W.-M.; Coppinger, J. A.; Seki, A.; Cheng, X.-L.; Yates, J. R.; Fang, G. RCS1, a Substrate of APC/C, Controls the Metaphase to Anaphase Transition. *Proc. Natl. Acad. Sci.* **2008**, *105*, 13415–13420.

109. Hanisch, A.; Silljé, H. H.; Nigg, E. A. Timely Anaphase Onset Requires a Novel Spindle and Kinetochore Complex Comprising Ska1 and Ska2. *EMBO J.* **2006**, *25*, 5504–5515.

110. Arachchige Don, A. S.; Dallapiazza, R. F.; Bennin, D. A.; Brake, T.; Cowan, C. E.; Horne, M. C. Cyclin G2 Is a Centrosome-associated Nucleocytoplasmic Shuttling Protein That Influences Microtubule Stability and Induces a P53-dependent Cell Cycle Arrest. *Exp. Cell Res.* **2006**, *312*, 4181–4204.

Appendix A

Figure A1. Light microscopy images of GNT-labeled MSCs at each step of the cell cleaning protocol. Scale bar = 50 µm.

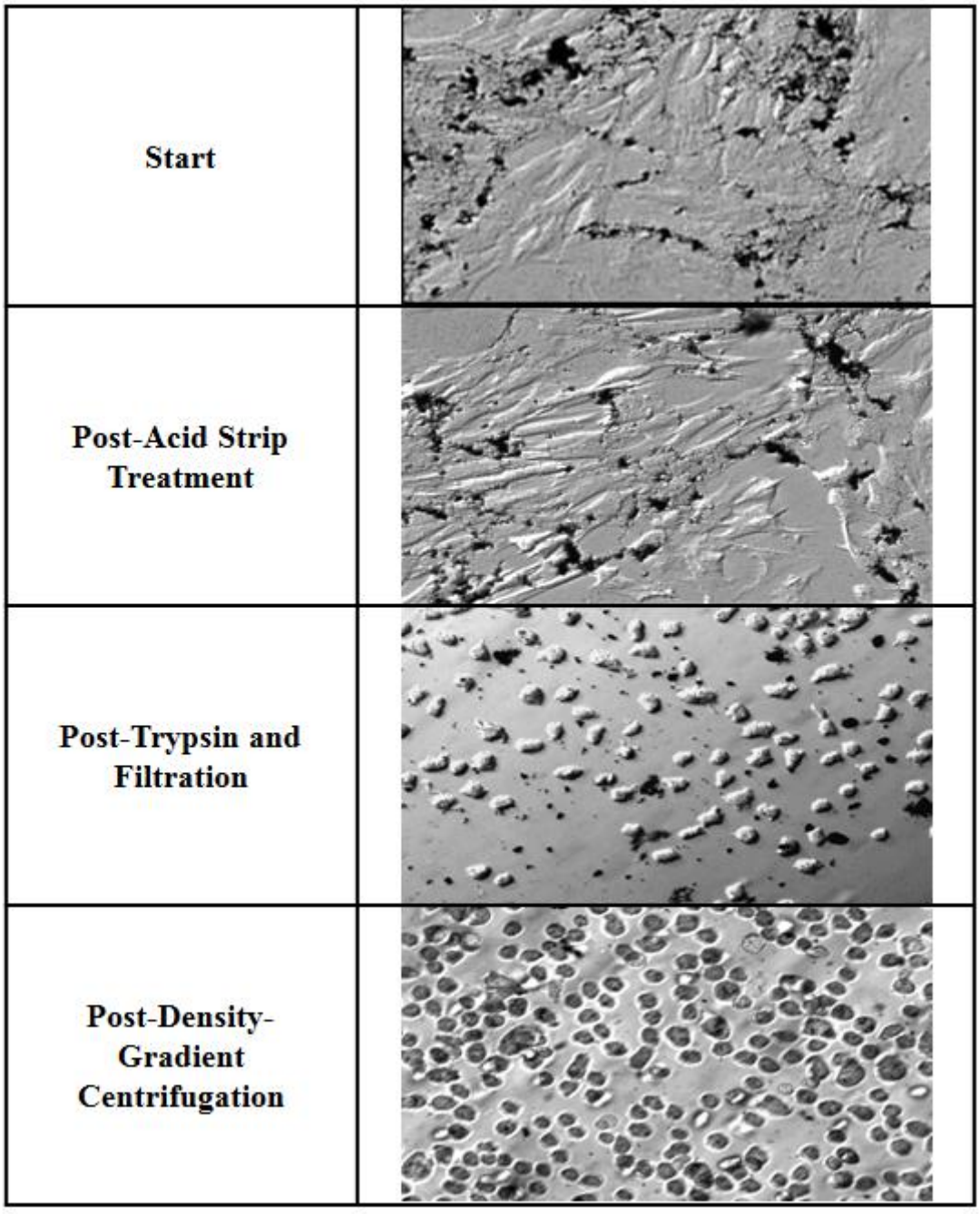

Figure A2. Cell viability analysis performed on GNT-labeled MSCs using a LIVE/DEAD viability/toxicity assay kit. Fluorescence-activated cell sorting (8580 gated events) was used to measure the fluorescence intensities for calcein AM (Calc, detection of live cells) and ethidium homodimer-1 (EthD, detection of dead cells).

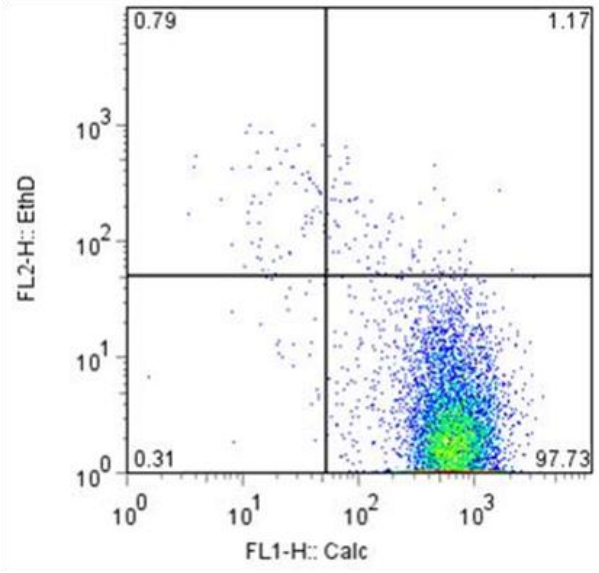

Appendix B

Heat maps containing the 123 differentially expressed transcripts analyzed from the transcriptome analysis of GNT-labeled MSCs (columns 1-3) and unlabeled MSCs (columns 4-6). Note: some transcripts may be duplicated/triplicated in the maps.

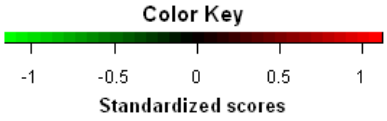

Heat Map	Symbol	Ratio	Gene Name	RefSeq Transcript ID (or UniGene ID)
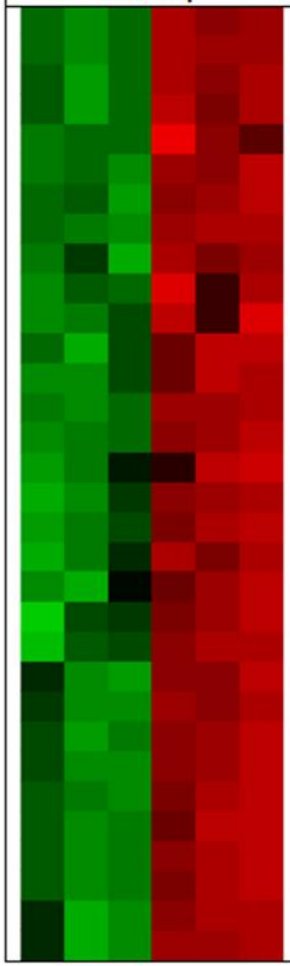	SKA2	-3.2	Spindle and kinetochore-associated protein 2	XM_003131674
	TCF19	-3.9	Transcription factor 19	NM_001167591
	-	-3.1	6mm ovarian follicle p6mm	1815673
	FABP5	-2.8	Fatty acid-binding protein 5	NM_001039746
	ALKBH8	-3.2	alkB, alkylation repair homolog 8	BI404620
	LMNB2	-2.6	Lamin B2	CF788083
	FEN1	-3.2	Flap structure-specific endonuclease 1	XM_003122631; XM_003122632
	LRRC59	-3.4	Leucine-rich repeat-containing protein 59	XM_003131579
	RNF123	-3.2	Ring finger protein 123	1248306
	LRRC17	-3.9	Leucine-rich repeat-containing protein 17	XM_003130237
	FABP3	-4.5	Fatty acid-binding protein 3, heart	NM_001099931
	ATAD2	-3.2	ATPase family AAA domain-containing protein 2	XM_001926030
	ID1	-4.5	DNA-binding protein inhibitor ID-1	XM_003134377
	SKA2	-2.9	Spindle and kinetochore-associated protein 2	XM_003131674
	GINS1	-4.0	DNA replication complex GINS protein PSF1	XM_003134310
	PCNA	-5.1	PCNA-associated factor	XM_003121460
	TMPO	-3.2	Thymopoietin	XM_003126696
	FBXO5	-4.1	F-box protein 5	XM_003121138
	CCDC115	-3.5	Coiled-coil domain-containing protein 115	XM_003133304
	LMNB1	-3.9	Lamin B1	XM_003123882
	WDHD1	-2.8	WD repeat and HMG-box DNA binding protein 1	XM_001924194
	RTN4IP1	-3.0	Reticulon 4 interacting protein 1	XM_003121325
	PCNA	-2.8	Proliferating cell nuclear antigen	692192
	FANCM	-3.0	Fanconi anemia group M protein	XM_003121784
	MCM2	-3.1	Minichromosome maintenance complex component 2	442082
	MCM4	-3.3	Minichromosome maintenance complex component 4	XM_001924933
	LYAR	-2.6	Ly1 antibody reactive homolog	XM_003128852
	NPM3	-3.4	Nucleoplasmin 3	XM_001928081
	CEP57L1	-2.5	Centrosomal protein 57kDa-like 1	XM_003121344; XM_003121345
	GALE	-2.9	UDP-glucose 4-epimerase	446677
	NES	-3.0	Nestin	XM_001925549
	E2F1	-4.2	Transcription factor E2F1	XM_001926880

Heat Map	Symbol	Ratio	Gene Name	RefSeq Transcript ID (or Public/UGID)
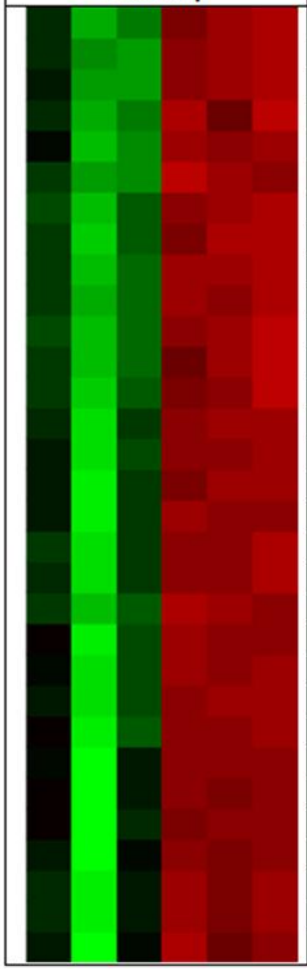	CHAF1B	-3.7	Chromatin assembly factor 1 subunit B (p60)	XM_003132765
	CDC45L	-2.8	Cell division cycle 45 homolog	XM_001929624
	CHAF1A	-3.0	Chromatin assembly factor 1 subunit A	XM_003123068
	HSD17B1	-2.8	Hydroxysteroid (17-beta) dehydrogenase 1	CK467445
	UBE2T	-2.9	Ubiquitin-conjugating enzyme E2 T-like	XM_003130609
	UBE2T	-2.7	Ubiquitin-conjugating enzyme E2 T-like	XM_003130609
	DZIP1	-3.6	DAZ interacting protein 1	CK457970
	CCDC99	-4.3	Coiled-coil domain containing 99	XM_003134063
	INCENP	-2.9	Inner centromere protein antigens 135/155kDa	XM_003122624
	CDK19	-3.0	cyclin-dependent kinase 19	XM_003133456
	VRK1	-3.7	Vaccinia related kinase 1	XM_001927381
	CDCA7	-3.4	Cell division cycle associated protein 7	XM_001928628; XM_001928632
	RRM2	-4.4	Ribonucleotide reductase M2	447233
	CEP55	-3.6	Centrosomal protein 55kDa	BX673528
	CKS2	-3.8	Cyclin-dependent kinases regulatory subunit 2	XM_003132790
	SKA1	-3.1	Spindle and KT-associated 1	XM_001926548; XM_003121438
	CDCA3	-4.1	Cell division cycle associated 3	XM_001928347
	RYR2	-3.0	Ryanodine receptor 2	CN153597
	ACE	-3.3	Angiotensin I converting enzyme	CK459351
	PLK4	-3.2	Polo-like kinase 4	XM_003129200; XM_003129201
	PRC1	-3.3	Protein regulator of cytokinesis 1	443312
	MIS18A	-3.4	Protein Mis18-alpha	443498
	UBE2T	-3.1	998175 MARC 4PIG	CN166510
	ARHGAP11A	-3.5	Rho GTPase-activating protein 11A	XM_001924579
	KIF23	-3.4	Kinesin family member 23	XM_003121763
	CCNB1	-3.7	Cyclin B1	NM_001170768
	NCAPG	-3.5	Non-SMC condensin I complex, subunit G	XM_003128870
	TOPOII	-3.6	Topoisomerase II	NM_213884
	BIRC5	-3.1	Baculoviral IAP repeat-containing protein 5	NM_214141
	CCNB2	-3.1	Cyclin B2	NM_001114282
	FAM64A	-3.3	Protein FAM64A	XM_003131878; XM_003131879

Heat Map	Symbol	Ratio	Gene Name	RefSeq Transcript ID (or UniGene ID)
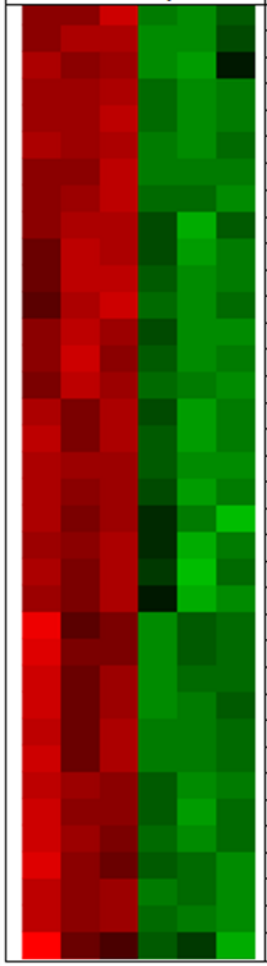	CTSL1	2.8	Cathepsin L1	XM_003130633
	LIF	3.9	Leukemia inhibitory factor	NM_214402
	AKR1C4/L1	2.7	Aldo-keto reductase family 1, member C4/C1	NM_001038626; NM_001123075
	AKAP12	2.5	A-kinase (PRKA) anchor protein 12	XM_001927265
	NDRG1	2.5	N-myc downstream regulated 1	XR_115857
	DDIT4	3.4	DNA damage-inducible transcript 4 protein	XM_001925275; XM_003133067
	HIP1R	2.6	Huntingtin interacting protein 1	XM_001925823
	ZC3H12A	3.2	Zinc finger CCCH-type containing 12A	CN165788
	SLC16A3	2.7	Solute carrier family 16, member 3	1044141
	SLC2A14	4.5	solute carrier family 2 (facilitated glucose transporter), member 14	CN156808
	NFKBIA	3.5	Nuclear factor klight polypeptide gene enhancer B-cells inhibitor α	NM_001005150
	SOD2	4.1	Superoxide dismutase 2	XM_001926440
	ASGR2	2.9	Asialoglycoprotein receptor 2-like	3011673
	BNIP3	3.1	BCL2/adenovirus E1B 19-kDa protein-interacting protein 3	455407
	ADM	3.8	Adrenomedullin	NM_214107
	DGKG	2.9	Diacylglycerol kinase, gamma 90kDa	CF788062
	C5orf41	3.0	UPF0474 protein	663328
	SAT1	2.6	Spermidine/spermine N1-acetyltransferase 1	NM_214358
	CCNG2	3.4	Cyclin G2	XM_003129099; XM_003129100
	HIST2H2BE	3.1	Histone H2B type 2-E	XM_003125782; XM_003125783
	TLR2	3.5	Toll-like receptor 2	NM_213761
	FBXO32	3.9	F-box only protein 32	NM_001044588
	PIK3IP1	3.0	Phosphoinositide-3-kinase interacting protein 1	XM_001926534
	ABCB1	3.1	ATP-binding cassette, sub-family B (MDR/TAP), member 1	XM_003130214
	RHOBTB2	3.0	Rho-related BTB domain containing 2	BM190251
	IRS2	3.7	Insulin receptor substrate 2	XR_116171
	IRS2	3.9	Insulin receptor substrate 2	XR_116171
	NFE2L1	2.7	Nuclear factor (erythroid-derived 2)-like 1	BP433515
	DAO	2.7	D-amino-acid oxidase	BF702982
	GABARAPL1	2.7	GABA(A) receptor-associated protein like 1	NM_001190287
	CABC1	3.2	Chaperone-activity of bc1 complex	XM_003130550
	DDIT3	2.5	DNA-damage inducible transcript 3	NM_001144845
	TP53INP1	2.6	Tumor protein p53 inducible nuclear protein 1	BI118962
	AUH	2.4	AU RNA binding protein/enoyl-CoA hydratase	XM_001928792
	C7orf41	3.2	Chromosome 7 open reading frame 41 ortholog	XM_003134811
	CYP2C19	3.3	Cytochrome P450 2C19	448334

Heat Map	Symbol	Ratio	Gene Name	RefSeq Transcript ID (or UniGene ID)
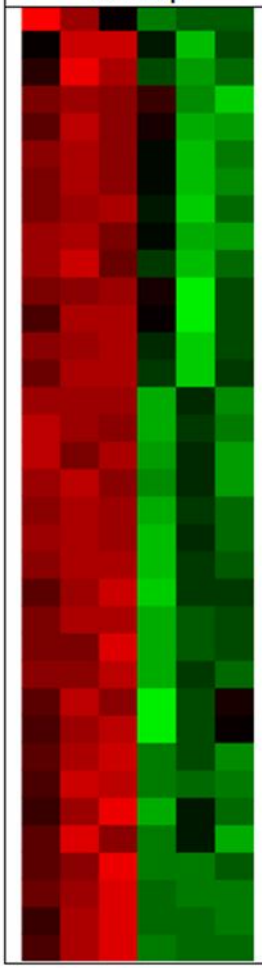	AKR1C4	3.8	Aldo-keto reductase family 1, member C4	NM_001038626; NM_001123075
	CASC1	3.3	Cancer susceptibility candidate 1	CO950175
	IL6	4.7	Interleukin-6	NM_214399
	MGP	4.2	Matrix Gla-protein	NM_214116
	RNASE4	4.6	Ribonuclease 4	NM_213936
	EPHX1	3.2	Epoxide hydrolase 1	NM_214355
	ARRDC4	3.6	Arrestin domain containing 4	CB475105
	CEBPdelta	3.2	CCAAT/enhancer-binding protein delta	XM_001925928
	CD9	3.1	CD9 antigen	NM_214006
	SCARA5	2.9	Scavenger receptor class A, member 5	BX916176
	TXNIP	5.2	Thioredoxin interacting protein	NM_001044614
	VCAM1	5.6	Vascular cell adhesion molecule 1	NM_213891
	CEBPdelta	2.9	CCAAT/enhancer binding protein delta	XM_001925928
	CCL2	3.1	C-C motif chemokine 2	NM_214214
	MAFF	3.7	v-maf musculoaponeurotic fibrosarcoma oncogene homolog F	BQ600866
	TGH2	4.7	Tissue transglutaminase homologue	XM_001925640
	MT1A	3.8	Metallothionein 1A	NM_001001266
	C8orf4	3.6	chromosome 8 open reading frame 4	BQ604560
	IEX1/IER3	3.1	Radiation-inducible immediate-early gene IEX-1	XM_001924516
	HTRA4	3.5	HtrA serine peptidase 4	CK450639
	CXCL2	5.3	C-X-C motif chemokine 2	NM_001001861
	CXCL2	4.8	C-X-C motif chemokine 2	XM_003129107
	ANGPTL4	4.3	Angiopoietin-related protein 4	NM_001038644
	LRP11	2.7	Low density lipoprotein receptor-related protein 11	BQ601688
	CXCL2	4.7	C-X-C motif chemokine 2	XM_003126160
	CXCL6	3.5	Chemokine (C-X-C motif) ligand 6	NM_213876
	CXCL6	3.7	Chemokine (C-X-C motif) ligand 6	NM_213876
	RNF144B	4.0	Ring finger protein 144B	BF710766
	NUPR1	4.4	Nuclear protein 1 isoform b	3008543
	CLDN1	3.9	Claudin 1	BQ604567
	PTGS2	3.9	Prostaglandin G/H synthase 2	NM_214321
	MASP1	2.8	Mannan-binding lectin serine peptidase 1	CN154795
	SDC4	2.9	Syndecan 4	XR_116382
	SOD2	3.9	Superoxide dismutase [Mn]	XM_001926440
	SOD2	3.9	Superoxide dismutase [Mn]	XM_001926440

Appendix C

Cell cycle (6) and immune response pathway analysis (6) maps affected by GNT incorporation into MSCs.

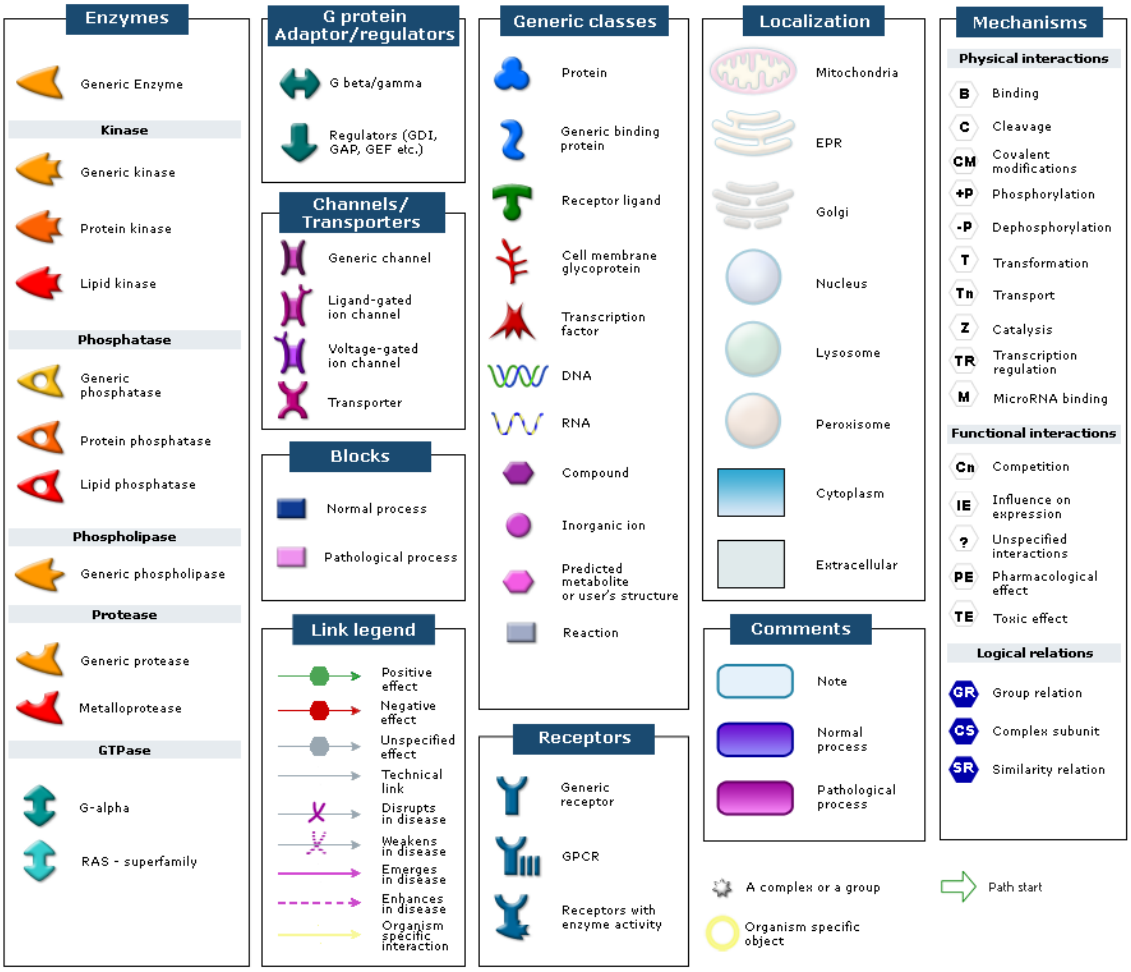

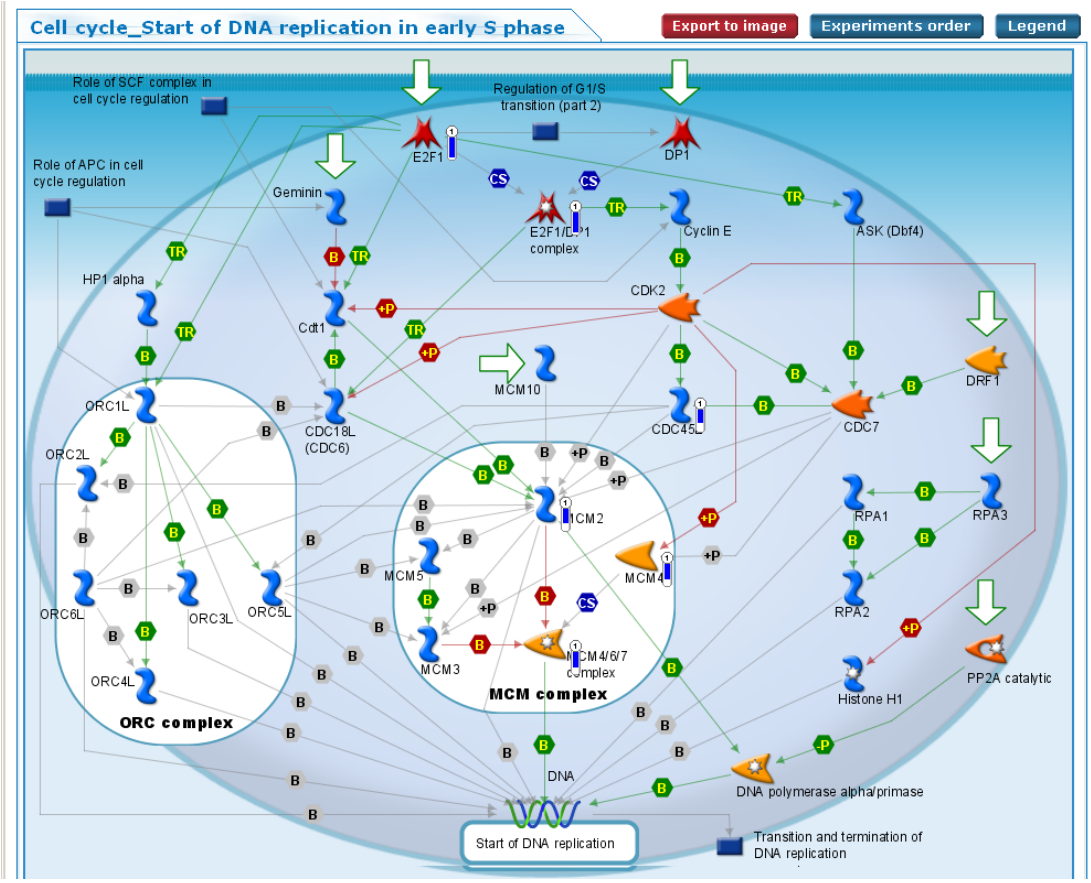
Cell cycle_Start of DNA replication in early S phase
Export to image
Experiments order
Legend
Role of SCF complex in cell cycle regulation
Regulation of G1/S transition (part 2)
Role of APC in cell cycle regulation
E2F1
DP1
Geminin
E2F1/DP1 complex
Cyclin E
ASK (Dbf4)
HP1 alpha
CDK2
Cdt1
MCM10
DRF1
ORC1L
CDC18L (CDC6)
CDC45L
CDC7
ORC2L
MCM2
RPA1
RPA3
MCM5
MCM4
ORC6L
ORC3L
ORC5L
RPA2
MCM4/6/7 complex
MCM3
PP2A catalytic
ORC4L
MCM complex
Histone H1
ORC complex
DNA
DNA polymerase alpha/primase
Start of DNA replication
Transition and termination of DNA replication

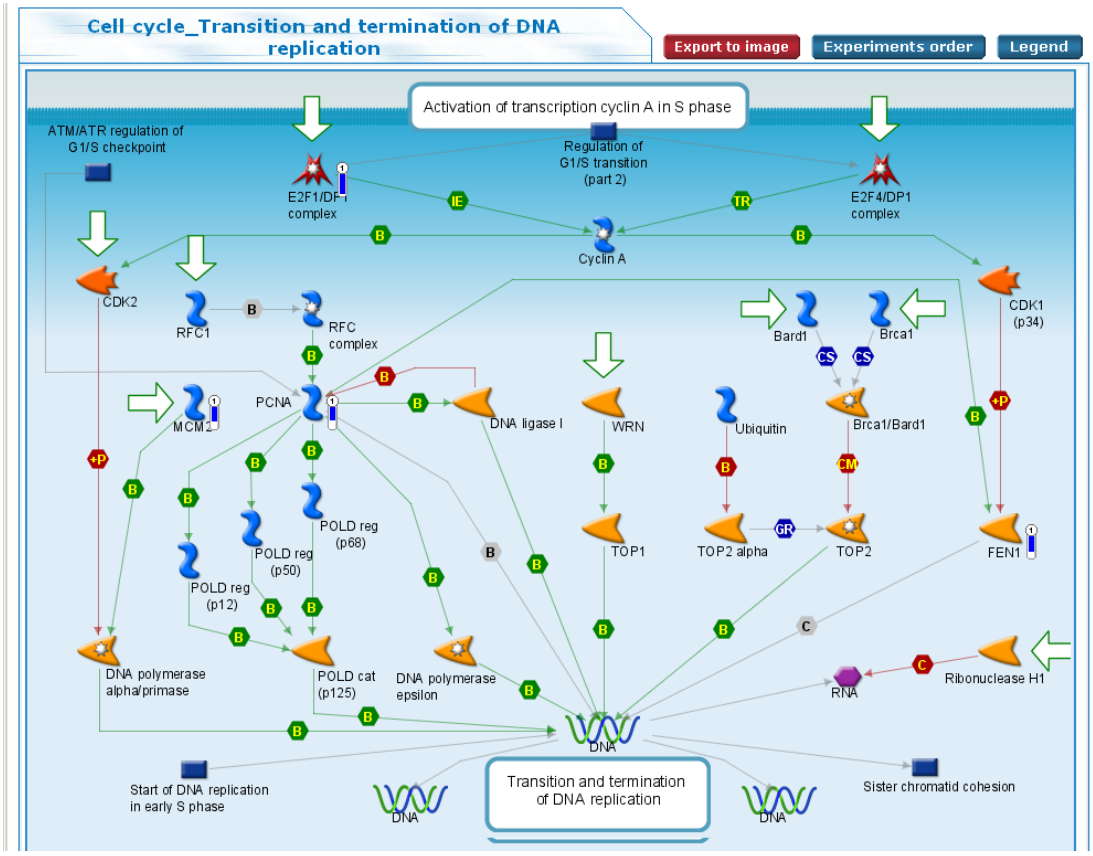
Cell cycle_Transition and termination of DNA replication
Export to image
Experiments order
Legend
Activation of transcription cyclin A in S phase
ATM/ATR regulation of G1/S checkpoint
Regulation of G1/S transition (part 2)
E2F1/DP1 complex
E2F4/DP1 complex
Cyclin A
CDK2
RFC1
RFC complex
CDK1 (p34)
Bard1
Brca1
PCNA
MCM2
DNA ligase I
WRN
Ubiquitin
Brca1/Bard1
POLD reg (p68)
POLD reg (p50)
POLD reg (p12)
TOP1
TOP2 alpha
TOP2
FEN1
DNA polymerase alpha/primase
POLD cat (p125)
DNA polymerase epsilon
RNA
Ribonuclease H1
DNA
Start of DNA replication in early S phase
Transition and termination of DNA replication
Sister chromatid cohesion

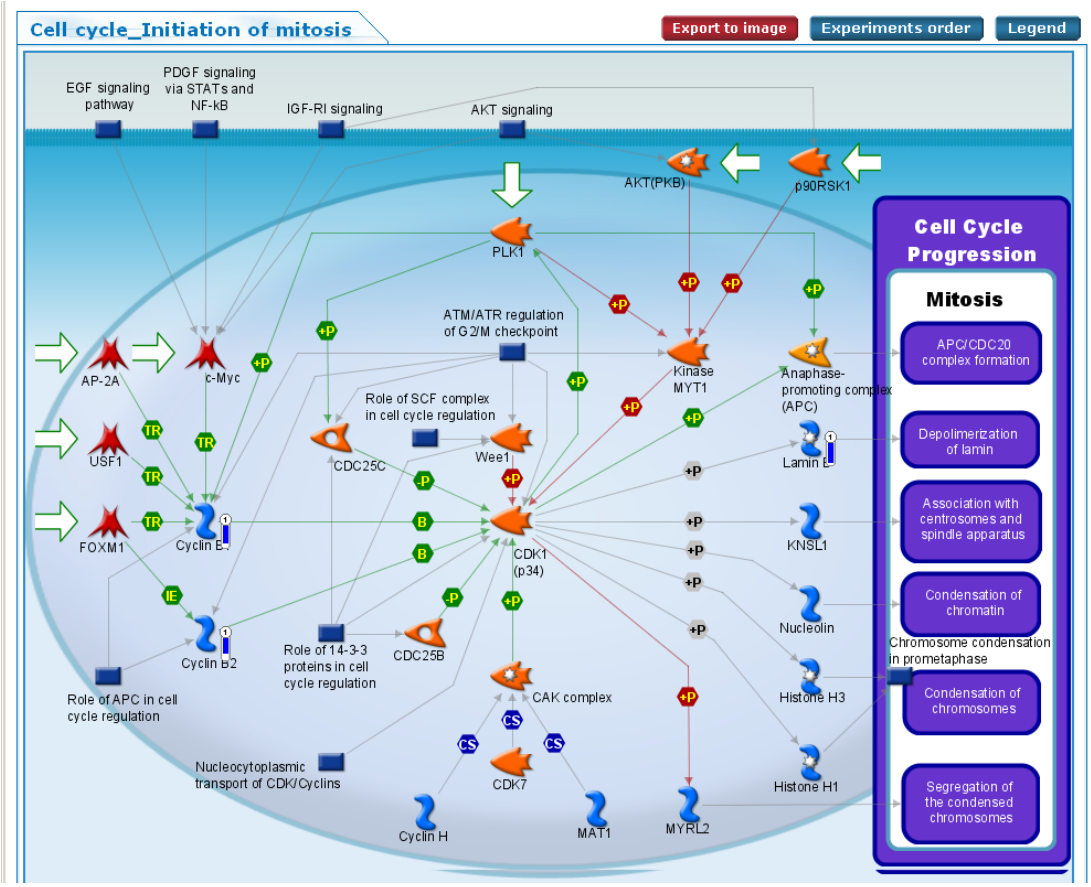
Cell cycle_Initiation of mitosis
Export to image
Experiments order
Legend
EGF signaling pathway
PDGF signaling via STATs and NF-kB
IGF-RI signaling
AKT signaling
AKT(PKB)
p90RSK1
PLK1
ATM/ATR regulation of G2/M checkpoint
Kinase MYT1
Anaphase-promoting complex (APC)
AP-2A
c-Myc
USF1
FOXM1
Cyclin E
Role of SCF complex in cell cycle regulation
CDC25C
Wee1
CDK1 (p34)
Lamin B
KNSL1
Nucleolin
Histone H3
Histone H1
Cyclin B2
Role of 14-3-3 proteins in cell cycle regulation
CDC25B
CAK complex
CDK7
Cyclin H
MAT1
MYRL2
Role of APC in cell cycle regulation
Nucleocytoplasmic transport of CDK/Cyclins
Cell Cycle Progression
Mitosis
APC/CDC20 complex formation
Depolimerization of lamin
Association with centrosomes and spindle apparatus
Condensation of chromatin
Chromosome condensation in prometaphase
Condensation of chromosomes
Segregation of the condensed chromosomes

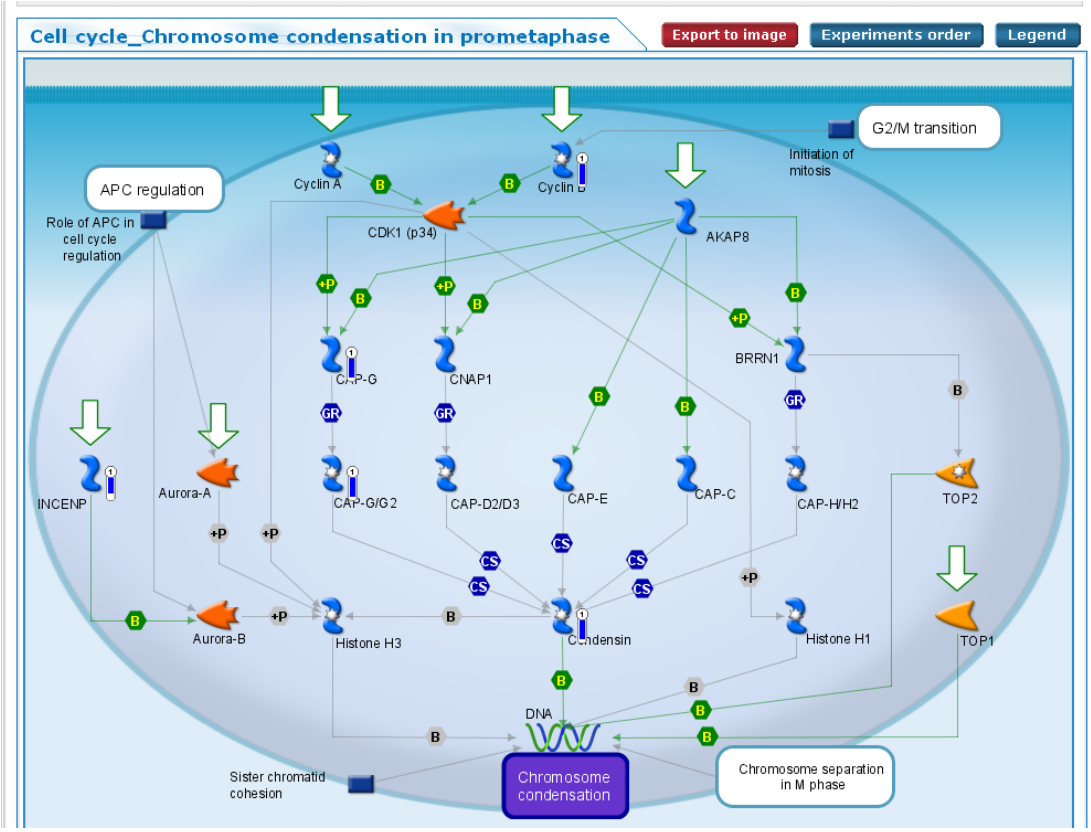
Cell cycle_Chromosome condensation in prometaphase
Export to image
Experiments order
Legend
G2/M transition
Initiation of mitosis
APC regulation
Role of APC in cell cycle regulation
Cyclin A
Cyclin B
CDK1 (p34)
AKAP8
BRRN1
CAP-G
CNAP1
INCENP
Aurora-A
CAP-G/G2
CAP-D2/D3
CAP-E
CAP-C
CAP-H/H2
TOP2
Aurora-B
Histone H3
Condensin
Histone H1
TOP1
DNA
Sister chromatid cohesion
Chromosome condensation
Chromosome separation in M phase

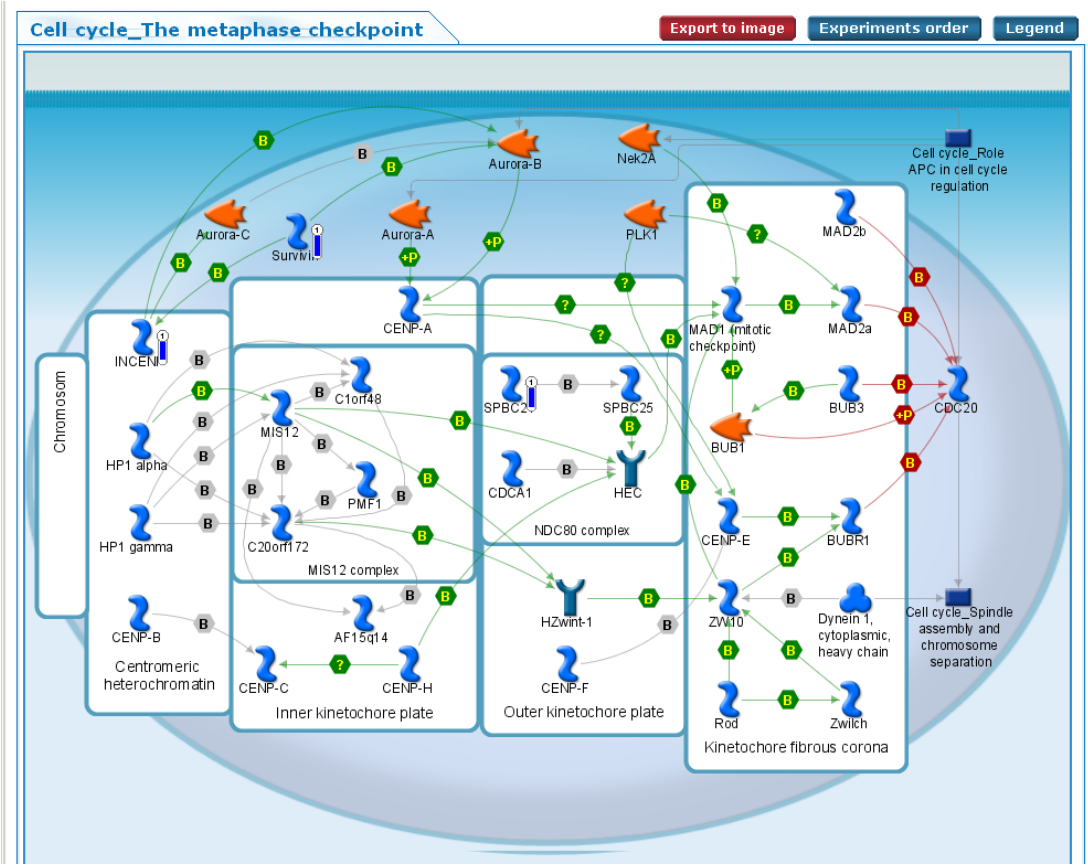
Cell cycle_The metaphase checkpoint
Export to image
Experiments order
Legend
Chromosom
Aurora-B
Nek2A
Aurora-C
Survivin
Aurora-A
PLK1
Cell cycle_Role APC in cell cycle regulation
MAD2b
CENP-A
MAD1 (mitotic checkpoint)
MAD2a
INCENP
C1orf48
SPBC25
BUB3
CDC20
MIS12
HP1 alpha
BUB1
PMF1
CDCA1
HEC
HP1 gamma
C20orf172
NDC80 complex
CENP-E
BUBR1
MIS12 complex
HZwint-1
ZW10
Dynein 1, cytoplasmic, heavy chain
Cell cycle_Spindle assembly and chromosome separation
CENP-B
AF15q14
CENP-F
Rod
Zwilch
Centromeric heterochromatin
CENP-C
CENP-H
Inner kinetochore plate
Outer kinetochore plate
Kinetochore fibrous corona

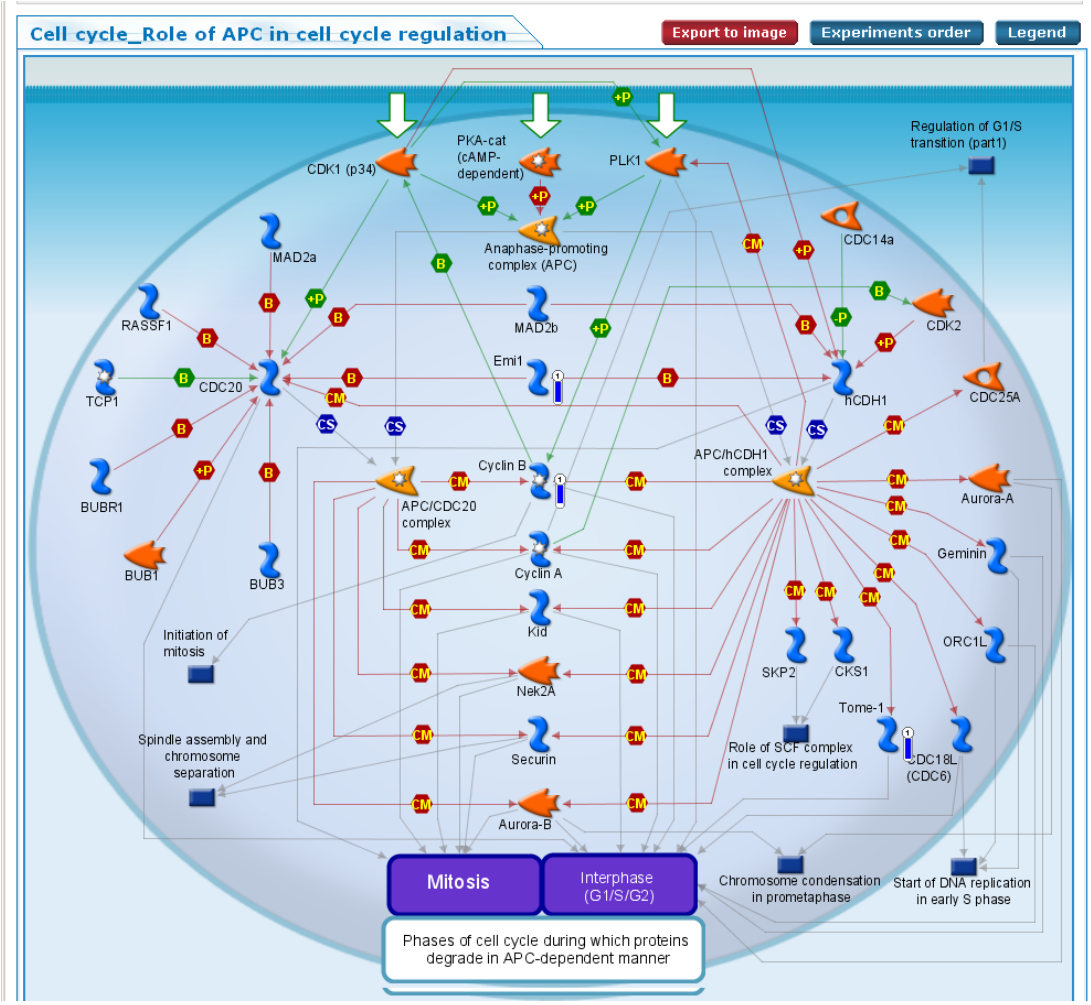
Cell cycle_Role of APC in cell cycle regulation
Export to image
Experiments order
Legend
CDK1 (p34)
PKA-cat (cAMP-dependent)
PLK1
Regulation of G1/S transition (part1)
Anaphase-promoting complex (APC)
MAD2a
MAD2b
CDC14a
CDK2
RASSF1
TCP1
CDC20
Emi1
hCDH1
CDC25A
BUBR1
BUB1
BUB3
APC/CDC20 complex
Cyclin B
APC/hCDH1 complex
Aurora-A
Cyclin A
Geminin
Kid
Initiation of mitosis
Nek2A
SKP2
CKS1
ORC1L
Tome-1
Spindle assembly and chromosome separation
Securin
Role of SCF complex in cell cycle regulation
CDC18L (CDC6)
Aurora-B
Mitosis
Interphase (G1/S/G2)
Chromosome condensation in prometaphase
Start of DNA replication in early S phase
Phases of cell cycle during which proteins degrade in APC-dependent manner

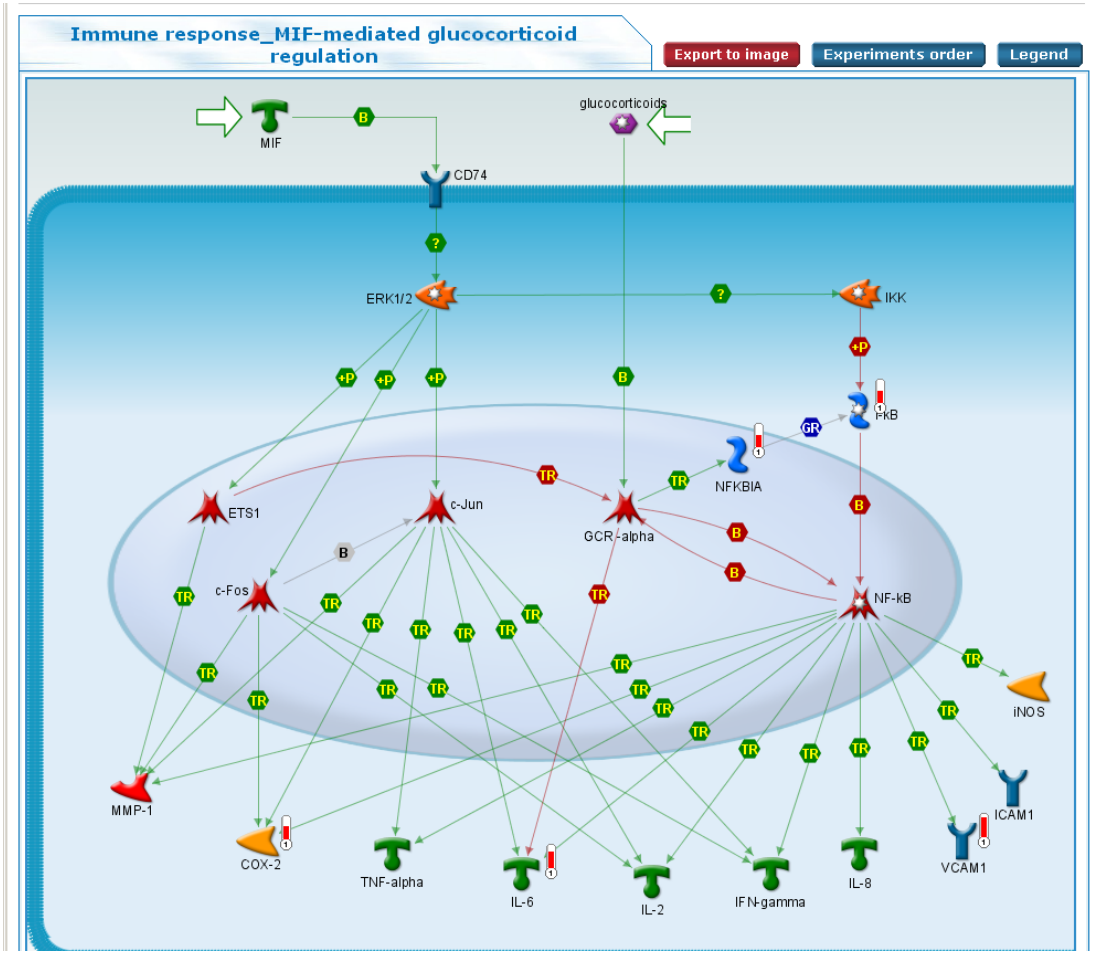
Immune response_MIF-mediated glucocorticoid regulation
Export to image
Experiments order
Legend
MIF
glucocorticoids
CD74
ERK1/2
IKK
IkB
NFKBIA
ETS1
c-Jun
GCR-alpha
c-Fos
NF-kB
iNOS
ICAM1
VCAM1
MMP-1
COX-2
TNF-alpha
IL-6
IL-2
IFN-gamma
IL-8

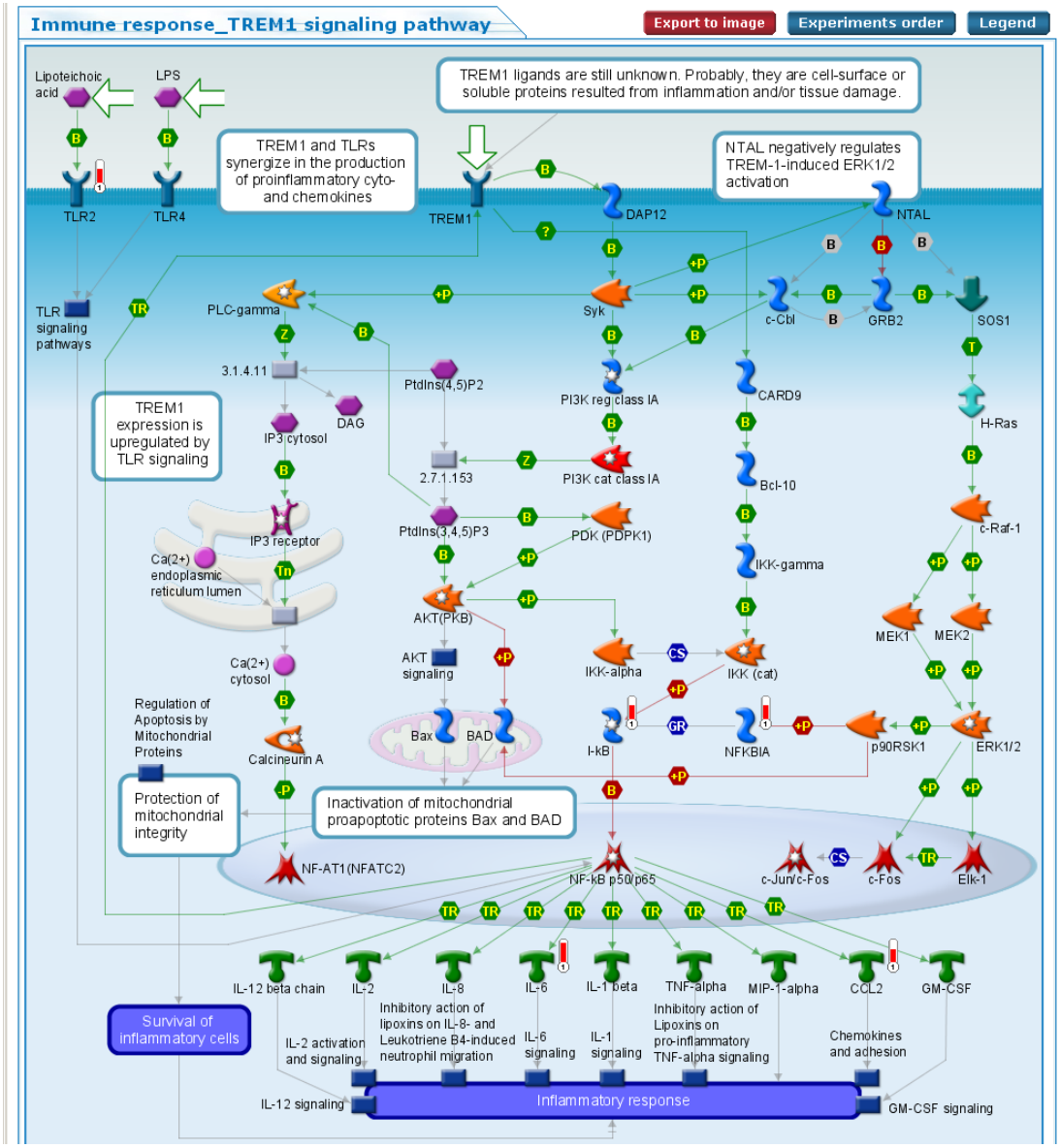
Immune response_TREM1 signaling pathway
Export to image
Experiments order
Legend
Lipoteichoic acid
LPS
TLR2
TLR4
TREM1 and TLRs synergize in the production of proinflammatory cyto- and chemokines
TREM1 ligands are still unknown. Probably, they are cell-surface or soluble proteins resulted from inflammation and/or tissue damage.
TREM1
DAP12
NTAL negatively regulates TREM-1-induced ERK1/2 activation
NTAL
TLR signaling pathways
PLC-gamma
Syk
c-Cbl
GRB2
SOS1
3.1.4.11
PtdIns(4,5)P2
PI3K reg class IA
CARD9
H-Ras
TREM1 expression is upregulated by TLR signaling
IP3 cytosol
DAG
2.7.1.153
PI3K cat class IA
Bcl-10
IP3 receptor
PtdIns(3,4,5)P3
PDK (PDPK1)
c-Raf-1
Ca(2+) endoplasmic reticulum lumen
IKK-gamma
AKT(PKB)
MEK1
MEK2
Ca(2+) cytosol
AKT signaling
IKK-alpha
IKK (cat)
Regulation of Apoptosis by Mitochondrial Proteins
Bax
BAD
I-kB
NFKBIA
p90RSK1
ERK1/2
Calcineurin A
Protection of mitochondrial integrity
Inactivation of mitochondrial proapoptotic proteins Bax and BAD
NF-AT1(NFATC2)
NF-kB p50/p65
c-Jun/c-Fos
c-Fos
Elk-1
IL-12 beta chain
IL-2
IL-8
IL-6
IL-1 beta
TNF-alpha
MIP-1-alpha
CCL2
GM-CSF
Survival of inflammatory cells
IL-2 activation and signaling
Inhibitory action of lipoxins on IL-8- and Leukotriene B4-induced neutrophil migration
IL-6 signaling
IL-1 signaling
Inhibitory action of Lipoxins on pro-inflammatory TNF-alpha signaling
Chemokines and adhesion
IL-12 signaling
Inflammatory response
GM-CSF signaling

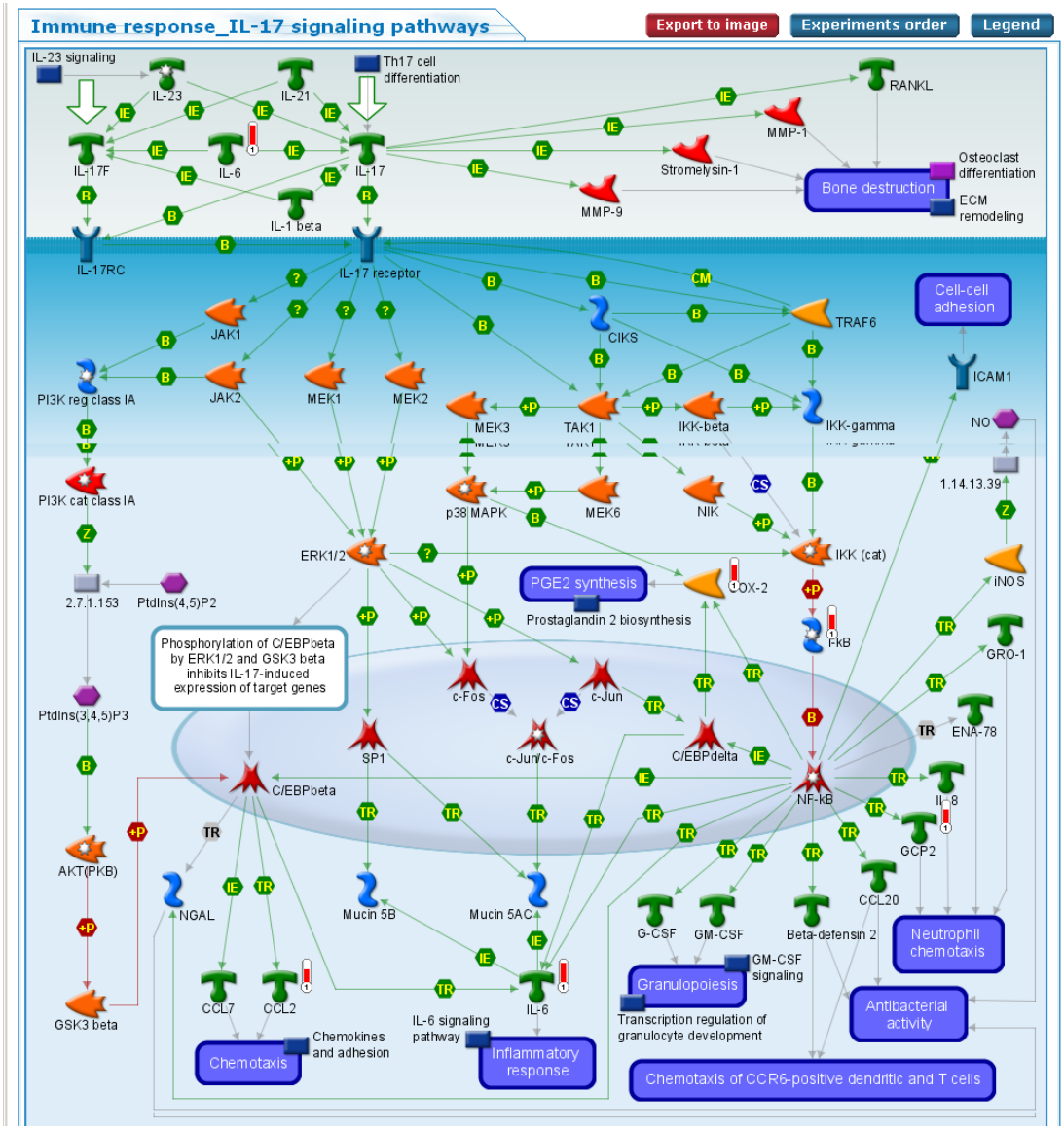
Immune response_IL-17 signaling pathways
Export to image
Experiments order
Legend
IL-23 signaling
IL-23
IL-21
Th17 cell differentiation
RANKL
MMP-1
IL-17F
IL-6
IL-17
Stromelysin-1
Osteoclast differentiation
Bone destruction
ECM remodeling
MMP-9
IL-1 beta
IL-17RC
IL-17 receptor
Cell-cell adhesion
JAK1
CIKS
TRAF6
ICAM1
PI3K reg class IA
JAK2
MEK1
MEK2
MEK3
TAK1
IKK-beta
IKK-gamma
NO
PI3K cat class IA
p38 MAPK
MEK6
NIK
1.14.13.39
ERK1/2
IKK (cat)
iNOS
2.7.1.153
PtdIns(4,5)P2
PGE2 synthesis
COX-2
Prostaglandin 2 biosynthesis
IkB
GRO-1
Phosphorylation of C/EBPbeta by ERK1/2 and GSK3 beta inhibits IL-17-induced expression of target genes
c-Fos
c-Jun
PtdIns(3,4,5)P3
SP1
c-Jun/c-Fos
C/EBPdelta
ENA-78
C/EBPbeta
NF-kB
IL-8
AKT(PKB)
GCP2
NGAL
Mucin 5B
Mucin 5AC
CCL20
G-CSF
GM-CSF
Beta-defensin 2
Neutrophil chemotaxis
GM-CSF signaling
Granulopoiesis
CCL7
CCL2
IL-6
Antibacterial activity
GSK3 beta
Chemokines and adhesion
Chemotaxis
IL-6 signaling pathway
Inflammatory response
Transcription regulation of granulocyte development
Chemotaxis of CCR6-positive dendritic and T cells

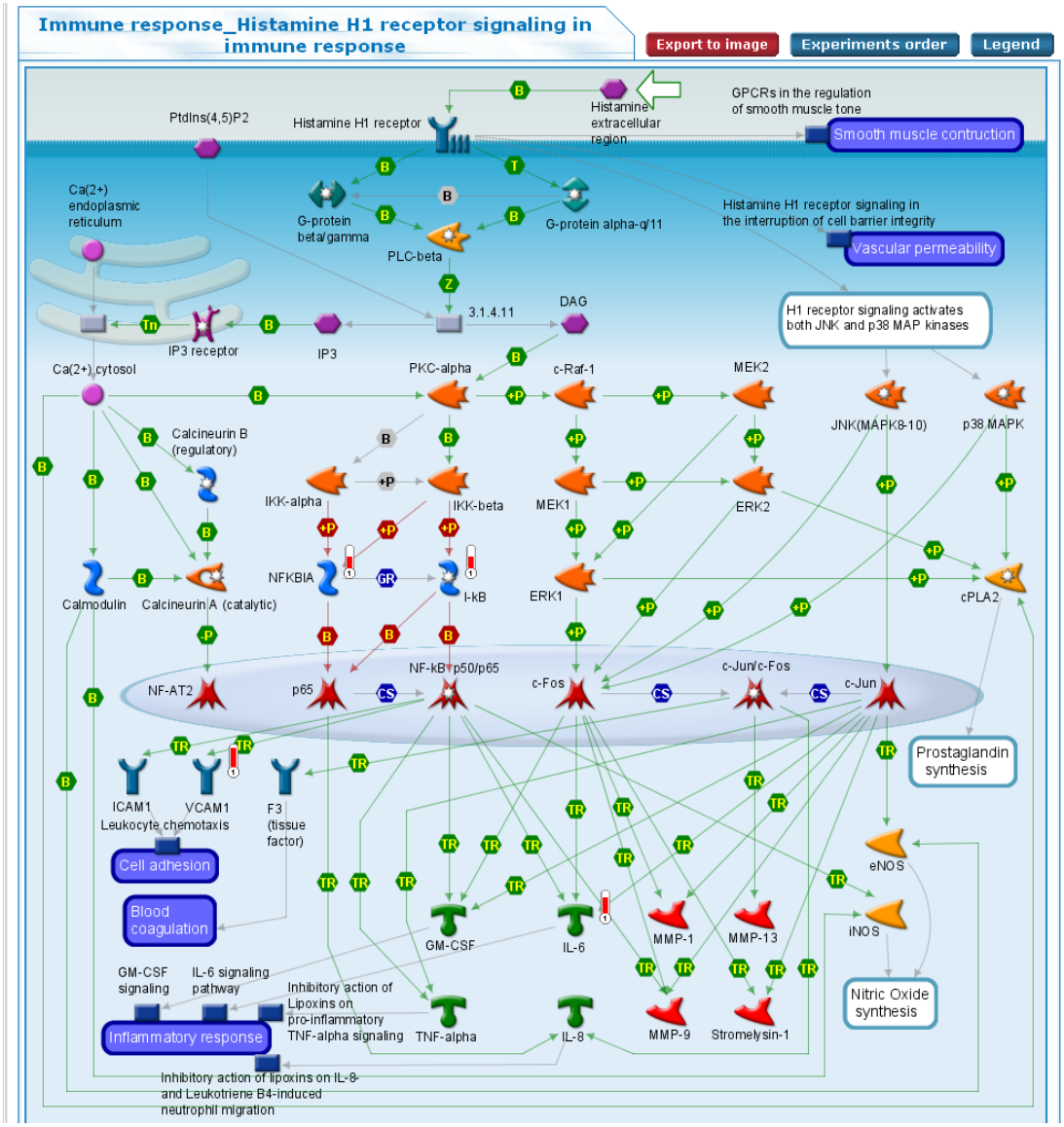
Immune response_Histamine H1 receptor signaling in immune response
Export to image
Experiments order
Legend
PtdIns(4,5)P2
Histamine H1 receptor
Histamine extracellular region
GPCRs in the regulation of smooth muscle tone
Smooth muscle contruction
Ca(2+) endoplasmic reticulum
G-protein beta/gamma
G-protein alpha-q/11
PLC-beta
Histamine H1 receptor signaling in the interruption of cell barrier integrity
Vascular permeability
IP3 receptor
IP3
3.1.4.11
DAG
H1 receptor signaling activates both JNK and p38 MAP kinases
Ca(2+) cytosol
PKC-alpha
c-Raf-1
MEK2
JNK(MAPK8-10)
p38 MAPK
Calcineurin B (regulatory)
IKK-alpha
IKK-beta
MEK1
ERK2
Calmodulin
Calcineurin A (catalytic)
NFKBIA
I-kB
ERK1
cPLA2
NF-AT2
p65
NF-kB p50/p65
c-Fos
c-Jun/c-Fos
c-Jun
Prostaglandin synthesis
ICAM1
VCAM1
F3 (tissue factor)
Leukocyte chemotaxis
Cell adhesion
Blood coagulation
eNOS
iNOS
GM-CSF
IL-6
MMP-1
MMP-13
GM-CSF signaling
IL-6 signaling pathway
Inhibitory action of Lipoxins on pro-inflammatory TNF-alpha signaling
TNF-alpha
IL-8
MMP-9
Stromelysin-1
Nitric Oxide synthesis
Inflammatory response
Inhibitory action of lipoxins on IL-8- and Leukotriene B4-induced neutrophil migration

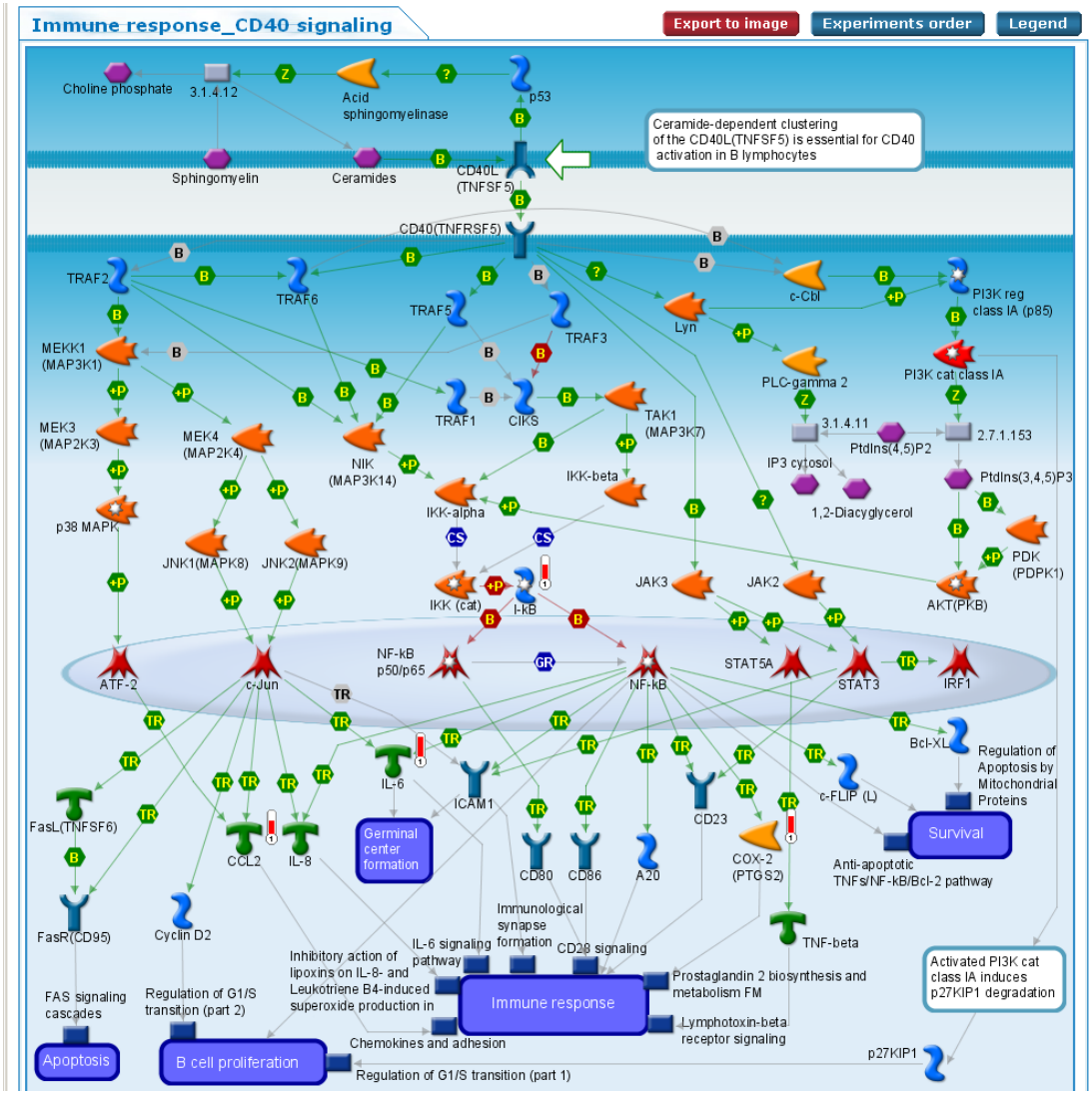
Immune response_CD40 signaling
Export to image
Experiments order
Legend
Choline phosphate
3.1.4.12
Acid sphingomyelinase
p53
Sphingomyelin
Ceramides
CD40L (TNFSF5)
Ceramide-dependent clustering of the CD40L(TNFSF5) is essential for CD40 activation in B lymphocytes
CD40(TNFRSF5)
TRAF2
TRAF6
TRAF5
TRAF3
TRAF1
CIKS
c-Cbl
Lyn
PI3K reg class IA (p85)
PI3K cat class IA
PLC-gamma 2
3.1.4.11
2.7.1.153
PtdIns(4,5)P2
IP3 cytosol
1,2-Diacylglycerol
PtdIns(3,4,5)P3
PDK (PDPK1)
AKT(PKB)
MEKK1 (MAP3K1)
MEK3 (MAP2K3)
MEK4 (MAP2K4)
NIK (MAP3K14)
TAK1 (MAP3K7)
IKK-beta
IKK-alpha
IKK (cat)
I-kB
p38 MAPK
JNK1(MAPK8)
JNK2(MAPK9)
JAK3
JAK2
NF-kB p50/p65
NF-kB
STAT5A
STAT3
IRF1
ATF-2
c-Jun
Bcl-XL
Regulation of Apoptosis by Mitochondrial Proteins
c-FLIP (L)
IL-6
ICAM1
CD23
FasL(TNFSF6)
CCL2
IL-8
Germinal center formation
CD80
CD86
A20
COX-2 (PTGS2)
Survival
Anti-apoptotic TNFs/NF-kB/Bcl-2 pathway
FasR(CD95)
Cyclin D2
Immunological synapse formation
IL-6 signaling pathway
CD28 signaling
TNF-beta
Activated PI3K cat class IA induces p27KIP1 degradation
Inhibitory action of lipoxins on IL-8- and Leukotriene B4-induced superoxide production in
Immune response
Prostaglandin 2 biosynthesis and metabolism FM
Lymphotoxin-beta receptor signaling
FAS signaling cascades
Regulation of G1/S transition (part 2)
Chemokines and adhesion
Apoptosis
B cell proliferation
Regulation of G1/S transition (part 1)
p27KIP1

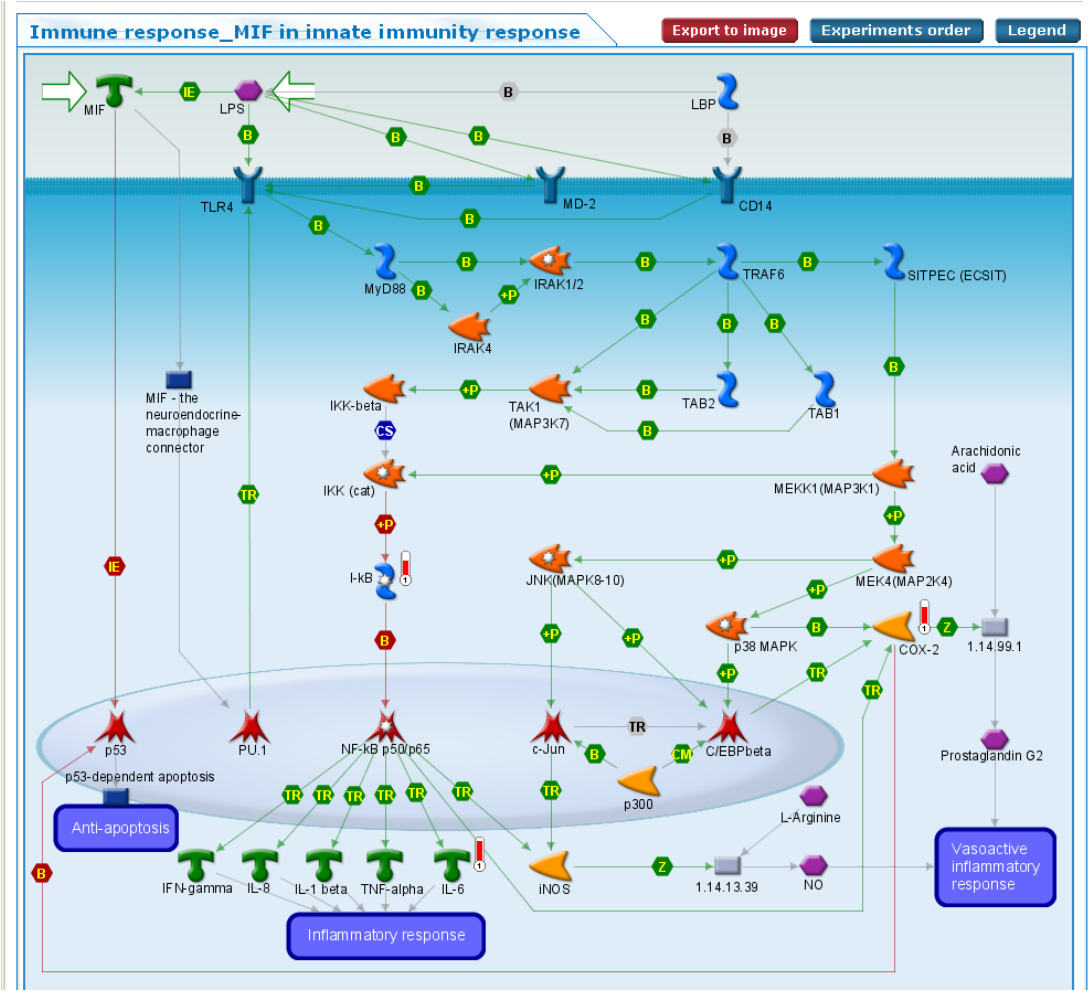
Immune response_MIF in innate immunity response
Export to image
Experiments order
Legend
MIF
LPS
LBP
TLR4
MD-2
CD14
MyD88
IRAK1/2
IRAK4
TRAF6
SITPEC (ECSIT)
MIF - the neuroendocrine-macrophage connector
IKK-beta
TAK1 (MAP3K7)
TAB2
TAB1
IKK (cat)
MEKK1(MAP3K1)
Arachidonic acid
I-kB
JNK(MAPK8-10)
MEK4(MAP2K4)
p38 MAPK
COX-2
1.14.99.1
p53
PU.1
NF-kB p50/p65
c-Jun
C/EBPbeta
p300
Prostaglandin G2
p53-dependent apoptosis
Anti-apoptosis
L-Arginine
IFN-gamma
IL-8
IL-1 beta
TNF-alpha
IL-6
iNOS
1.14.13.39
NO
Vasoactive inflammatory response
Inflammatory response

Appendix D

Cell cycle genes affected by GNT incorporation into MSCs.

Gene	Gene Function
BIRC5	Required for chromosome segregation and cytokinesis (also known as Survivin)[88]
CCDC99	Required for the localization of dynein and dynactin to the mitotic kinetochore[89]
CDC45	Required to the initiation of DNA replication[90]
CDCA3	Required for entry into mitosis and acts by participating at G2/M phase (also known as Tome-1)[91]
CHAF-1	Facilitates DNA methylation and histone H3 'Lys-9' methylation during replication-coupled chromatin assembly[92]
CKS2	Binds to the catalytic subunit of the cyclin dependent kinases and is essential for transitions between the G1/S phases and the G2/M phases[93]
Condensin	Required for conversion of interphase chromatin into mitotic-like condense chromosomes[94]
Cyclin B1 and B2	Components of cell cycle regulatory machinery, expressed during G2/M phase[95]
Cyclin G2	Negative regulator of cell cycle progesssion[96]
E2F1	Transcription activator of genes encoding proteins involved in DNA replication and cell-cycle progression from G1 to S phase[97]
FBox5	Regulates progression through early mitosis by inhibiting the anaphase promoting complex/cyclosome (APC)[98]
FEN1	5'-flap endonuclease and 5'-3' exonuclease involved in DNA replication[99]

GINS1	Required both for the initiation of chromosome replication and also for the normal progression of DNA replication forks (also known as PSF1)[100]
INCENP	Component of the chromosomal passenger complex (CPC), a complex that acts as a key regulator of mitosis and required for metato-anaphase transition[101]
KIF23	Moves antiparallel microtubules and localizes to the interzone of mitotic spindles[102]
MCM 2 and 4	Required for the initiation of eukaryotic genome replication[103]
MIS18	Required for normal chromosome segregation during mitosis[104]
PCNA	Involved in the control of eukaryotic DNA replication[105]
PLK4	Required for centriole duplication[106]
PRC1	Cross-links antiparallel microtubules; involved in cytokinesis[107]
RCS1	Mitotic regulator that controls the metaphase-to-anaphase transition[108]
SKA1 and 2	Required for timely anaphase onset during mitosis[109]
TCF19	Inhibits cell cycle by transcriptional repression of Cyclin E[110]

Appendix E

Figure D1. Flow cytometry diagrams of cell cycle analysis for Pig 1.

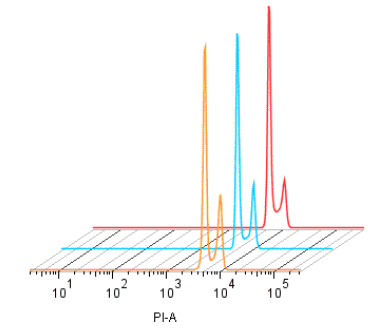

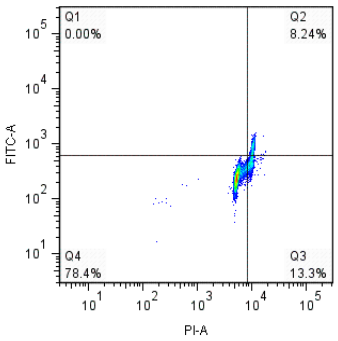

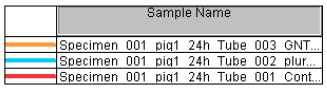

Specimen_001_pig1_24h_Tube_001_Control.fcs
Viable
8410

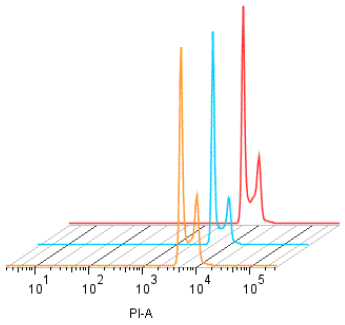

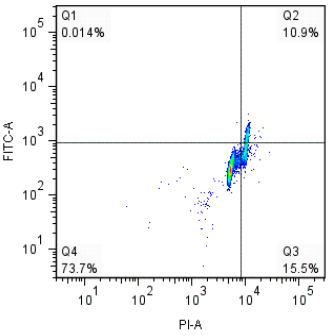

Specimen_001_pig1_24h_Tube_002_pluronic.fcs
Viable
7360

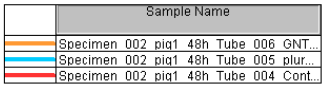

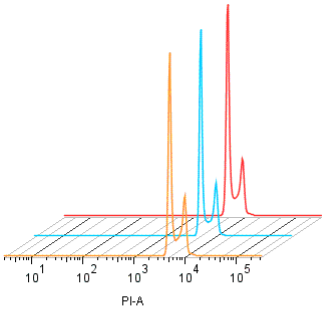

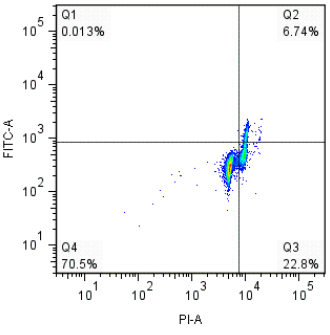

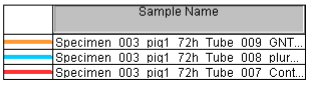

Specimen_001_pig1_24h_Tube_003_GNT.fcs
Viable
7998

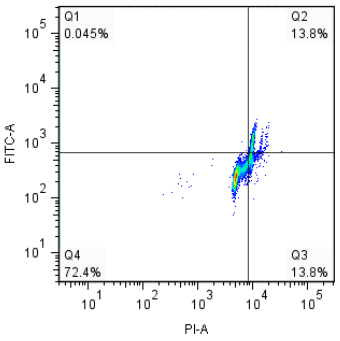

Specimen_002_pig1_48h_Tube_004_Control.fcs
Viable
8795

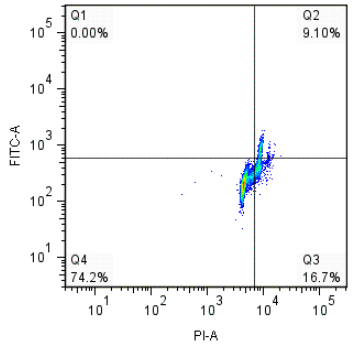

Specimen_003_pig1_72h_Tube_007_Control.fcs
Viable
8587

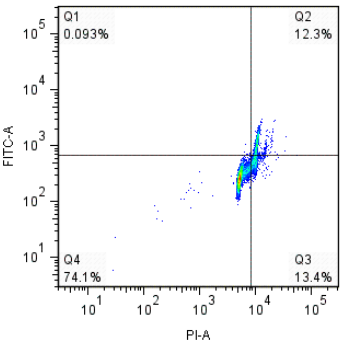

Specimen_002_pig1_48h_Tube_005_pluronic.fcs
Viable
8638

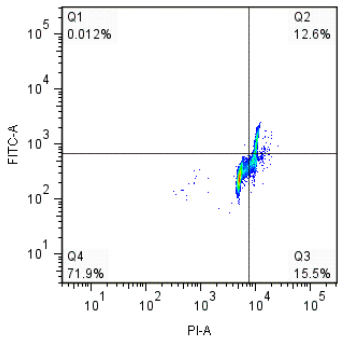

Specimen_003_pig1_72h_Tube_008_pluronic.fcs
Viable
8437

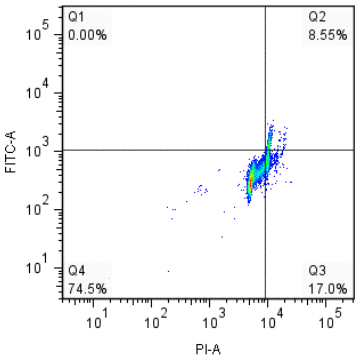

Specimen_002_pig1_48h_Tube_006_GNT.fcs
Viable
7659

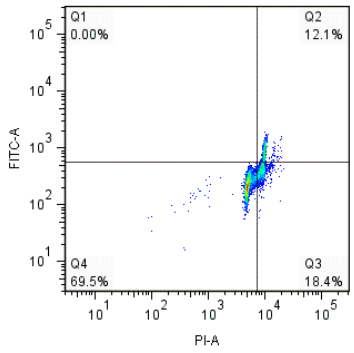

Specimen_003_pig1_72h_Tube_009_GNT.fcs
Viable
7651

Figure D2. Flow cytometry diagrams of cell cycle analysis for Pig 2.

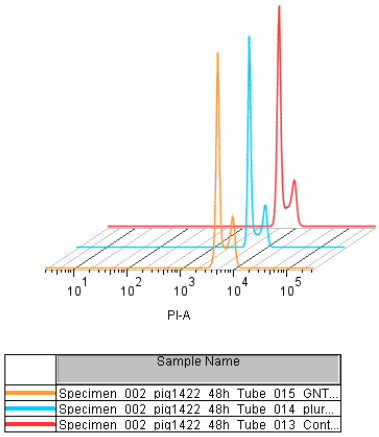

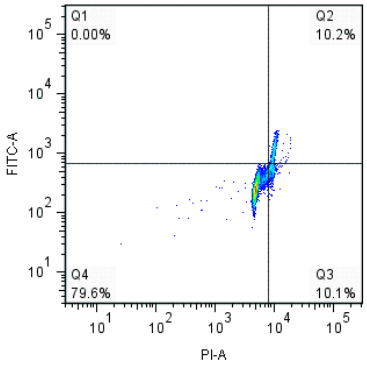

Specimen_001_pig1422_24h_Tube_010_Control.fcs
Viable
8874

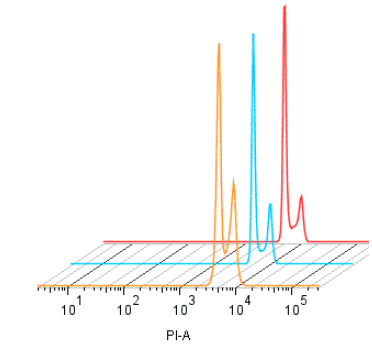

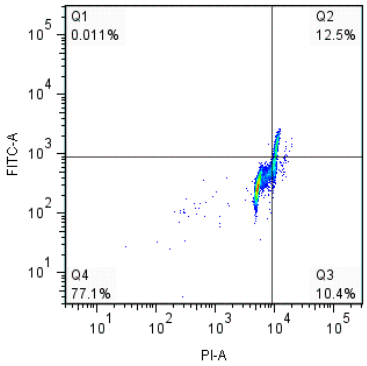

Specimen_001_pig1422_24h_Tube_011_pluronic.fcs
Viable
8796

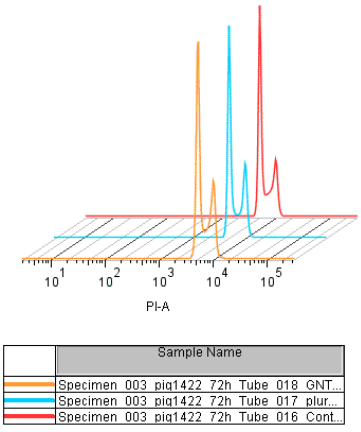

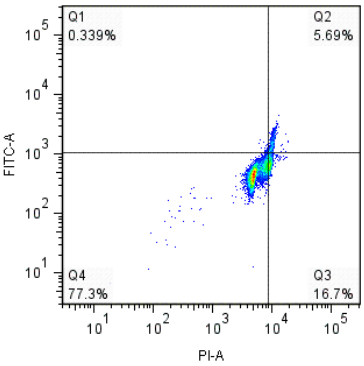

Specimen_001_pig1422_24h_Tube_012_GNT.fcs
Viable
7680

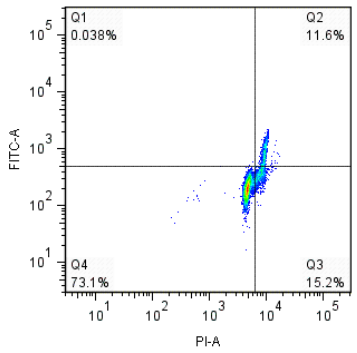

Specimen_002_pig1422_48h_Tube_013_Control.fcs
Viable
7958

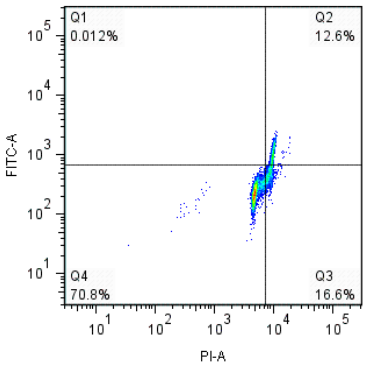

Specimen_003_pig1422_72h_Tube_016_Control.fcs
Viable
8206

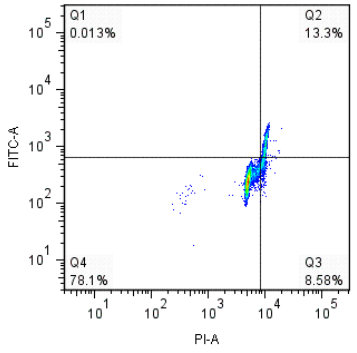

Specimen_002_pig1422_48h_Tube_014_pluronic.fcs
Viable
7865

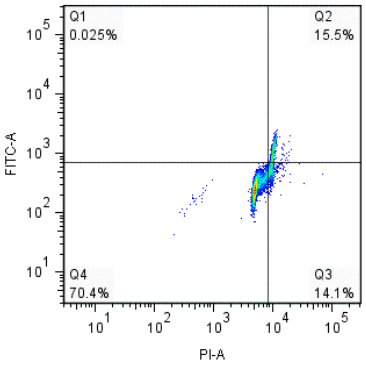

Specimen_003_pig1422_72h_Tube_017_pluronic.fcs
Viable
8097

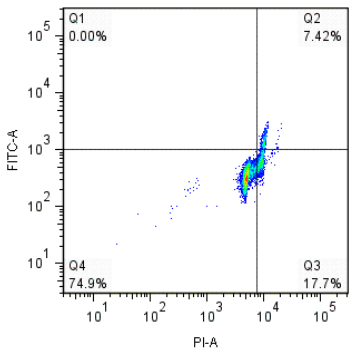

Specimen_002_pig1422_48h_Tube_015_GNT.fcs
Viable
7159

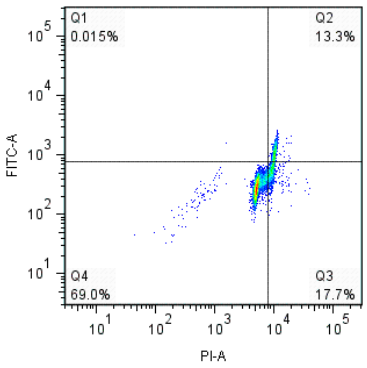

Specimen_003_pig1422_72h_Tube_018_GNT.fcs
Viable
6522

Figure D3. Flow cytometry diagrams of cell cycle analysis for Pig 3.

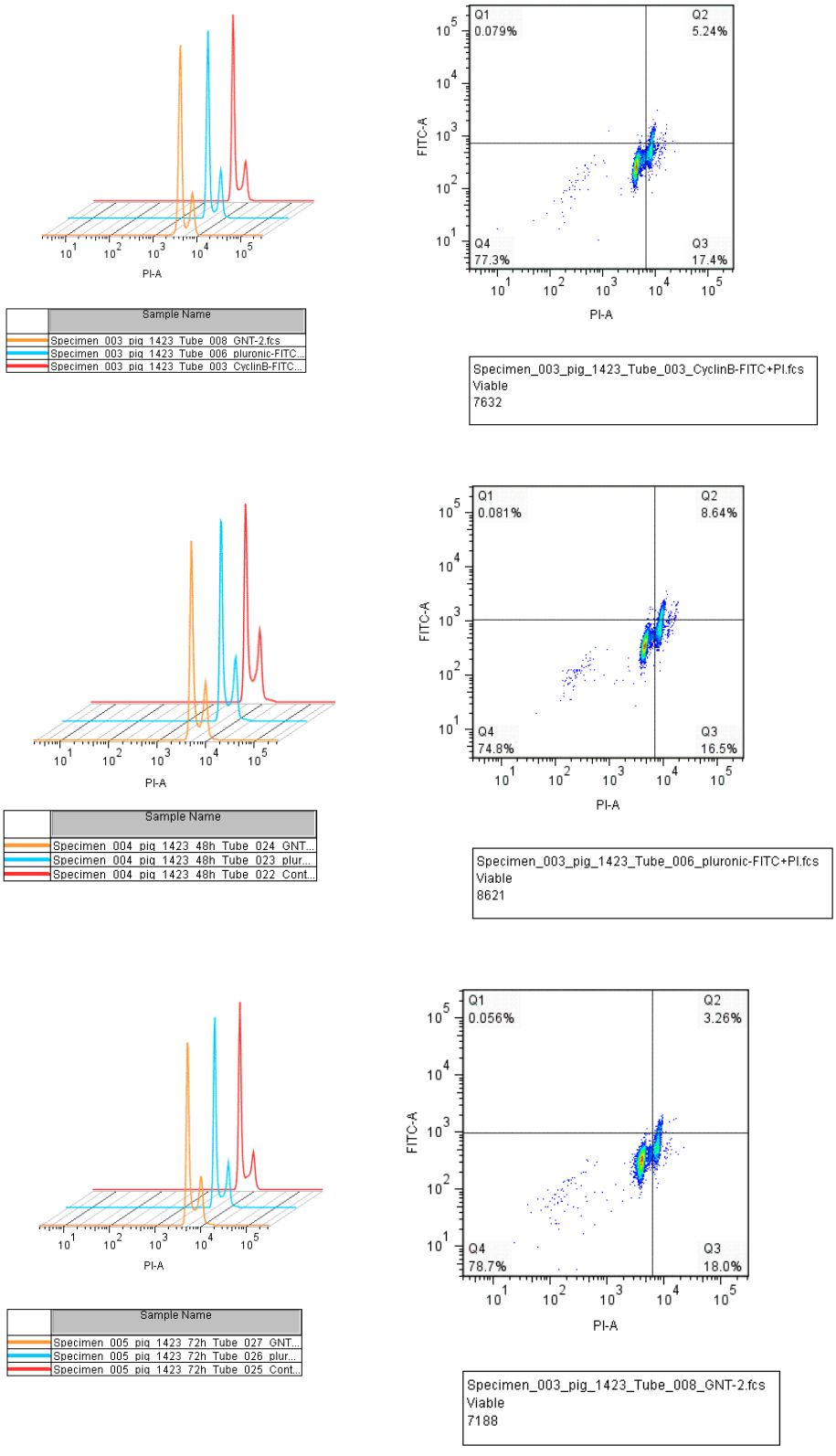

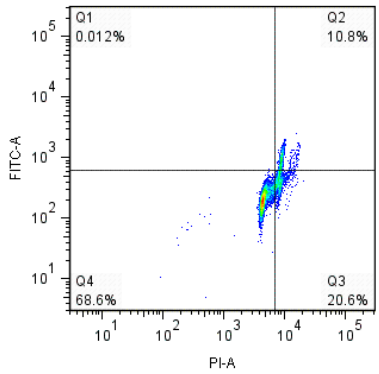

Specimen_004_pig_1423_48h_Tube_022_Control.fcs
Viable
8305

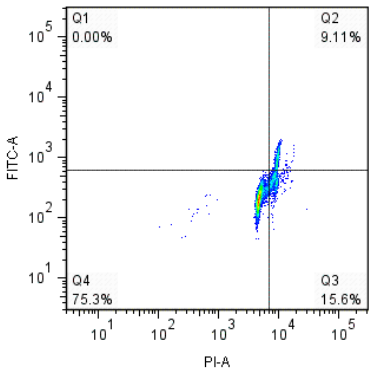

Specimen_005_pig_1423_72h_Tube_025_Control.fcs
Viable
8082

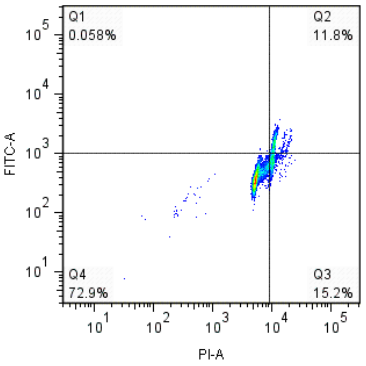

Specimen_004_pig_1423_48h_Tube_023_pluronic.fcs
Viable
8592

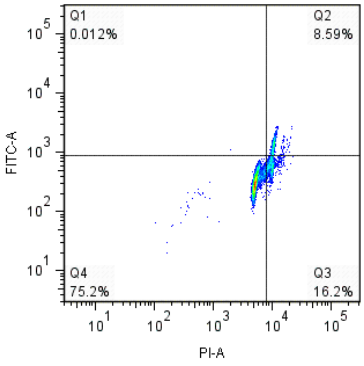

Specimen_005_pig_1423_72h_Tube_026_pluronic.fcs
Viable
8375

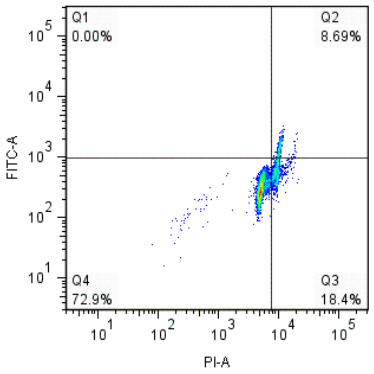

Specimen_004_pig_1423_48h_Tube_024_GNT.fcs
Viable
7110

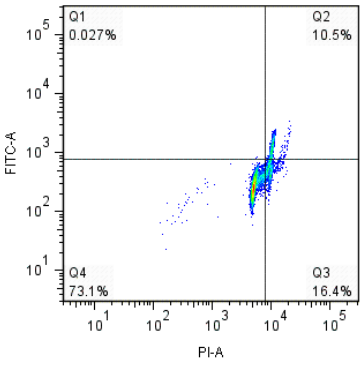

Specimen_005_pig_1423_72h_Tube_027_GNT.fcs
Viable
7336